Technical University of Munich
TUM School of Computation, Information and Technology

Wide-field mid-infrared optothermal microscopy and its application in live-cell imaging

Tao Yuan

Complete reprint of the dissertation approved by the TUM School of Computation, Information and Technology of the Technical University of Munich for the award of the Doktor der Ingenieurwissenschaften (Dr.-Ing.).

Chair: Prof. Dr. Oliver Hayden

Examiners:

1. Prof. Dr. Vasilis Ntziachristos
2. Prof. Dr. Ghulam Destgeer

The dissertation was submitted to the Technical University of Munich on 25 July 2023 and accepted by the TUM School of Computation, Information and Technology on 27 march 2024.

DEPARTMENT OF ELECTRICAL
AND COMPUTER ENGINEERING

Technische Universität München

Ph.D. Thesis

Wide-field mid-infrared optothermal microscopy and its application in live-cell imaging

Author: Tao Yuan

Supervisors:

Prof. Dr. Vasilis Ntziachristos

Prof. Dr. Ghulam Destgeer

Prof. Dr. Miguel A. Pleitez

Abstract:

Mid-infrared optothermal microscopy (MIR-OM) is a label-free technology that is capable of acquiring chemical contrast image based on the mid-infrared (MIR) photothermal/optothermal effect (termed optothermal effect in this thesis) of the sample. Imaging contrast of MIR-OM is specific to the chemical bond, which vibrates as specific wavelength mid-infrared light is absorbed by the sample. Since the amount of certain chemical bonds in living cells is related to the particular metabolism process, MIR-OM is a promising technology for living cells studies. For example, in the beta-oxidation, catabolic process of the fatty acid leads to the breakdown of methylene group (CH_2), and reduces its number in living cells, thus, CH_2 methylene group can be the target of this technology to study lipid metabolism. Compared with imaging technologies that use external fluorescent labels, such as fluorescence microscopies, MIR-OM does not rely on labels but the intrinsic chemical bonds. Therefore, it has the advantages of reducing the long labeling time and circumventing the metabolism interference introduced by labels. However, this imaging technique is still in its early development stage, facing limitations either from imaging speed, imaging field-of-view (FOV), or imaging reliability, reducing its attraction as a daily tool in biotechnology.

This dissertation aims to develop a new optothermal microscopy for high-speed, large FOV chemical contrast imaging, push this technology to image large population living cells, and statistically monitor their activities. For this sake, a wide-field excitation scheme is introduced to simultaneously excite the vibrational absorption over a large area by a broad MIR beam. To obtain the chemical contrast, phase contrast microscopy is used to detect the optical path difference (OPD) caused by optothermal effect of the sample. This detection scheme brings the advantage of fast speed compared with the focal excitation scheme, where the image is acquired by point-by-point scanning.

Here, firstly we present a pilot work to verify the feasibility of this detection scheme, in which a custom-made condenser-free phase contrast microscopy is applied for detecting the chemical contrast image, and the optothermal imaging of triglyceride (TAG) is demonstrated. Then the dissertation introduces a new phase imaging method for detecting OPD in a large FOV at high sensitivity – phase-shifting microscopy. It is demonstrated that with phase-shifting microscopy, the OPD noise is suppressed to sub nanometer, and a FOV of 50 times of state-of-art can be achieved. Validation of the microscope is performed by monitoring the activity of lipid droplets in living adipocytes.

Contents

Chapter 1 Introduction

1.1 Motivation

In the last half century, the life sciences have been greatly driven by fluorescence microscopy. However, most fluorescence microscopies rely on the use of external fluorescent labels, which can undergo photobleaching (*1*), photoconversion (*2*), and possibly alter the metabolic activity of cells (*3*). In response to the label-free demands from biologists, various contrast enhancement techniques have been proposed, such as interferometric scattering microscopies, quantitative phase contrast microscopies. However, the contrast provided by these methods lacks the chemical specificity. This thesis focuses on developing a wide-field optothermal microscopy for imaging living cells, driven by the need of a label-free and chemical-contrast imaging modality. Different from other label-free contrast enhancement methods, wide-field optothermal microscopy's contrast stems from cells' photothermal/optothermal effect after the vibrational absorption of mid-infrared light by the biomolecules.

1.2 Optothermal phenomenon

Photothermal/optothermal phenomenon occurs in the radiationless absorption of electromagnetic waves. The physical mechanism behind this phenomenon can be the molecule's electronic absorption of electromagnetic waves in the ultraviolet-visible (UV-VIS) range (200 – 800 nm in wavelength) , or the molecule's vibrational absorption of electromagnetic waves in the infrared (IR) range (800 – 12000 nm in wavelength, mainly the mid-infrared range: 2500 nm – 12000 nm) (*4*). During the absorption, the medium experiences a temperature increase since the absorbed energy is converted to thermal energy. An acoustic wave is usually generated after abrupt optothermal heating, creating the optoacoustic phenomenon (*5, 6*).

The electronic absorption occurs when the electron of molecule jumps to a higher orbital after absorption of a UV-VIS photon. Optothermal effect induced by electronic absorption has been detected for measuring the quantum yields and lifetime of an electron excited state (*7-9*), determinating the concentration of gas (*10*), and obtaining the spectrum of high absorption sample (*11-14*). In photochemistry, the studies of radiationless electronic transition have been facilitated by photothermal detection in case of low fluorescence quantum yield (*15, 16*). The optothermal effect generated by a transparent and homogenous medium leads to a thermal lens effect that has been used for studying the thermal optical properties of the sample (*17-19*).

Different from electronic absorption, vibrational absorption arises from the relative vibration of atoms inside the molecule when an infrared photon is absorbed by the molecule. These relative vibrations

usually cause the stretching of chemical bonds between the atoms. For example, the stretching of C-H bonds in fatty acids can be induced by the absorption of photons in wavenumber (reciprocal of wavelength) of 2920 cm^{-1} and 2850 cm^{-1}, and the vibration of carbonyl group C=O in ketones can be triggered by the absorption of photons in wavenumber around 1710 cm^{-1} (*20, 21*). Vibrational absorption plays the fundamental role in the Fourier-Transform Infrared Spectroscopy (FTIR) spectroscopy (*22-25*), and optothermal infrared spectroscopy (*26-28*), which have been used to evaluate the existence of specific molecular bond in the test sample, and even further confirm the molecular structure.

In the last few decades after 1980s, as the theories of optothermal phenonmenon have been developed (*29*), this phenonmenon has been used in microscopy technologies for achieving label-free imaging. Some of early optothermal microscopies have been applied for imaging of nanoparticles, single molecules, and living cells (*30-33*).

1.3 Vibrational microscopy

Motivated by the successful applications of vibrational spectroscopes such as FTIR spectroscopy and Raman scattering spectroscopy, various vibrational microscopies were proposed to acquire chemical information from a two dimensional area (chemical contrast image) instead of acquiring one dimensional spectrum. In vibrational microscopy, the pixel value of the image is molecule's vibrational signal at a given point of the FOV, where the vibrational signal can be original from MIR absorption or Raman scattering. Since the imaging contrast is generated by the inherent chemical bond, vibrational microscopy does not require the use of exogenous labels to enhance the imaging contrast. Compared with the imaging modalities that using exogenous labels, it reduces the time for the labeling process and circumvents the possible interference of metabolism by the labels.

Raman scattering-based vibrational microscopies is a genre of biomedical imaging technology that has been widely used in biological research. Different from mid-infrared vibrational absorption, Raman scattering triggers the vibration of molecule by exchanging a fraction of energy of a photon with the molecule bond's vibration energy. During the energy exchange, the scattered photon undergoes an energy loss ("Stokes" Raman scattering) or energy gain ("anti-Stokes" Raman scattering). This energy loss, or energy gain corresponding to the bond's vibration energy, can be observed as a red shift or blue shift of the scattering light by the detector. Collectively, these wavelength shifts of scattering light from a molecule construct a spectrum that characterizes the molecular structure. Since the Raman scattering efficiency is extremely low (scattering cross-section around 10^{-30} cm^2)(*34*), the spectral imaging acquisition is low, therefore, the enhanced techniques are applied to improve the scattering efficiency, such as Coherent Anti-Stokes Raman Scattering (CARS)(*35, 36*), Stimulated Raman Scattering (SRS)(*37*), Surface-Enhanced Raman Scattering (SERS)(*38, 39*). Nonetheless, a confocal configuration

has to be used to increase the number of incident photons, which increases the possibility of photodamage and requires the time-consuming point-by-point scanning to obtain an image (*40, 41*).

1.4 Mid-infrared optothermal microscopy

Vibrational microscopy can also be realized by detecting the optothermal signal generated from the absorption of mid-infrared light, i.e., detecting the temperature change. Compared with Raman scattering, mid-infrared absorption has a much stronger efficiency for exciting molecular vibration. MIR absorption cross-section is 10 orders of magnitude larger (absorption cross-section around 10^{-19} cm^2)(*42*) than Raman scattering.

In optothermal microscopy, direct detection of temperature change is usually unfeasible, due to the lack of a high sensitivity, high resolution temperature sensing technique. To achieve optothermal imaging, a pump-probe design is usually implemented, in which the mid-infrared light is used as the pump beam for optothermal excitation, and a visible (VIS) light is used as the probe beam for detecting the temperature change based on the thermal optical properties of the sample. This pump-probe imaging method was developed in the 1990s (*30, 31*), and has been used in electronic absorption-based optothermal microscopy, achieving the detection of single molecules, nanoparticles, and mitochondria (*31, 32, 43*).

A pump-probe design for the vibrational absorption-based optothermal microscopy was reported by Lee, by tuning the excitation wavelength to C-H stretching vibration through an optical parametric oscillator (OPO) (*44, 45*). Similar imaging methods were further developed afterward, achieving the imaging of tissue slice, single cell, and in vivo imaging (*33, 46, 47*). Nevertheless, the researchers utilized a confocal configuration for imaging acquisition, where the pump beam and probe beam were both focused by an objective to a diffraction limit spot, and a photodiode was used for detecting the transmission light. Although the confocal configuration provided high spectrum fatality, it acquired images using point-by-point scanning, leading to a trade-off between imaging speed and imaging FOV, i.e., the larger the FOV, the more time was needed for imaging acquisition. This trade-off problem has been a common problem for all microscopies that used the confocal configuration, including the Raman microscopies, optoacoustic microscopies, and fluorescence microscopies. The confocal configuration is challenging for applications that require high temporal resolution. For example, monitoring of the "saltatory" motion of lipid droplets, characterized by abrupt movements in the speed of 1-2 μm/s (*48, 49*).

Fortunately, the high absorption cross-section of optothermal effect allows optothermal microscopy to utilize a wide-field configuration that is impossible for Raman scattering-based microscopy. In the wide-field configuration, instead of focusing the excitation beam to a spot, a broad beam is used for optothermal excitation of a wide-field area. The optothermal map, i.e., the chemical contrast image, is

acquired by subtraction of two phase contrast images, captured by a camera. One phase image is obtained with MIR excitation (MIR-ON), and the other phase image is obtained without MIR excitation (MIR-OFF). Since the optical path length (phase) of the microscopic illumination light (probe beam) is refractive index dependent, and the refractive index of material/sample is temperature dependent (thermal-optical effect) (*50-52*), the phase image difference illustrates the optothermal map of the FOV, which is also a chemical contrast image. The wide-field configuration has the following advantages compared with confocal configuration:

Firstly, the imaging speed can be far beyond the speed of confocal configuration. This is because that the imaging acquisition time is determined by camera exposure time instead of raster scanning. The exposure time of a commercially available camera can easily reduce to 1 μs. With the implementation of a pulse laser, the exposure time can even reduce to a few nanoseconds or less. Even though a single chemical contrast image requires two phase contrast images (MIR-ON and MIR-OFF images), the time duration between these two images can reduce to the thermal relaxation time of a single MIR pulse. This relaxation time was found in the range of a few μs to around one hundred μs (*52*). In a word, the potential imaging speed of this imaging modality can reach up to 10 kHz, which is not possible by the point-by-point scanning method.

Secondly, MIR excitation power flux density (PFD) can be reduced by using the wide-field configuration. As the pump beam is broadened from a focus spot (1 μm^2) to the whole image FOV (5×10^5 μm^2), the illumination area is 5 orders of magnitude larger than the confocal configuration. As a result, the power flux density of the excitation beam can reduce by 5 orders of magnitude, which brings the advantage of less phototoxic to the living cells.

1.5 Problems addressed in this thesis

Using the wide-field configuration, many wide-field optothermal microscopes have been proposed recently. However, the demonstrated effective FOVs were limited in the range of 3.1×10^2 to 2.0×10^3 μm^2 (20 to 50 μm in diameter), illustrating only a single cell or few beads (*50-52*). The reduced FOVs are unsuitable for imaging large cells population and for statistical study of large numbers of cells. Furthermore, the demonstrated FOVs were characterized by a Gaussian shape artifact, where the middle of the FOV showed high chemical-contrast and the surrounding of the FOV showed low chemical-contrast. The limitation of FOV stemmed from the fact that the weak optothermal signal could not be detected when the MIR beam was further expanded.

Secondly, wide-field optothermal microscopes work based on quantitatively probing the phase contrast change of the sample induced by mid-infrared absorption (termed MIR-phase, denoted by $\Delta\varphi$). However, the sample itself also retard the phase (termed intrinsic-phase, denoted by ϕ_0) dramatically due to its refractive index, dry mass, etc., even if there is no MIR irradiated. It is known that the MIR-phase is

small ($\Delta\varphi$ less than 0.01 rad (*52, 53*)), while intrinsic-phase ϕ_0 of a cell can be 3 orders of magnitude larger (*54, 55*). Detecting subtle phase change from this large intrinsic phase image is a challenge. Moreover, in a phase-detection system, the phase value usually wraps back to $-\pi$ rad when it passes over π, creating a spatially sharp change that needs to be reconstructed.

In this work, we hypothesize that intrinsic-phase dependency problem (and, thus, phase wrapping) can be solved by means of a phase-shifting mechanism. For this sake, here we introduce Phase-shifting Optothermal microscopy (PSOM). PSOM acquires intensity images (MIR-ON or MIR-OFF) instead of phase images, where the intensity is sinusoidally related to the phase. The cancelation of intrinsic-phase is carried out by square summation of four MIR-ON and MIR-OFF intensity image subtractions. We also hypothesize that the intrinsic-phase cancelation carried out by the phase-shifting mechanism can suppress the phase noise, and increase the sensitivity of the phase detection. With this benefit, further expansion of the FOV can be feasible.

1.6 Thesis organization

This dissertation focuses on the development of a new wide-field optothermal microscopy technique that possesses an imaging field-of-view (FOV) of up to 5×10^5 μm^2, enabling the chemical contrast imaging of multiple cells simultaneously. The imaging concept of this wide-field optothermal microscopy will be discussed in Chapter 3. Chapter 4, Chapter 5, and Chapter 6 consist of the major works during my PhD. In chapter 4, I develop two phase imaging methods (i.e., the probe systems) that will be utilized for mid-infrared (MIR) phase detection. Equipped with the probe systems, I delve into the details of developing an optothermal microscopy system in Chapter 5 and Chapter 6. As examples of its operation, I demonstrate measurements of large lipid droplets (LDs) in mature adipocytes, hyperspectral imaging, and dynamic measurements of LDs in adipocytes within a large FOV.

The dissertation is organized as follows:

Chapter 1 provides a brief introduction to motivation, optothermal phenomenon, the background for developing optothermal microscope, and discusses the limitations of state-of-art wide-field optothermal microscopes and the contribution of this work.

Chapter 2 reviews the physical knowledge of vibrational absorption, and introduces the basic principle of optothermal effect.

Chapter 3 introduces the imaging principle of wide-field optothermal microscopy.

Chapter 4 introduces two phase-detection methods that developed in this thesis: a condenser-free phase contrast microscopy and a phase-shifting microscopy. For the section on condenser-free phase contrast microscopy, we developed an analytic relation between the phase and the intensity image acquired by Zernike phase contrast microscope. In the section on phase-shifting microscopy, we discuss the polarization phase-shifting mechanism. This chapter provides the necessary knowledge for understanding the probe module of wide-field optothermal microscopy.

Chapter 5 introduces a pilot work of wide-field optothermal microscopy, where the MIR-phase is probed by a condenser free phase contrast microscopy. With this pilot work, we are able to measure the chemical contrast of a synthetic sample and the single pulse thermal relaxation time in the water.

Chapter 6 introduces the development of a wide-field optothermal microscopy by using a phase-shifting microscope as a probe method, illustrates how the phase-shifting mechanism facilitates the MIR-phase measurement, and circumvents the need for intrinsic-phase reconstruction. The resolution, and imaging FOV of the microscopy are characterized in this chapter. And examples of operation are demonstrated, i.e., optothermal microscopy imaging of living cells.

Chapter 7 gives a brief summary of the presented work, and an outlook for the application and further improvement.

Chapter 2 Fundamentals of wide-field optothermal imaging

2.1 Interactions of light and matter

The interaction between matter and light varies across different regions of the electromagnetic spectrum. The short wavelength electromagnetic wave acts like particles, for example, when an x-ray (wavelength: 0.03 - 3 nanometers) photon interacts with an electron, both momentum of the electron and photon change, and the energy lost during the interaction results in scattered photons with longer wavelength, see **Fig. 2-1**. This phenomenon – termed Compton scattering - convinced physicists that light can be treated as a stream of particles.

In the UV-VIS range (UV:100 to 400 nm, and VIS: 400 to 800 nm) of electromagnetic waves, the interaction of a photon with an atom or molecule usually results in the emission or transition of electrons. Emission of electrons occurs when a metal plate is irradiated by UV light when the light exceeds a certain frequency – regardless of the intensity and irradiation time. This phenomenon - the photoelectric effect - disagrees with classical electromagnetism. The explanation of this photoelectric effect resulted in the early concept of quantum mechanics since it could only be explained by considering the light as packets of energy – photons/quanta. The amount of photon's energy E is proportional to the frequency of the light ν_p by Planck's constant h: $E = h\nu_p$.

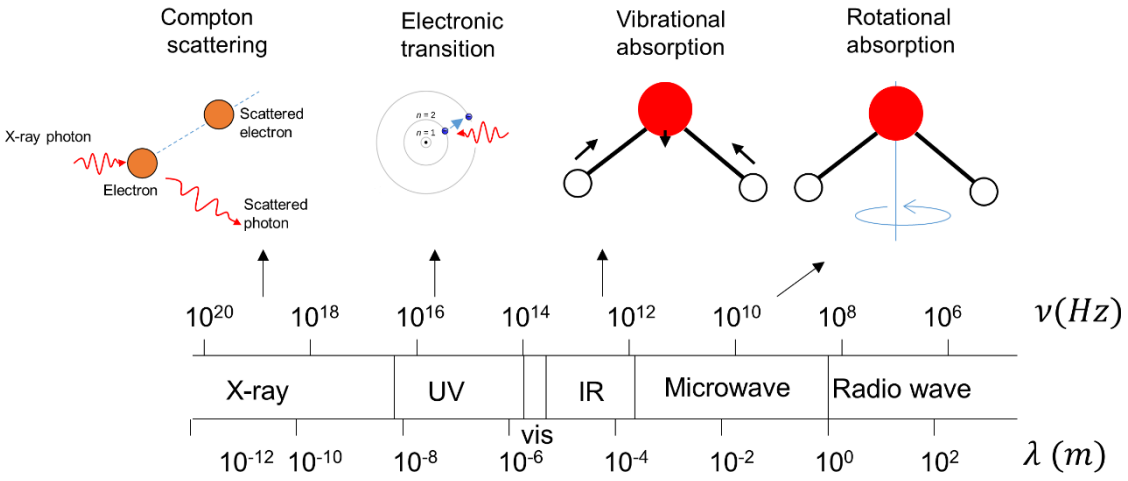

Fig. 2-1. Interactions of light with matter at different ranges of electromagnetic wave. Top: Illustration of the interactions between light and matter (electron, atom, molecule). Bottom: Electromagnetic wave ranging from x-ray to radio wave, with frequency and wavelength indicated. UV: Ultraviolet; IR: Infrared; vis: Visible.As the energy of the photon is not enough to kick out the electron (for instance, the interaction of a visible photon with an organic molecule),

the photon is absorbed and the electron in the molecule transits to a higher allowed orbital. This electronic transition usually takes place when the energy of the photon matches the quantized energy level of the atom or molecule. This kind of interaction plays an important role in UV-VIS spectroscopy.

The interaction of mid-infrared photons with molecules is similar to the electronic transition. It is found that not only the energy of electrons in a molecule can be quantized to discrete energy levels, but the vibration of atoms within the molecule can also be quantized to discrete energy levels. The amount of energy difference between these energy levels (especially the energy level between the ground state and the first excited state) matches the photon energy in the infrared region (mainly the mid-infrared region). Therefore, the absorption of mid-infrared photons by a molecule generally leads to the vibration of atoms in the molecule. Different chemical bonds usually have different vibration frequencies, corresponding to absorption peaks in the absorption spectrum. The mid-infrared spectrum can be used as a fingerprint for inferring the existence of certain chemical bonds.

2.2 Molecular vibrational absorption

A molecule consists of two or more atoms connected by chemical bonds. Like the spring in a harmonic oscillator, the length of the chemical bond is not fixed. Therefore, the atoms can vibrate in a small space like a microscopic harmonic oscillator. This section demonstrates the quantization of this microscopic harmonic oscillator.

2.2.1 Vibrational absorption of diatomic molecule

The simplest example of molecular vibration is the vibration of a diatomic molecule. Although the diatomic molecule is an anharmonic oscillator, it can be approximated as a harmonic oscillator if the displacement of atoms is small (see **Fig. 2-2**). The potential energy V of a harmonic oscillator is known to follow a parabolic equation (*56*):

$$V = \frac{1}{2}k\Delta x^2 \qquad \textit{eq. 2-1}$$

Where k is Hooke's constant of the spring, and Δx is the spring extension, which takes 0 when the spring has the length at rest.

For a harmonic oscillator in classical mechanics, the spring length $x(t)$ as a function of time t can be precisely obtained; and the total energy E of the harmonic oscillator can be any continuous value:

$$x(t) = Acos(\omega t + \varphi) + x_0 \qquad \textit{eq. 2-2}$$

$$E = \frac{1}{2}kA^2 \qquad \textit{eq. 2-3}$$

Where x_0 is the spring length at rest, A is the maximum spring extension (i.e., Amplitude), and φ is the initial phase of the oscillator, ω is angular frequency given as $\omega = \sqrt{k/\eta}$, where k is the Hooke's constant of the spring, and η is the reduced mass, can be obtained from two mass points m_1 and m_2, connected at two ends of spring: $\eta = \frac{m_1 m_2}{m_1 + m_2}$.

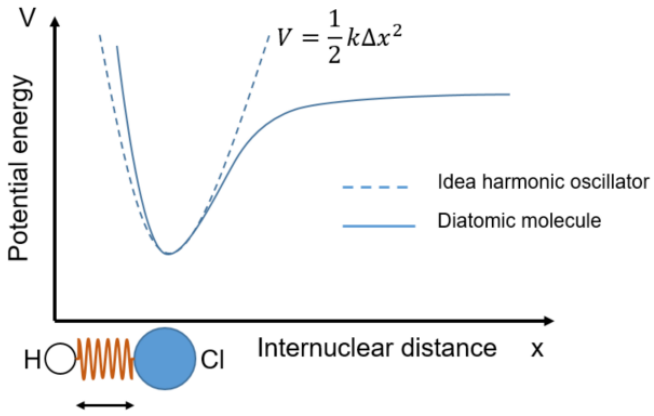

Fig. 2-2. **Diatomic molecule potential energy curve.** Potential energy curve (solid curve) for a diatomic molecule and compared with energy curve of an idea harmonic oscillator (dashed curve).

However, the microscopic word is governed by quantum mechanics, there we cannot precisely determine the bond length, and the energy stored in the oscillator is not continuous. Solving the harmonic oscillator problem by applying the Schrödinger equation yields discrete eigenstates with associated eigenvalues (*56*):

$$\Psi_n(x) = \left(\frac{\eta\omega}{\pi\hbar}\right)^{1/4} \frac{1}{\sqrt{2^n n!}} H_n(\xi) e^{-\xi^2/2} \qquad \textit{eq. 2-4}$$

$$E_n = \hbar\omega(n + 1/2) \qquad \textit{eq. 2-5}$$

Where ω, and η are given previously as angular frequency and reduced mass. $\hbar$ is reduced Planck's constant $\hbar = h/2\pi$. n is an integer ranging from 0, 1, 2,… and $\xi \equiv \sqrt{\frac{\eta\omega}{\hbar}}x$. H_n is Hermite polynomials of order n, see ref. (*56*). The square of the eigenstate gives the possibility as a function of bond length, and the corresponding eigenvalue gives the allowed energy level of the oscillator for the eigenstate.

The absorption of infrared light by the diatomic molecule can cause transitions between energy levels (mainly the transition from ground state *n=0*, to first excitation state *n=1*, due to the large population of ground state molecules). The absorption occurs as the energy of the photon $h\nu_p$ matches the adjacent energy levels $\hbar\omega$ in eq. 2-5:

$$h\nu_p = \Delta E = \hbar\omega \qquad \textit{eq. 2-6}$$

Therefore, it is the angular frequency ω of the vibration determines the type of photon that can be absorbed by the molecule. This frequency is inherent to the chemical bond and is related to the mass of the atoms constituting the bond, as well as the force exerted between the atoms. It is known that the angular frequency of most of the molecular vibration matches the mid-infrared range of the electromagnetic wave. Taking hydrogen chloride (HCl) as an example, it has a vibrational absorption band around 2860 cm^{-1} (3.5 µm) as shown in **Fig. 2-3**.

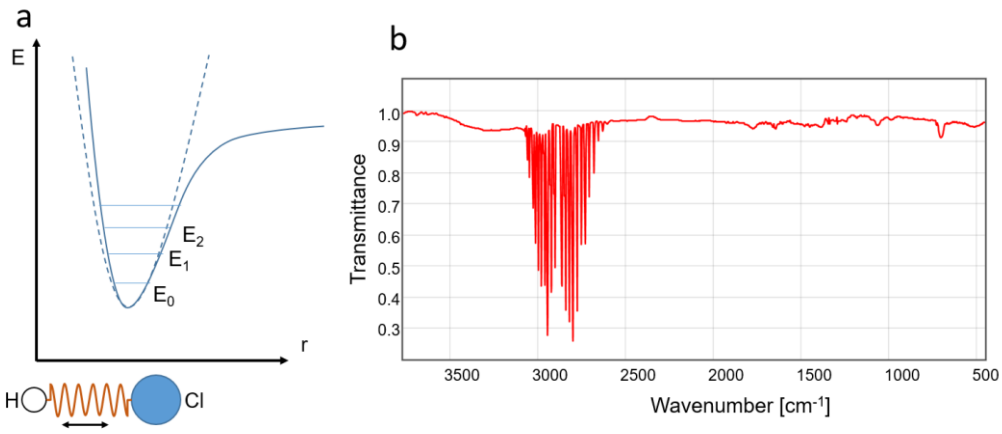

Fig. 2-3. Harmonic oscillator model of HCl molecule. a, Harmonic oscillator model of HCl molecule, and its quantized energy levels. **b,** MIR spectrum of HCl in the gas phase. Absorption occurs as vibrational state transit from E0 (ground state) to E1 (first excitation state) showing an absorption band around 2860 cm^{-1}, the breakdown of the vibration band into sharp peaks is caused by the difference of rotational states within each vibrational state. [Spectrum data from NIST Standard Reference Database 69: NIST Chemistry WebBook]

2.2.2 Vibrational absorption of polyatomic molecule

Vibration motion in polyatomic molecules is much more complicated due to the large number of spatial degrees of freedom and the force exerted between the atoms. The spatial degree of freedom is the independent motion of atoms in space. Since the displacement of an atom from its equilibrium position can be described by a 3-dimensional vector (x_1, x_2, x_3) - corresponding to 3 degrees of freedom, displacements of *N* atoms from their equilibrium positions can be described by 3*N*-dimensional vector (x_1, x_2, x_3, x_4, ..., x_{3N}), corresponding to 3*N* degrees of freedom. In a molecule, these 3*N* degrees of

freedom are constrained by the internal force (chemical bonds), and the atoms may locate in a symmetric location. The theory for vibrational spectra of polyatomic molecules is cumbersome and usually involves analysis by group theory. Here we introduce a simplified mathematical treatment of the vibrational theory, for understanding the quantization of polyatomic molecule vibration.

To solve the vibrational problem, one might first want to find the expression of the potential energy using the 3*N* mass weight coordination $V(q_1, q_2, q_3, q_4, \dots, q_{3N})$ (*57*). Assume the motion of atoms is close to their equilibrium positions, Taylor's expansion of *V* near the equilibrium point can be written as follow:

$$V = V_0 + \sum_{i=1}^{3N} \left(\frac{\partial V}{\partial q_i}\right)_0 q_i + \frac{1}{2} \sum_{i,j=1}^{3N} \left(\frac{\partial^2 V}{\partial q_i \, \partial q_j}\right)_0 q_i q_j + HO \qquad \textit{eq. 2-7}$$

Where $\left(\frac{\partial V}{\partial q_i}\right)_0$ denotes the derivative at the equilibrium point, and q_i is the mass weight coordination $q_i = \sqrt{m_i} x_i$, where m_i is the mass of the atom with index *i*; x_i is atom's displacement from the equilibrium position. HO denotes the higher-order terms of expansion. Moreover, knowing the potential energy is at its minimum when the atom is just in its equilibrium position, one can get $\left(\frac{\partial V}{\partial q_i}\right)_0 = 0$ for all q_i. One can drop away the higher order terms HO to simplify the analysis. Besides, by choosing the potential energy of the equilibrium point as 0, one can also drop away the V_0 term and have:

$$V = \frac{1}{2} \sum_{i,j=1}^{3N} f_{ij} q_i q_j \qquad \textit{eq. 2-8}$$

Where $f_{ij} = \left(\frac{\partial^2 V}{\partial q_i \, \partial q_j}\right)_0$ constructs the Hessian matrix $\boldsymbol{F}$, served as a vibration constant matrix analogous to Hooke's constant:

$$\boldsymbol{F} = \begin{pmatrix} f_{1,1} & f_{1,2} & \cdots & f_{1,3N} \\ f_{2,1} & f_{2,2} & \cdots & f_{2,3N} \\ \vdots & \vdots & \cdots & \vdots \\ f_{3N,1} & f_{3N,2} & \cdots & f_{3N,3N} \end{pmatrix} \qquad \textit{eq. 2-9}$$

Directly applying the Schrödinger equation for the potential function given in eq. 2-8 is impractical due to the crossing products of the coordination.

It can be shown that these 3*N* degrees of freedom $(q_1, q_2, q_3, q_4, \dots, q_{3N})$ can be linearly transferred to normal coordination $(Q_1, Q_2, Q_3, Q_4, \dots, Q_{3N})$, by a matrix composed by the eigenvector of Hessian matrix $\boldsymbol{F}$, so that the potential energy can be written as (*57*):

$$V = \frac{1}{2}\sum_{k=1}^{3N} \lambda_k{}^2 \mathrm{Q}_k^2 \qquad \textit{eq. 2-10}$$

Here each coordination in $(Q_1, Q_2, Q_3, Q_4, \dots, Q_{3N})$ corresponds to a normal mode of vibration, in which each normal mode vibration is linearly independent (due to the independence of eigenvector), and λ_k is vibration frequency of the corresponding normal mode, which is also the eigenvalue of matrix $\boldsymbol{F}$. It can be further shown that (for a nonlinear molecule) there are 6 normal modes possessing a vibrational frequency of 0, related to the translation of all atoms as a whole in space following x, y, and z directions, and rotation of the whole molecule regarding to x, y, and z axis. The deduction of 6 normal modes results in $3N - 6$ normal modes (which is $3N - 5$ for a linear molecule).

$$V = \frac{1}{2}\sum_{k=1}^{3N-6} \lambda_k{}^2 Q_k^2 \qquad \textit{eq. 2-11}$$

It reminisces the potential energy for a single harmonic oscillator (eq. 2-1). Applying the time-independent Schrödinger equation to each of the normal modes, we have:

$$\frac{-\hbar^2}{2}\frac{d^2\psi(Q_k)}{dQ_k^2} + \frac{1}{2}\lambda_k{}^2 Q_k^2 \psi(Q_k) = W(k)\psi(Q_k) \qquad k = 1,2 \dots 3N \qquad \textit{eq. 2-12}$$

Similar to the diatomic molecule problem, we have the solution for each of the normal modes (*57*):

$$\Psi_{nk}(Q_k) = \left(\frac{\lambda_k}{\pi\hbar}\right)^{1/4} \frac{1}{\sqrt{2^n n!}} H_n(\xi) e^{-\xi^2/2} \qquad k = 1,2 \dots 3N \qquad \textit{eq. 2-13}$$

$$\mathrm{W}_{nk} = \hbar\lambda_k(n_k + 1/2) \qquad k = 1,2 \dots 3N \qquad \textit{eq. 2-14}$$

Again, where $\xi \equiv \sqrt{\frac{\lambda_k}{\hbar}} Q_k$. And λ_k is the vibrational frequency of normal mode *k*, which can be obtained as the eigenvalue of the Hessian matrix $\boldsymbol{F}$ in eq. 2-9. $|\Psi_{nk}(Q_k)|^2$ gives the possibility function of the normal mode *k* in terms of the normal coordination Q_k, at quantum state n. W_{nk} gives the corresponding energy of normal mode *k* at quantum state *n*.

Just as a vector in 3D space can be decomposed to 3 orthogonal vectors, a particular vibration of the molecule can be regarded as a vector and decomposed into 3*N*-6 orthogonal normal vibrations, corresponding to the coordination of $Q_1, Q_1, \dots, Q_{3N-6}$. From the other side, the superposition of these 3*N*-6 normal modes describes a particular vibration of the molecule. The wave function for this particular vibration corresponds to the multiplication of the 3*N*-6 wave functions $\Psi_{nk}(Q_k)$. And the total vibration energy corresponds to the addition of each individual energy state:

$$W = \sum_{k=1}^{3N-6} \hbar\lambda_k(n_k + 1/2) \qquad \textit{eq. 2-15}$$

The quantum state for particular vibration can be denoted by the 3*N*-6 number: $n_1 n_2 n_3 n_4 \dots n_{3N-6}$. For example, a water molecule (3 atoms) has 3 vibration modes (3×3-6), and the vibrational state of the water molecule can be written as 3 integers: $n_1 n_2 n_3$. The lowest energy state (ground level) is denoted as 000. The absorption causing the one-level transition of a single vibration mode is called fundamental level absorption, for example, the transition from 000 to 001, or 000 to 100. The absorption causing the transition across more than one level, for example, 000 to 020, is called overtone absorption.

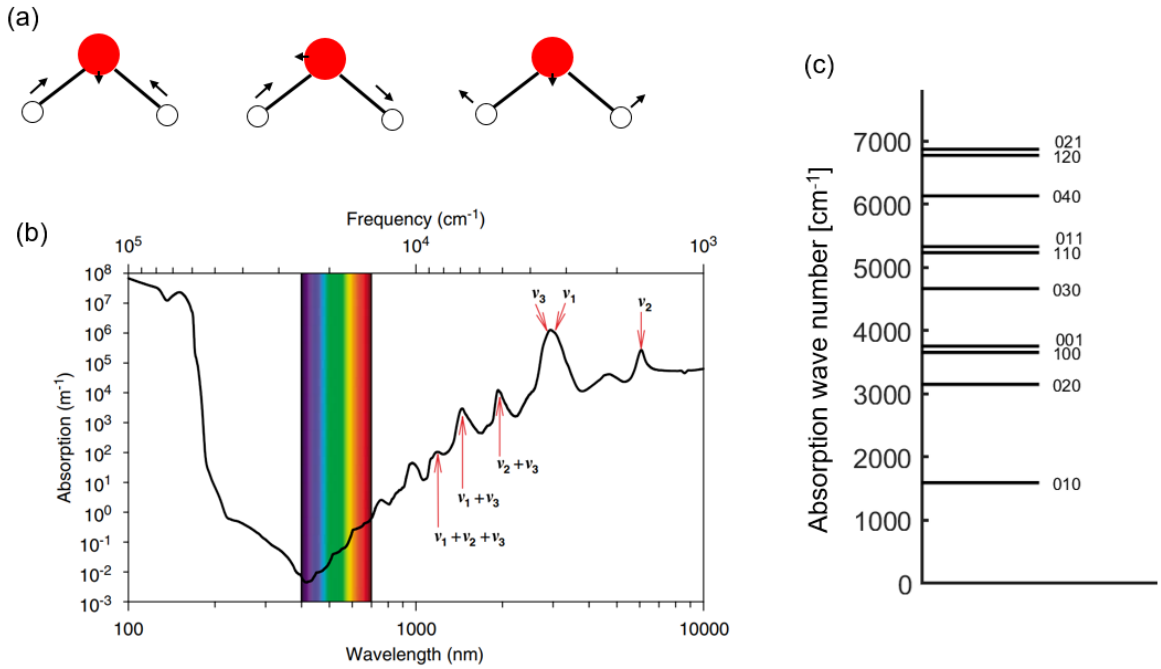

Fig. 2-4. Normal vibration modes of water.(a) Three normal vibration modes of water: symmetric stretching, asymmetric stretching, and bending. (b) Water spectrum. (c) Vibrational absorption energy levels, denoted by vibrational wavenumber (*58*, *59*).

Table 2-1: Quantum states of water and their corresponding energy levels.

$n_1n_2n_3$	Wavenumber [cm^{-1}]	$n_1n_2n_3$	Wavenumber [cm^{-1}]
000	0	030	4666.790
010	1594.746	110	5234.978
120	3151.630	011	5331.265
100	3657.053	040	6134.015
001	3755.929	…	…

Ref.: (*58*).

When solving the vibrational problem of a symmetric polyatomic molecule with a large number of atoms, two or more of the normal modes might share the same vibrational frequency, this is called normal mode degeneration. This degeneration suggests that the number of normal modes for a nonlinear molecule can be far less than 3*N*-6. Nevertheless, the absorption spectrum is still complicated due to the overtone absorption, and the fine structure of the absorption band can be observed when using high resolution spectroscope (<1 cm^{-1}). This fine structure originates from the vibrational transition of different rotational states (see **Fig. 2-3**), which involves significantly low energy. This vibrational-rotational absorption is especially clear in the gaseous compounds (HCl or water vapor for instance).

2.2.3 Typical biological vibrational absorption bands

Over the past century, IR spectroscopy has developed into a mature technology for chemical analysis of materials based on the vibrational absorption of molecules. A vast number of IR spectra from various organic chemical compounds have been collected following the invention of different types of IR spectrometers, which work by detecting transmitted light. Among the data collected, an important discovery is that specific functional groups in chemical compounds typically absorb IR light at specific wavenumbers. For instance, the vibration of the methylene group, which exists in alkanes, fatty acids, and triglycerides, consistently results in CH stretching absorption peaks around 3000 – 2800 cm^{-1}. The carbonyl group, present in ketones, aldehydes, and acids, primarily exhibits absorption peaks around 1730 cm^{-1}. Additionally, the amide group, found in proteins, consistently displays two absorption peaks around 1550 and 1650 cm^{-1}, respectively. These distinct absorption peaks serve as unique features of biological compounds, making infrared (IR) spectroscopy a powerful tool for nonperturbative and label-free analysis of biological samples.

A significant absorption peak requires several characteristics. Firstly, the absorption band must exhibit sufficient intensity to be easily identified. Secondly, it should be situated in a spectrum region where it does not overlap with other absorption peaks. Lastly, the peak should possess a narrow bandwidth that

enables the detection of subtle shifts resulting from different molecular structure contexts. The MIR spectrum regions is usually divided into 4 regions: X-H stretching region (4000-2500 cm^{-1}), the triple-bond region (2500 – 2000 cm^{-1}), the double bond region (2000 – 1500 cm^{-1}) and fingerprint region (1500 – 600 cm^{-1}) (*60, 61*).

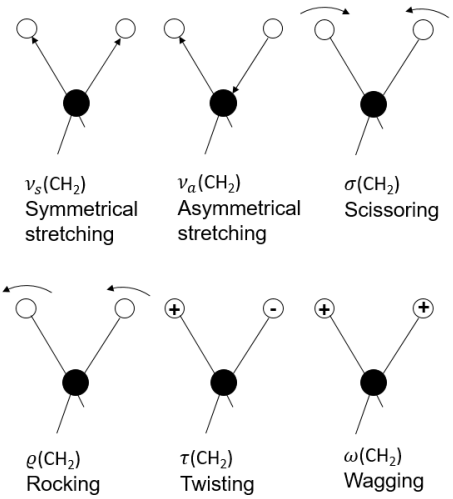

Fig. 2-5. **Vibrations of methylene group.**

One of the most useful diagnostic bands for determining the presence of a methylene group is the CH stretching absorption, located in the range of 2800 – 3000 cm^{-1}. It serves as a hallmark for lipids in tissues since lipids typically contain a long chain of methylene groups. The symmetric stretching vibration of methylene involves the simultaneous lengthening or shortening of the two CH bonds in the methylene group (see **Fig. 2-5**). This symmetric stretching leads to the absorption band of around 2855 ± 10 cm^{-1}. (see Table 2-2). The asymmetric stretching of methylene involves the lengthening of one CH bond and the shortening of the other bond, resulting in an absorption band around 2926 ± 10 cm^{-1}. These two absorption bands dominate the region of 2800 – 3000 cm^{-1}. Although the asymmetric and symmetric vibrational absorption peaks of the methyl group are present in a similar location, their corresponding absorption peaks are relatively small in biological samples due to their lower abundance (usually found at the end of the chain).

Table 2-2. Vibrational absorption wavenumber of CH bonds.

	Vibration	Wavenumber range [cm^{-1}] *(61)*
Stretching	CH_3 Asymmetric	2962 ± 10
	CH_3 Symmetric	2872 ± 10
	CH_2 Asymmetric	2926 ± 10
	CH_2 Symmetric	2855 ± 10
bending	C-CH_3 Asymmetric bend	1460 ± 10
	C-CH_3 Symmetric bend	1375 ± 10
	C-CH_2 Scissors	1455 ± 10
	C-CH_2 Rocking	720 ± 10

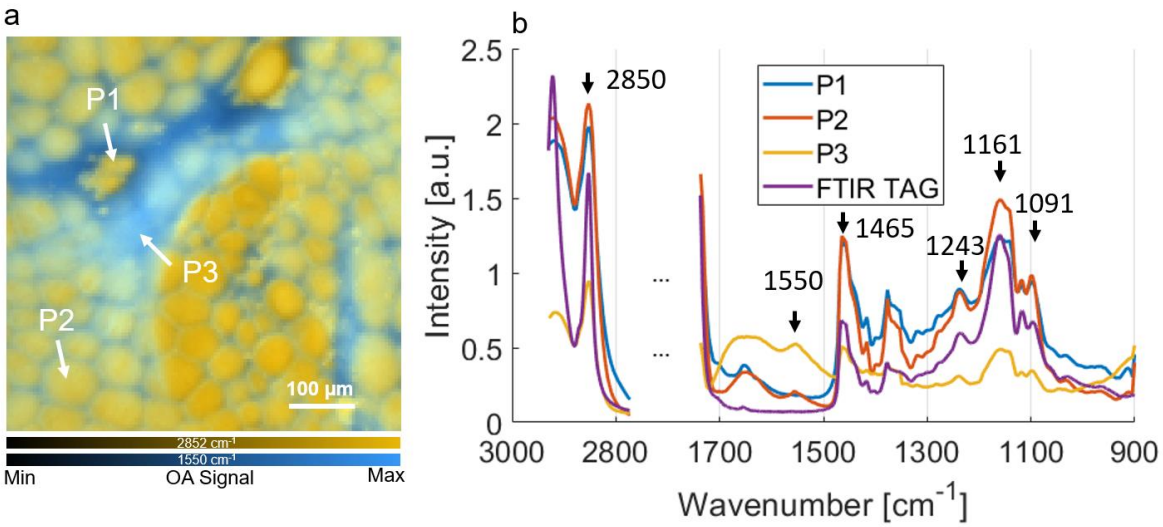

Fig. 2-6. Comparison of spectra obtained from adipose tissue and synthetic triglyceride (TAG). **a**, The mid-infrared optoacoustic microscopy (MiROM) (*62*) image of the adipose tissue. **b,** Spectra of adipose tissue obtained from the MiROM image (acquired from locations as marked by the arrows), and the spectrum of synthetic triglyceride acquired by FTIR. OA: Optoacoustic.

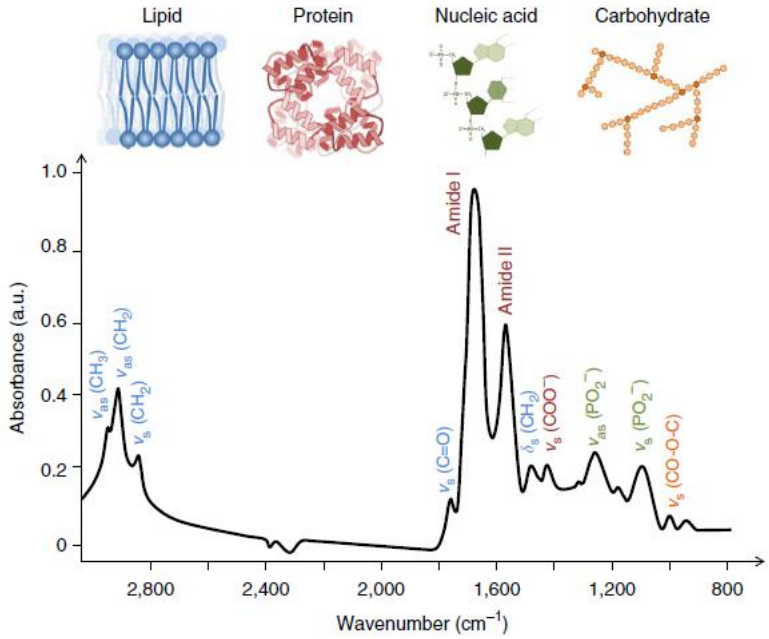

Fig. 2-7. Absorption peaks of typical biological spectrum. Absorption peaks of typical biological spectrum, where ν = stretching vibrations, δ = bending vibrations, s = symmetric vibrations and as = asymmetric vibrations (*63*).

Another important set of diagnostic bands in biological analysis is the absorption bands of the amides, located around 1650 cm^{-1} (amide I band) and 1550 cm^{-1} (amide II band), which are useful for determining the presence of proteins. Amides consist of a carbonyl group with a carbon atom attached to one side and a nitrogen atom attached to the other side. The absorption in the amide I band arises from the stretching of the carbonyl group and typically ranges from 1680 to 1630 cm^{-1}. The amide II

band is contributed by the N-H bending vibration (40-60%) and the C-N stretching vibration (18-40%) (*64*).

Table 2-3. Vibrational absorption wavenumber of typical bimolecular groups.

Functional group	Wavenumber range [cm^{-1}] *(61)*
Amide	1680-1630
Carboxylic acid	1725-1700
Ester	1750-1725

2.3 Mid-infrared optothermal effect and single-pulse optothermal decay

Vibrational absorption results in the change of internal energy U of the sample. After vibrational absorption, in an infinitesimal volume element $d\tau$ of the absorber, the increase of internal energy ΔU and its temperature change ΔT can be correlated with the thermal capacity C as follow:

$$\Delta T = \frac{\Delta U}{C} \qquad \textit{eq. 2-16}$$

It suggests that absorption of mid-infrared light leads to the temperature increase – the mid-infrared optothermal effect. Since the temperature change is linearly correlated with the internal energy gain, i.e., linearly correlated with vibrational absorption, one can measure the temperature change to obtain the vibrational absorption spectrum, or measure the temperature map to obtain vibrational absorption image.

2.3.1 Heat equation

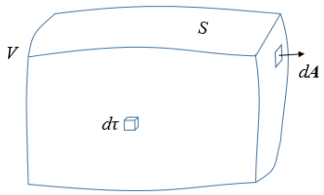

Fig. 2-8. Region of volume in a thermal conductive body. $d\boldsymbol{A}$ is a vector on surface with its direction outward.

A long and continuous illumination of water can create an optothermal lens, which has been discussed in other works (*18*). In this study, a very short pulse (~10 ns) MIR laser will be used for optothermal excitation. The absorption process can be considered as an instantaneous process, so our focus lies in solving the heat conduction problem that occurs after the completion of absorption. Specifically, we aim to determine the spatial and temporal dependence of the temperature field T in a large volume V (refer to **Fig. 2-8**). Using $\boldsymbol{x}$ as the position vector and t as time, our goal is to find a solution for:

$$T = T(\boldsymbol{x}, t) \qquad \textit{eq. 2-17}$$

According to Fourier's law, we know that the temperature field is associated with the heat flux (vector quantity, the magnitude defined as the rate at which heat is transferred per unit area, per unit time; and the direction normal to the unit area) $\dot{\boldsymbol{q}}$ by:

$$\dot{\boldsymbol{q}}(\boldsymbol{x}, t) = -\kappa \nabla T(\boldsymbol{x}, t) \qquad \textit{eq. 2-18}$$

Here κ is the thermal conductivity constant.

Moreover, we apply the energy conservation law to the volume V, i.e., the total internal energy change within this volume is equal to the net heat flux through the surface S of volume (There is no heat source after MIR absorption is complete):

$$-\frac{\partial \int_V dU}{\partial t} = \int_S \dot{\boldsymbol{q}}(\boldsymbol{x}, t) d\boldsymbol{A} \qquad \textit{eq. 2-19}$$

Here, the left part corresponds to the total internal energy change within volume V; the right part corresponds to the net heat flux through the enclosed surface S. The negative sign indicates that the positive heat flux (heat flow out) leads to reduction of internal energy. Where $dU = c\rho d\tau$. Using eq. 2-16 to eq. 2-19, we obtain the heat equation:

$$\frac{\partial T(\boldsymbol{x}, t)}{\partial t} \frac{1}{\alpha} = \nabla^2 T(\boldsymbol{x}, t) \qquad \textit{eq. 2-20}$$

Where α is the thermal diffusivity $\alpha = \frac{\kappa}{c\rho}$, and c is the specific heat capacity defined by the heat capacity C of the volume $d\tau$ divided by the mass of the volume $d\tau$: $c = C/(\rho d\tau)$, and ρ is the density. In the cylindrical coordinate, eq. 2-20 is written as:

$$\frac{\partial T}{\partial t} \frac{1}{\alpha} = \frac{1}{r} \frac{\partial}{\partial r} \left(r \frac{\partial T}{\partial r} \right) + \frac{1}{r^2} \frac{\partial^2 T}{\partial \phi^2} + \frac{\partial^2 T}{\partial z^2} \qquad \textit{eq. 2-21}$$

Here, r is the polar axis, z is the longitudinal axis, and ϕ denotes the angular coordinate as shown in **Fig. 2-9**.

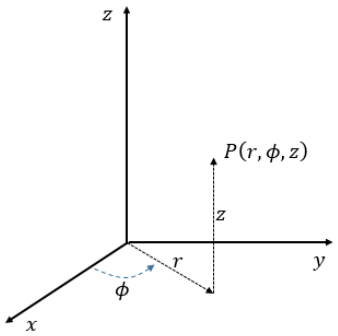

Fig. 2-9. Cylindrical coordinate system (r, ϕ, z).

2.3.2 Single-pulse optothermal decay in water

When we image cells using the optothermal technique, a portion of the energy will unavoidably be absorbed by water, while the energy absorbed by the cells will also inevitably be released into the water. Therefore, it is crucial to understand the spatial-temporal dependence of temperature following the absorption of a mid-infrared (MIR) pulse by water.

To formulate the problem, we take water as our sample, which is contained in a cylindrical dish. The bottom of the dish is made of a ZnS window to allow the transmission of mid-infrared light. Additionally, the water is covered with a cover glass to prevent evaporation. A pulse of the MIR beam, characterized by a Gaussian distribution, is directed into the water from the bottom. Our goal is to find the analytical solution for the temperature field T after the absorption of the MIR pulse is complete.

Here we use cylindrical coordinate system to solve the problem, in which we denote the contact surface between water and ZnS window as $z = 0$, as seen in **Fig. 2-10**. The planar distribution of the energy (energy per unit area, denoted by σ) can be considered as a Gaussian function (*18*):

$$\sigma(r, \phi, 0) = \frac{2E_0}{\pi R^2} \exp\left(-2\frac{r^2}{R^2}\right) \qquad \textit{eq. 2-22}$$

This is a aximuthal symmetric function that depends only on the polar axis r. Here, E_0 is the total energy of the pulse, and R is the radius of the beam (the distance from the propagation axis to where the intensity drops to $1/e^2$ of maximum intensity).

Due to the vibrational absorption, MIR energy distributes inside the sample as internal energy according to beer-lambert law. The planar energy density after MIR traveling length z is written as this relation: $\sigma(r, \phi, z) = \sigma(r, \phi, 0)exp(-\mu z)$, where μ is the absorption coefficient. The negative of partial

derivative of the relation with respect to z gives the energy volume density (internal energy per unit volume) in sample $D(r, \phi, z)$, caused by MIR absorption:

$$D(r, \phi, z) = \mu\sigma(r, \phi, 0)\exp(-\mu z), \qquad \text{for } z > 0 \qquad \textit{eq. 2-23}$$

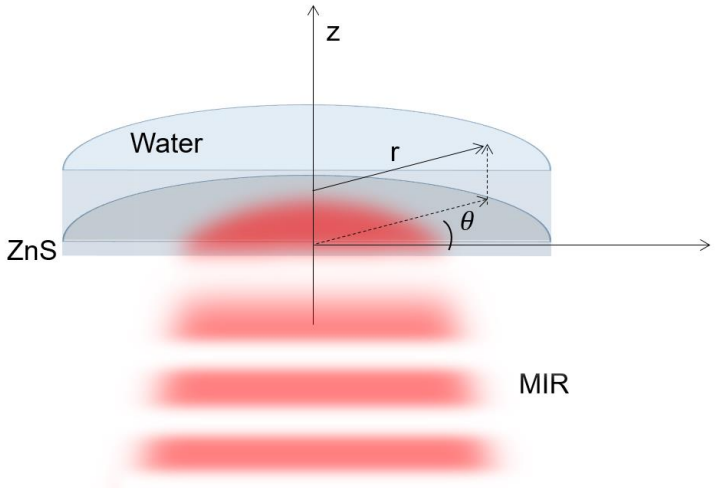

Fig. 2-10. Cylindrical coordinate system for the single-pulse optothermal decay problem. The MIR pulse irradiates the water from the bottom through the ZnS window. The contact surface between water and ZnS window is denoted as z=0. (Assume that no MIR light is absorbed in ZnS window.)

The volume density of internal energy is an r and z dependent function, independent of ϕ. It can be used to calculate the temperature gain T_0 in the water after the absorption of the pulse is complete:

$$T_0(r, \phi, z) = \frac{D(r, \phi, z)}{c\rho}, \qquad z > 0 \qquad \textit{eq. 2-24}$$

We take this temperature gain as the initial condition for optothermal decay problem. eq. 2-25 to eq. 2-29 formulated the initial condition for the optothermal decay problem. The problem we are going to solve is confined to the dish region: $0 < r < a, 0 \leq \phi < 2\pi,\ 0 < z < b$, where a is the radius of the dish, and b is the thickness of the water volume in the dish. To simplify the problem, we assume that the ZnS window (located at $z = 0$) and glass window (located at $z = b$) are insulated materials, and the heat is dissipating by the dish wall into the environment. And the wall keeps the temperature of the environment, which is assumed to be 0.

$$\frac{1}{r}\frac{\partial}{\partial r}\left(r\frac{\partial T}{\partial r}\right) + \frac{\partial^2 T}{\partial z^2} = \frac{1}{\alpha}\frac{\partial T}{\partial t}, \qquad 0 < r < a, \qquad 0 < z < b, \qquad t > 0 \qquad \textit{eq. 2-25}$$

$$T = 0, \qquad r = a, \qquad t > 0 \qquad \textit{eq. 2-26}$$

$$\frac{\partial T}{\partial z} = 0, \qquad z = 0, \qquad t > 0 \qquad \textit{eq. 2-27}$$

$$\frac{\partial T}{\partial z} = 0, \qquad z = b, \qquad t > 0 \qquad \textit{eq. 2-28}$$

$$T_0(r, \phi, z) = \frac{2\mu E_0}{c\rho\pi R^2} \exp\left(-2\frac{r^2}{R^2} - \mu z\right), \qquad 0 < r < a, \qquad 0 < z < b, \qquad t = 0 \qquad \textit{eq. 2-29}$$

Here eq. 2-25 states the heat equation, eq. 2-26 to eq. 2-28 states the boundary conditions, and eq. 2-29 states the initial condition. The problem can be solved using the separation of variables, $T(r, z, t) = R(r)Z(z)\Gamma(t)$, which results in two eigenvalue problems. The general solution is written as (*65*):

$$T(r, z, t) = \sum_{m=1}^{\infty} \sum_{p=1}^{\infty} c_{mp} R_0(\beta_m, r) Z(\gamma_p, z) e^{-\alpha(\beta_m^2 + \gamma_p^2)t} \qquad \textit{eq. 2-30}$$

Where, $R_0(\beta_m, r)$, $Z(\gamma_p, z)$, and $e^{-\alpha(\beta_m^2+\gamma_p^2)t}$ are the solutions for $R(r)$, $Z(z)$, and $\Gamma(t)$. β_m and γ_p are discrete separation constants with the order of m and p (integral number = 1, 2, …). c_{mp} is a series of values determined by:

$$c_{mp} = \frac{1}{N(\beta_m)N(\gamma_p)} \int_0^a \int_0^b r R_0(\beta_m, r) Z(\gamma_p, z) T_0(r, z, 0)\, dr dz \qquad \textit{eq. 2-31}$$

Where $N(\beta_m)$ and $N(\gamma_p)$ are the normalization factors of $R_0(\beta_m, r)$ and $Z(\gamma_p, z)$, which are given by:

$$\frac{1}{N(\beta_m)} = \frac{\pi^2}{2} \frac{\beta_m^2}{1 - J_0^2(\beta_m a)} \qquad \textit{eq. 2-32}$$

$$\frac{1}{N(\gamma_p)} = 2\frac{\gamma_p^2 + 1}{b(\gamma_p^2 + 1) + 1} \qquad \textit{eq. 2-33}$$

Where $J_0(\beta_m r)$ is the Bessel functions of order 0 of the first kind.

Moreover, $R_0(\beta_m, r)$, $Z(\gamma_p, z)$ are given by:

$$R_0(\beta_m, r) = J_0(\beta_m r) Y_0(\beta_m a) - J_0(\beta_m a) Y_0(\beta_m r) \qquad \textit{eq. 2-34}$$

$$Z(\gamma_p, z) = cos(\gamma_p z) \qquad \textit{eq. 2-35}$$

Where $Y_0(\beta_m r)$ is Bessel functions of order 0 of second kind.

Finally, according to boundary conditions, the value β_m and γ_p are given by solving the equations:

$$R_0(\beta_m, a) = 0 \qquad \textit{eq. 2-36}$$

$$\frac{\partial Z(\gamma_p, z)}{\partial z} = 0 \qquad \textit{eq. 2-37}$$

Chapter 3 Working principle of wide-field optothermal microscopy

3.1 Pump-probe imaging concept

Equipped with the basic knowledge of vibrational absorption, now we move on to introduce the imaging concept of wide-field optothermal microscopy proposed in this thesis. As shown in **Fig. 3-1**, wide-field optothermal microscopy is a pump-probe imaging approach, where MIR light works as a pump beam, and visible (VIS) light works as a probe beam. The pump beam illuminates a large area (for instance, an area of 5×10^5 μm^2, or c.a. 700×700 μm^2) of the sample plane to excite optothermal effect. A phase imaging system - can be Zernike phase contrast (ZPC) microscope, differential interference contrast (DIC) microscope, or quantitative phase imaging tool - is implemented to capture the refractive index change of the sample due to the following thermo-optic effect (temperature change induces refractive index change).

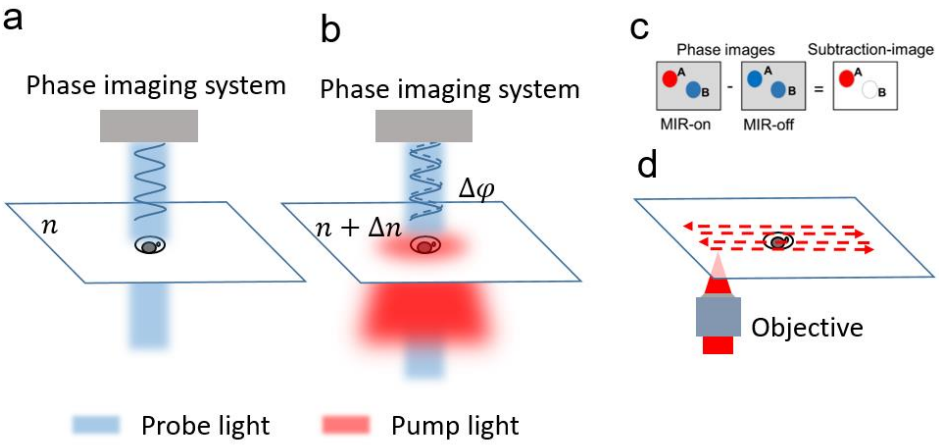

Fig. 3-1. Imaging concept of wide-field optothermal microscopy. a, Acquisition of MIR-OFF image. **b,** Acquisition of MIR-ON image. **c,** Subtraction of two phase images (MIR-ON minus MIR-OFF) illustrate the molecular vibration contrast (chemical-contrast) of the sample. **d**, For comparison, the focal excitation requires raster scanning for an image.

For the purpose of optothermal imaging, two phase images are required: a MIR-OFF image acquired without MIR illuminating the field-of-view (FOV) (**Fig. 3-1**a), and another MIR-ON image acquired with MIR illuminating the FOV (**Fig. 3-1**b). The MIR-OFF images are later subtracted from the MIR-ON image, as shown in **Fig. 3-1**c, to obtain the optical path difference (OPD), which is related to the refractive index change. The more energy absorbed by the sample, the more significant the OPD, and the higher the contrast will be shown in the subtraction image. By detecting the OPD over the FOV, we are able to obtain the localized absorption coefficient, thus a MIR chemical-contrast image. For example, in the cartoon demonstration shown in **Fig. 3-1**c, subtracting the MIR-OFF image from the MIR-ON

image produces a subtraction image that represents the optical path difference caused by MIR illumination. In a FOV where there is a high MIR absorption sample "A" and a low MIR absorption background "B", the subtraction image exhibits high contrast for "A" and low contrast for "B".

There are several advantages associated with this imaging concept. Firstly, pump-probe detection can result in better imaging resolution compared to vibrational spectral imaging techniques that only utilize a pump, such as Fourier-transform infrared spectroscopy (FTIR) and mid-infrared optoacoustic microscopy (MiROM). This is because the image resolution in pump-probe detection is determined by the wavelength of the visible light (probe) rather than the mid-infrared light (pump). Secondly, in comparison to point-by-point scanning schemes like stimulated Raman scattering microscopy (SRS) (*37*) and MiROM (*62*), where the pump beam is focused into a diffraction-limited spot (**Fig. 3-1**d), wide-field irradiation eliminates the need for mechanical scanning. The acquisition time for a single chemical contrast image (which depends on the exposure time of the camera and the time interval between MIR-ON and MIR-OFF images) can be significantly shorter than that of point-by-point scanning methods. Finally, the power flux density of the pump on the sample can be greatly reduced compared to focal excitation methods, thereby minimizing potential photodamage during measurements on living cells (*40*).

3.2 Relation between absorption coefficient and MIR-phase

To bring the imaging concept into reality, it is important to establish the analytical relation between the absorption coefficient and the phase change induced by MIR absorption (i.e., MIR-phase).

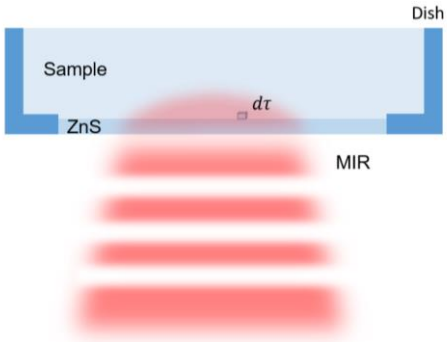

Fig. 3-2. Illumination of MIR beam on the sample. Due to the absorption, the MIR beam exponentially decreases as it penetrates the sample. To simplify the discussion, we take a small volume $d\tau$ that is close to the bottom surface.

In the MIR-ON case, when the MIR light (at specific wavenumber k) illuminates the sample, a local change of temperature is generated in the sample. Consider an infinitesimal volume $d\tau$ of the sample that really close to the illumination surface (see **Fig. 3-2**), $d\tau$'s temperature will increase due to the vibrational absorption, with an absorption coefficient of μ_k. Let $\Delta T = T1 - T0$ be the temperature

difference before (denotes as $T0$) and after (denotes as $T1$) the MIR pulse is absorbed by the sample, ΔT can be written as (*52*):

$$\Delta T_{(\vec{r},k)} = \frac{\Delta Q_{(\vec{r},k)}}{c\ m} = \frac{\mu_k E_{\vec{r}}}{cA\ \rho} \qquad \textit{eq. 3-1}$$

Where $\vec{r}$ is a coordinate vector denotes the position of the infinitesimal volume $d\tau$; $\Delta Q_{(\vec{r},k)}$ is the amount of heat generated in $d\tau$; m is the mass of sample within $d\tau$; c is the specific heat capacity of sample; ρ is the mass density of sample; $E_{\vec{r}}$ denotes the amount of MIR pulse energy that reach to the bottom of the infinitesimal volume; A is the area of the bottom surface of infinitesimal volume; μ_k is the vibrational absorption coefficient of the sample at wavenumber k. The increase in temperature results in a change in the refractive index Δn within the infinitesimal volume $d\tau$ of the sample due to the thermo-optic effect,

$$\Delta n_{(\vec{r},k)} = \frac{dn}{dT}\Delta T_{(\vec{r},k)} = \delta \Delta T_{(\vec{r},k)} \qquad \textit{eq. 3-2}$$

And also results in a change of its thickness due to thermal expansion,

$$\Delta l_{(\vec{r},k)} = \frac{1}{l}\frac{dl}{dT}\Delta T_{(\vec{r},k)} l = \beta l \Delta T_{(\vec{r},k)} \qquad \textit{eq. 3-3}$$

Where in *eq. 3-2*, $\delta = \frac{dn}{dT}$ is the thermo-optic coefficient and in *eq. 3-3*, $\beta = \frac{1}{l}\frac{dl}{dT}$ is linear thermal expansion coefficient of the sample, and l is the thickness of $d\tau$. Consequently, since the change of the refractive index and the thickness are proportional to the temperature, there will be a net optical path length difference in the sample:

$$\begin{aligned} OPD &= [(n + \Delta n)(l + \Delta l) - nl] \\ &\approx l\Delta n + n\Delta l \\ &= l\delta\Delta T + n\beta l\Delta T \end{aligned} \qquad \textit{eq. 3-4}$$

Assume the wavelength of the visible probe light is λ, one can convert this OPD to the phase difference, using:

$$\Delta\varphi = \frac{2\pi OPD}{\lambda} \qquad \textit{eq. 3-5}$$

Table 3-1. Physical properties of typical samples.

	Water	**Glycerol**	**TAG**	**ZnS**	**Air**
Specific heat capacity (c) *[J/g°C]*	4.18	2.43	2.08-2.15	0.469	1.0035 at 0 °C
Density (ρ) *[g/m^3]*	10^6	1.26×10^6	0.9×10^6	4.09×10^6	1.1839×10^3 at 25 °C
Thermo-optic coefficient (dn/dT) *[1/°C]*	-1.2×10^{-4}	-2.25×10^{-4}	-3.66×10^{-4}	6.6×10^{-6}	-
Thermal expansion coefficient ($dl/(ldT)$) *[$\times10^{-6}$ K^{-1}]*	69	152	100-200	-	-
Refractive index (n)	1.33	1.474	1.473	2.38 at 553 nm	1.00029
Absorption coefficient (μ) *[m^{-1}]*	10^5-10^6 at 3.3 µm	-	2-3x10^3 at 3.5 µm	0.02	-
Thermal diffusivity (α) *[m^2/s]*	1.43×10^{-7} at 25 °C	-	8.38×10^{-8}	-	2.17×10^{-5} at 20 °C

Ref.: (*66*) (*67*) (*68*).

The relation between vibrational absorption coefficient μ_k and MIR-phase $\Delta\varphi$ of a PSOM image is linearly correlated using eq. 3-1 to eq. 3-5 (the deduction follows Zhang's work in (*52*)):

$$\frac{2\pi E_{\vec{r}}}{\lambda A}\frac{(l\delta + nl\beta)}{c\rho}\mu_k = \Delta\varphi_{(\vec{r},k)} \qquad \textit{eq. 3-6}$$

Here, the term $\frac{2\pi E_{\vec{r}}}{\lambda A}$ is system dependent, and the term $\frac{(l\delta+nl\beta)}{c\rho}$ is sample dependent. For a given sample at a given system, $\frac{2\pi E_{\vec{r}}}{\lambda A}\frac{(l\delta+nl\beta)}{c\rho}$ is a constant (can be denoted as s) and eq. 3-6 can be written as a linear relation $s\mu_k = \Delta\varphi_k$. Therefore, the MIR-phase is only wavelength dependent, and the MIR absorption spectrum can be obtained from MIR-phase image, by changing the MIR wavelength.

To estimate magnitude order of OPD in eq. 3-4. Taking into account the typical values of organelle size (~ 1 µm), thermos-optic coefficient (-1.2×10^{-4} [1/°C], for water), and thermal expansion coefficient (6.9×10^{-3} [1/°C], for water), the OPD due to the MIR absorption can be calculated to be in the scale of few nanometers per degree (1 - 10 nm/°C).

Chapter 4 Development of probe systems

In addition to the wide-field illumination, an important module in wide-field optothermal microscopy is a phase imaging system (see **Fig. 3-1**), for the purpose of probing the phase difference introduced by MIR absorption (i.e., MIR-phase). This chapter introduces the development of two custom-made phase image methods that will be used in the next two chapters for detecting MIR-phase: Condenser-free Zernike phase contrast microscopy (CF-ZPC) and phase-shifting microscopy (PSM).

4.1 Condenser-free Zernike phase contrast microscopy (CF-ZPC)

In a theory proposed by Ernst Abbe, the image of the microscope is considered as the interference effect of a diffraction phenomenon. The two bunches of interference beams originate from the interaction of microscopic illumination and sample. Here, the illumination beam is split into two types – the light rays that travel through the sample are deviated by the sample (termed deviated light) and the light rays that travel through the surrounding of the sample keep their original direction (termed surrounding light).

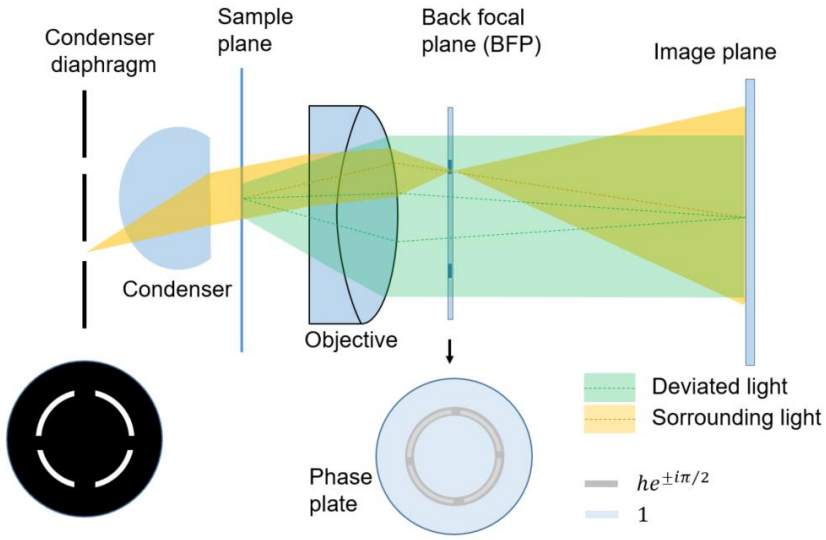

Fig. 4-1. **Diagram of the light propagation in a traditional Zernike phase contrast microscopy for a finite length corrected objective.** The light from the ring shaped light source is collimated by a condenser, creating the Köhler illumination for the microscope. On the sample plane, the ray that interacts with the sample deviates away from its propagation path (dashed green rays, for example), and is focused on the image plane. While the ray that does not interact with the sample (surrounding light) keeps its propagation direction (dashed orange ray, for example), and is focused at the back focal plane of the objective. The phase contrast enhancement is carried out by a phase plate located at the back focal plane of the phase contrast objective. In this phase plate, a ring structure is designed for attenuating the undeviated light intensity and retarding its phase. The modified undeviated light and deviated light are overlapped and interfere on the image plane. The interferogram produces the phase contrast image of the transparent sample.

After the light traveling the whole optical system, it reach to the camera sensor or the human's retina, where the deviated light and surrounding light are overlapped and interfere with each other. The interferogram forms an image of the sample. Exploiting this concept, Frits Zernike proposed a contrast enhancement design for transparent samples, which otherwise invisible by the camera or eyes. This imaging technique was later widely used in biology (*69*, *70*). This contrast enhancement design works by placing a phase plate on the Back Focal Plane (BFP) of the objective, where the deviated light and surrounding light are spatially separated. The phase plate possesses a ring (in the case of ring illumination) that covers the undeviated light to alter its intensity (c.a. 80% attenuation) and phase (change the phase by $+\frac{\pi}{2}$ or $-\frac{\pi}{2}$), to optimize (constructed or destructed) interference on the sample plane (see **Fig. 4-1**). The working principle of Zernike phase contrast microscope hasn't changed much since it was invented. The main effort in developing new generations of ZPC has been focused on the "halo" and "shade-off" artifacts, where structure illumination or special phase plates have been designed for minimizing the artifact (*71-73*). Despite the variant design, phase contrast microscopy generally uses a high NA (for instance, NA=1.25) condenser to create the Köhler illumination for the sample. Due to the high numerical aperture, this condenser works extremely close to the bottom of sample, which is a hinder to introduce extra illumination, for example, MIR illumination. This problem can be circumvented by adopting the condenser-free illumination as shown in **Fig. 4-2**.

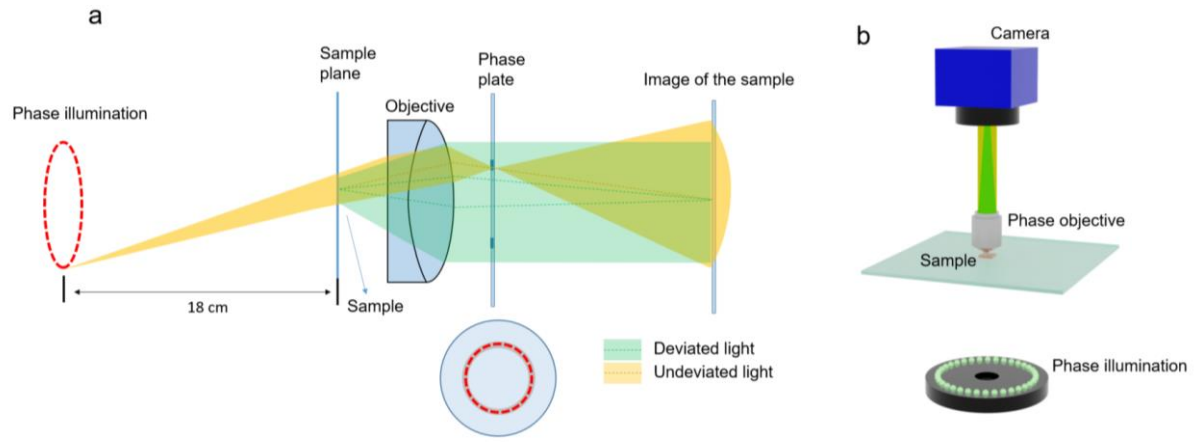

Fig. 4-2. Condenser-free phase contrast microscope. a, Diagram of the light rays propagation in CF-ZPC. **b,** 3D cartoon drawing of CF-ZPC. Compared with traditional ZPC, the condenser lens is replaced by a phase illumination - a ring of white LEDs. The LEDs ring is located at 18 cm away from the sample on a conjugate plane of the phase ring. On the back focal plane, the image of LEDs is projected on the phase ring of the phase plate.

The condenser-free phase contrast microscope (CF-ZPC), applies a distance (18 cm away from the sample plane in our case, as shown in **Fig. 4-2**) phase illumination for the microscope. The phase illumination consists of discrete point sources (white LEDs in our case, Aura Phase Contrast Illuminator

(*74, 75*)) with a ring of 20 cm in diameter. And the illumination ring was placed on the conjugate plane of the phase plate.

Compared with the conventional Zernike phase contrast microscopy, the substitution of condenser would not change much the phase contrast image of the sample. This is because: Firstly, in the conventional Zernike phase contrast microscopy, the phase illumination – the ring of condenser diaphragm – is an illumination plane consisting of constituent non-coherence point sources. The reduction from an illumination plane to a limited number of point sources only reduces the image intensity since the illumination points from the plane are incoherent. To compensate for the intensity loss, one can increase the intensity of LEDs. Secondly, the large distance from the illumination source and sample ensures the illumination is nearly collimated, so that the surrounding light is focused on the BFP to fulfill the working condition for ZPC. In our case, for example, the divergence of the light in the FOV is around 0.83 mrad (calculated from the FOV of 150 μm and the LEDs distance of 18 cm).

Besides the mechanical modification (substitute the phase illumination), this thesis also analytically develop the phase-intensity relation (conversion relation of the phase information to intensity information by the system) and numerically simulate the phase imaging characteristic of CF-ZPC.

4.1.1 Thin sample phase-intensity relation

To understand the conversion between phase image and intensity image in ZPC (phase-intensity relation), we first consider a one dimensional periodic phase object on the sample plane that alters the transmitting light according to:

$$F = \mathrm{e}^{i\phi(x)} \qquad \textit{eq. 4-1}$$

Where x denotes the position in one-dimension, and $\phi(x)$ is a periodic function describing the phase of the object in the sample plane. When a plane wave (which can be denoted as unit 1, since its phase is constant regarding position) travels through this sample. eq. 4-1 describes the optical field just behind the sample. If this optical field is projected into the image plane, no contrast will be observed since its intensity is constant ($|F|^2 = 1$) everywhere. Considering the biological sample (for a thin sample such as a monolayer cell) retard the phase really small, Zernike made the approximation that the real part of F has unit value and is independent of location x. That is, F can be expressed by approximation of its Taylor expansion (*69*):

$$F \approx 1 + i\phi(x) \qquad \textit{eq. 4-2}$$

Where the unit 1 represents the surrounding light that travels directly to the sample plane, without phase and amplitude change. When the light field of eq. 4-2 travels through the objective, Fourier transform of eq. 4-2 can be used to calculate the optical field on BFP. Therefore, surrounding light will be focused in the BFP (This can be understood by: Fourier transform of 1 is a δ function). Zernike proposed a design to place a wave plate on BFP, altering the surrounding light by a factor of $he^{\pm i\pi/2}$ (see **Fig. 4-1**). Where h indicates the factor for changing the optical field's vibration amplitude, $\pm\pi/2$ indicates the phase change ($+\pi/2$ corresponding to positive phase contrast, $-\pi/2$ corresponding to negative phase contrast). So in the image plane, instead of an identical optical field, it becomes (consider magnification of microscope = 1):

$$F' \approx he^{i\pi/2} + i\phi(x) \qquad \textit{eq. 4-3}$$

Taking the square of eq. 4-3, we obtain the intensity of this one-dimensional "image", which states phase-intensity relation (neglected the high order term ϕ^2 since ϕ is small):

$$|F'|^2 \approx -h^2 - 2h\phi(x) \qquad \textit{eq. 4-4}$$

One notice that after using the phase plate, intensity is linearly related to the phase variation $\phi(x)$. Where the parameter h can be carefully chosen so that the intensity of surrounding light h^2 is comparable with the intensity of deviated light $2h\phi(x)$, to enhance the image contrast.

4.1.2 Thick sample phase-intensity relation

Zernike phase contrast microscopy provides high contrast for the small phase variation in the sample since it aims for imaging small phase variation at the beginning. However, the linear phase-intensity relation of eq. 4-4 doesn't hold in practice, especially for thick samples that Zernike's approximation failed (in eq. 4-2). Here we look for a phase-intensity relation by considering all the higher-order terms in Taylor expansion. And validate this relation by simulation and experiments of thick samples. Firstly, here we write F as its full Taylor expansion, instead of eq. 4-2:

$$F = 1 + \sum_{n=1}^{\infty} \frac{(i)^n}{n!}\phi(x)^n \qquad \textit{eq. 4-5}$$

As discussed in the previous section, the unit 1 is multiplied by a factor of $he^{i\pi/2}$ to represent the modification of amplitude and phase of the surrounding light. The optical field in the image plane is:

$$F' = he^{i\pi/2} + \sum_{n=1}^{\infty} \frac{(i)^n}{n!} \phi(x)^n \qquad \textit{eq. 4-6}$$

One can obtain the following by adding and subtraction unit 1:

$$F' = he^{i\pi/2} - 1 + 1 + \sum_{n=1}^{\infty} \frac{(i)^n}{n!} \phi(x)^n \qquad \textit{eq. 4-7}$$

And wrap up the Taylor series at the end, we get:

$$F' = he^{i\pi/2} - 1 + \mathrm{e}^{i\phi(x)} \qquad \textit{eq. 4-8}$$

An analytical phase-intensity relation can be obtained:

$$|F'|^2 = (\cos\phi(x) - 1)^2 + (h + \sin\phi(x))^2 \qquad \textit{eq. 4-9}$$

Similarly, the negative phase plate provides the following relation:

$$|F'|^2 = (\cos\phi(x) - 1)^2 + (-h + \sin\phi(x))^2 \qquad \textit{eq. 4-10}$$

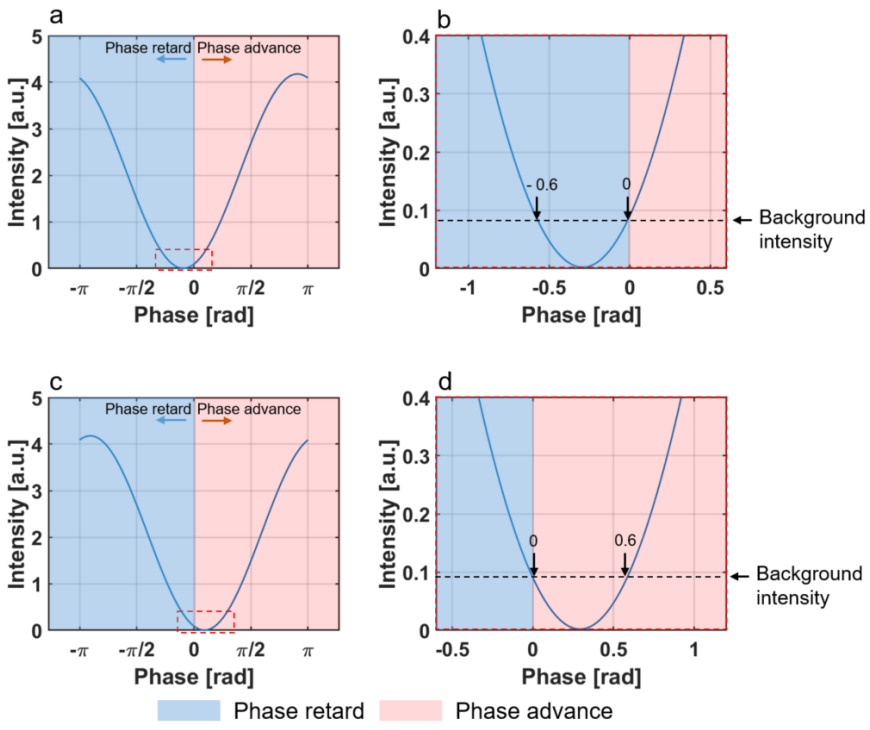

Fig. 4-3. Phase-intensity relation of Zernike phase contrast microscope. a,b, Positive contrast. **c,d**, Negative contrast. (b) and (d) are zoomed in region of (a) and (c), respectively, as marked by the red dashed areas. In this figure, we let h = 0.3.

The plots of eq. 4-9 and eq. 4-10 are shown in **Fig. 4-3**, using h = 0.3. According to the relations, for positive contrast, as shown in **Fig. 4-3**a,b, when ϕ is around -0.3 rad (phase retard of 0.3 rad), the intensity reaches its minimum. The minimum intensity is less than the intensity of surrounding light, in which the phase is not retarded ($\phi = 0$). Moreover, when ϕ is in the range of [-0.6 0] rad, the microscope renders the corresponding intensity darker than the surrounding area. When the phase is further retarded so that ϕ < -0.6, the microscope renders the image brighter than the surrounding area. This can be observed from a positive phase contrast image of cells and triglyceride (TAG) drops as shown in **Fig. 4-4**.

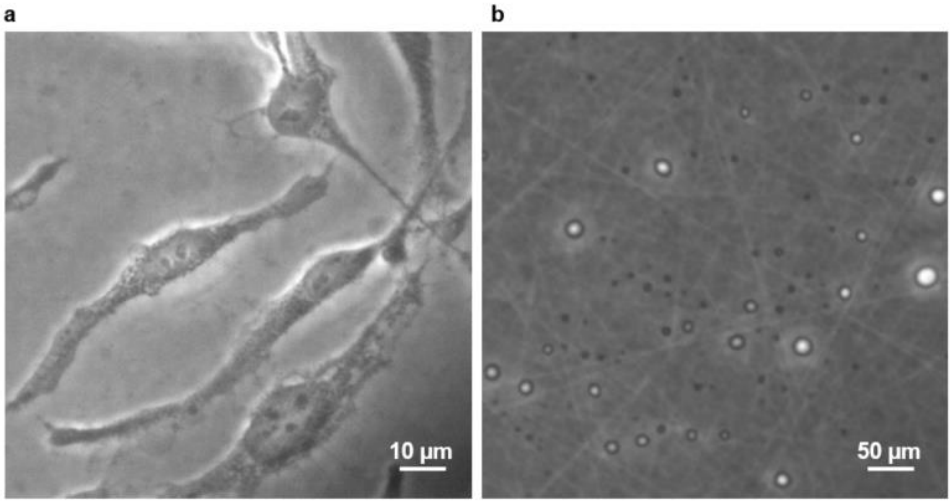

Fig. 4-4. CF-ZPC images of Hela cells and TAG drops via positive contrast objective. a, CF-ZPC image of Hela cells. **b,** CF-ZPC image of TAG drops. The cells illustrate weaker intensity (darker) compared with the background, since the cells are thin and the phase retardation localized between [-0.6 0] rad. For the TAG drops, the small ones are darker than the background due to small phase retardation while the bigger ones are bright in the center with a black region surrounded due to the large phase retardation.

4.1.3 Wavefront propagation simulation

To better understand the condenser-free Zernike phase contrast microscopy, we simulate the wavefront propagation of a CF-ZPC. This is performed by taking the advantage of its limited number of illumination point sources instead of unlimited point sources in conventional ZPC microscopy. In this simulation, we consider the point sources to be lighting from infinite, generating plane waves reaching to the sample plane. The monochromatic plane waves from each point source are independent (therefore, no interference between the plane waves), and obliquely propagate through the sample plane. The phase perturbation due to the sample (phase retardation by TAG droplet or phase advance by optothermal lens of water) is modeled based on the geometric and refractive index of the sample (see **Fig. 4-5**). The

wavefront along the traveling path is simulated by PROPER based on Fresnel approximation diffraction theory (*76*).

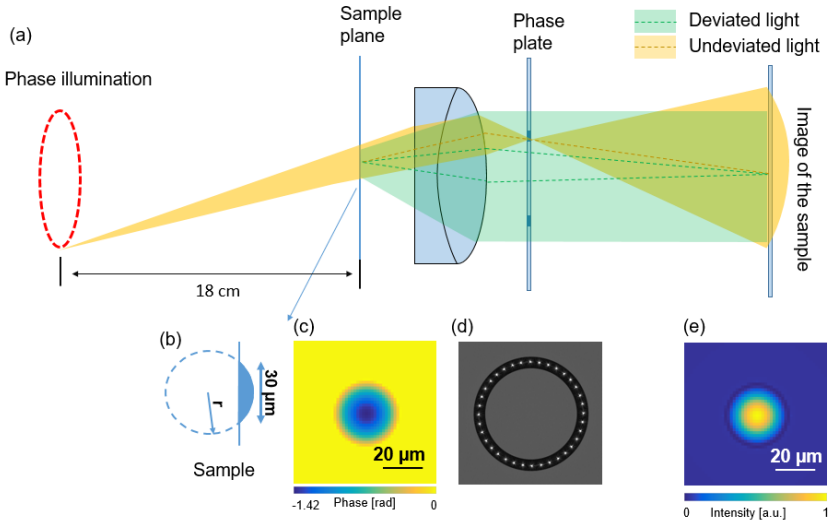

Fig. 4-5. Simulation of condenser-free Zernike phase contrast microscopy. (a) Diagram of the CF- ZPC. (b) The model of the sample (side view, blue shaded area). A micro lens model with a diameter of 30 µm, a curvature R of 0.002 μm^{-1}, is used to mimic a TAG (triglyceride) droplet. The micro lens model is part of a virtual sphere with diameter *r*. When a wavefront from the left travels through the micro lens, the phase of the wavefront retards according to the thickness of the micro lens. The light passing through the micro lens travels a longer optical path length $(n-1)d$ compared to which passing through the surrounding area, where *n* is the refractive index of micro lens, and *d* is the traveling distance. This optical path difference corresponds to phase retard of $\frac{2\pi(n-1)d}{\lambda}$, where λ is the wavelength of light, configurated as 500 nm in the simulation. The micro lens only retard the phase propagation wave, without intensity loss. (c) Phase retardation map of the micro lens of (b). (d) The intensity image of the back focal plane during the simulation, illustrating the image of point sources and their locations in the phase plate. (e) A phase contrast image of the sample model (b,c) (*77*).

The key in this simulation is to construct a phase plate in the BFP of the objective. In the simulation, the effect of the phase plate exerting on the wavefront is considered as a multiplication operation of the wavefront to a complex number $A(x,y)e^{i\varphi(x,y)}$, where $A(x,y)$ denotes the transmission factor of 2D phase plate, and $\varphi(x,y)$ denotes the phase perturbation of the 2D phase plate. According to previous discussions about the ZPC microscope, the phase ring should be designed as an attenuation ring to reduce the intensity of surrounding light, which is focused on this ring. So the transmission factor on the ring area is less than 1, determined by the parameter "h" discussed in section 4.1.1 and 4.1.2. The area outside the phase ring (complementary area) is preferred to transmit all the light, corresponding to the transmission factor of 1.

It is found that the transmission factor of the phase ring is preferred to be in the range of 0.3473 to 0.5 (corresponding to an intensity transmission ratio of 0.12 to 0.25, intensity ratio between transmit light and incident light) (*78*). We use a transmission factor of 0.39 (intensity transmission ratio 0.15) for our simulation. The positive and negative phase plate is classified based on the sign of phase perturbation from the phase ring: For a positive phase plate, the value of $\varphi(x,y)$ in the phase ring is a positive value: $+\frac{\pi}{2}$, while in a negative phase plate, it is negative value: $-\frac{\pi}{2}$. The value of $\varphi(x,y)$ in complementary area is 0 for both positive and negative phase plates, as shown in **Fig. 4-6**.

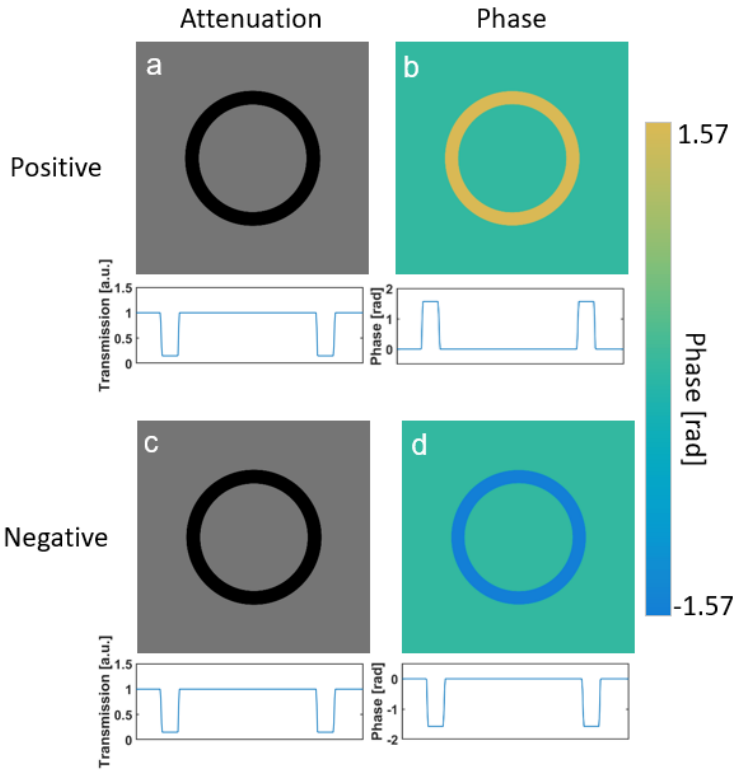

Fig. 4-6. Positive and negative phase plates. a,b, Transmission and phase perturbation of positive phase plate, and the line profile crossing the ring. **c,d**, Transmission and phase perturbation of negative phase plate and the line profile crossing the ring. Gray color indicates a transmission factor of 1, which means the light doesn't change its intensity when propagating through it. The black color indicates the intensity transmission factor of 0.15, which indicates that the propagating wave changes its intensity by a factor of 0.15 after traveling the phase plate.

Fig. 4-7 shows the simulation results when imaging the micro lens of **Fig. 4-5**b. The simulations with a positive phase plate, negative phase plate, and without phase plate are illustrated and compared. The intensity of the light in the back focal plane is shown in **Fig. 4-7**a-c, for the case of positive phase plate (a), negative phase plate (b), and no phase plate (c). The corresponding phase contrast images of the micro lens are shown in **Fig. 4-7**d-f. **Fig. 4-7**g illustrates the phase map of the sample. **Fig. 4-7**h plots the line profiles of the phase contrast image (d), (e), and the phase value in (g). Both positive phase contrast

(d) and negative phase contrast (e) give a clear image of the micro lens, which is unobservable under a bright field image (f), since the micro lens does not attenuate the light that travel through it.

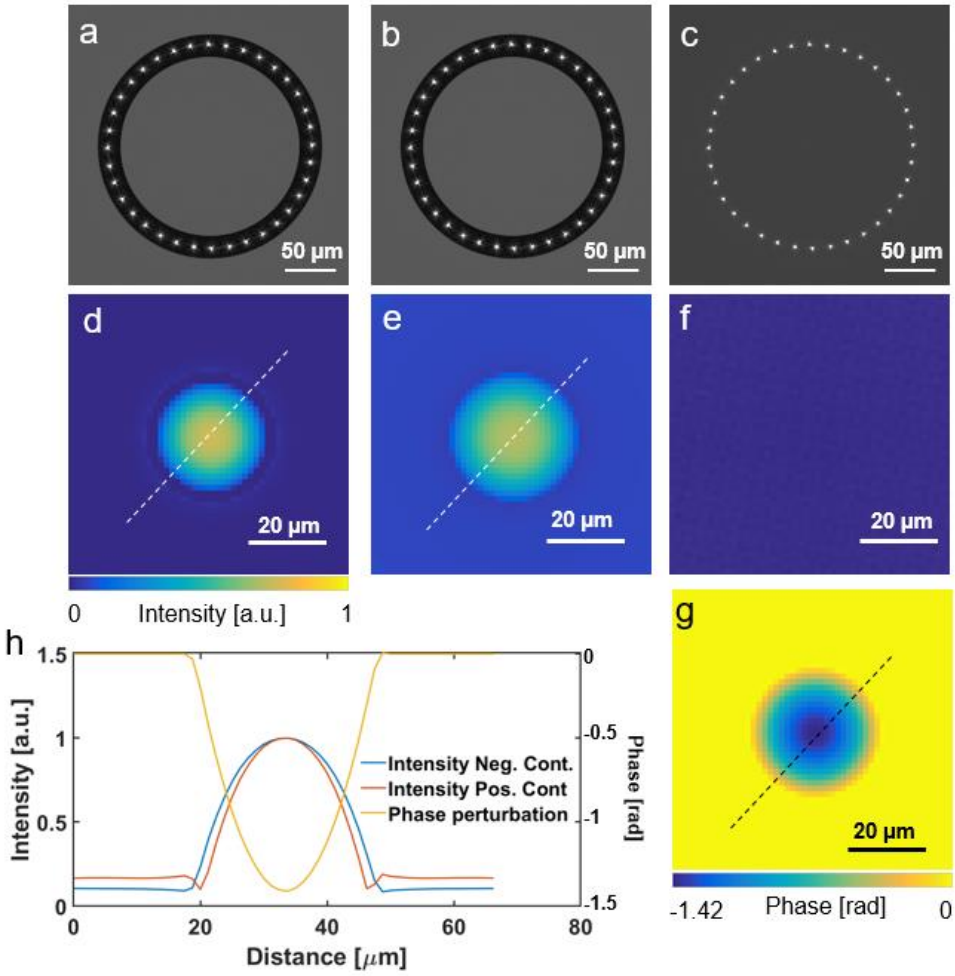

Fig. 4-7. Characterization of CF-ZPC by simulation. a,b, Intensity images of the back focal plane (location of phase plate) as the point source illuminating the microscope. (a) Positive contrast phase plate. (b) Negative contrast phase plate. **c,** Intensity image of the back focal plane when there is no phase plate (in a bright field microscope). **d-f,** Intensity images of the image plane using positive phase plate, negative phase plate, and no phase plate. **g,** The phase of the sample under this simulation, corresponds to a phase perturbation map caused by a micro lens sample as shown in **Fig. 4-5**b. **h,** Line profiles crossing the center of (d), (e), and (g), illustrating the intensity and phase perturbation.

The intensity of the phase contrast images can be understood according to ZPC's phase-intensity relations (eq. 4-9 and eq. 4-10) and its plots show in **Fig. 4-3**. On the edge of the micro lens, where the phase retardation is less than 0.6 rad, a lower intensity (compared with the surrounding) is observed in the positive phase contrast image (**Fig. 4-7**d). This lower-intensity area forms a dark ring surrounding the object. Outside this ring, a bright halo is found, which corresponds to the well know "Halo" artifact. We do not observe the dark ring from the image acquired with a negative phase objective (**Fig. 4-7**e).

This is because the phase-intensity relation given in **Fig. 4-3**c,d gives no minimum point in the phase retardation range ($\phi < 0$). When we compare the line profiles from positive and negative phase objectives. The negative contrast profile shows higher intensity, this can be explained by the right-shift of the phase-intensity curve of **Fig. 4-3**c compared with **Fig. 4-3**a.

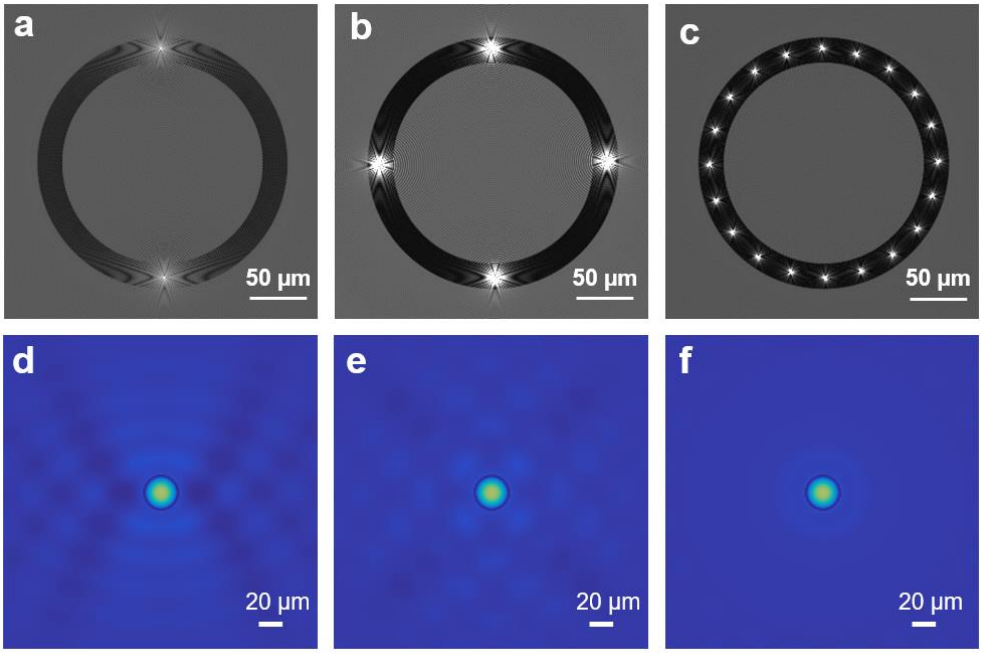

Fig. 4-8. Phase contrast imaging simulated from different illumination points. Top row (a-c): Intensity image of the back focal plane, in the case of 2-point sources, 4-point sources, and 20-point sources. The point sources illuminate the system independently so they do not interfere with each other. Bottom row (d-f): phase contrast images when using 2-point sources, 4-point sources, and 20-point sources. The phase contrast image is the summation of phase contrast images from each point source illumination. For example, (d) is the summation of two phase contrast images from 2-point sources in (a). The positive phase ring is used in the simulation.

Now we move on to study the effect of different light sources on CF-ZPC images. As shown in **Fig. 4-8**, the image of the micro lens does not change when using different numbers of point sources, varying from 2-point sources to 20-point sources. However, the surrounding area was rendered by an anisotropic pattern when a small number of point sources were used (**Fig. 4-8**d,e). This anisotropic pattern is mainly caused by the diffraction of the sample due to the inclined incident beam. The pattern is canceled out as the number of point sources increases and it is almost invisible under the illumination of 20-point sources. To further reduce this pattern, we used 36-point sources in our later results, and use 100-point sources in our real system. Corresponding experimental results as shown in **Fig. 4-8** were also carried out by others (*74*, *75*).

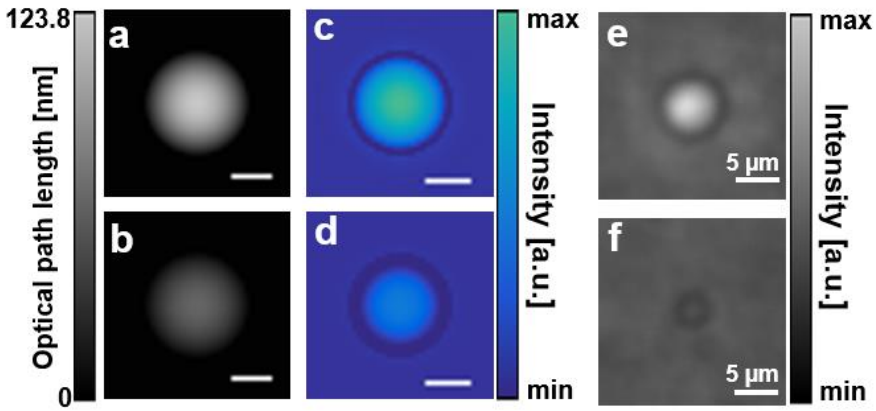

Fig. 4-9. Examination of micro lens with different thicknesses and comparison between simulation and experimental results. (a-b), The optical path length of two micro lenses under simulation. (c-d), Phase contrast images generated by simulation using a positive phase plate. (e-f), Experimental results of two TAG droplets from the condenser-free Zernike phase contrast microscope (*77*). Scale bar of (a-d): 10 µm.

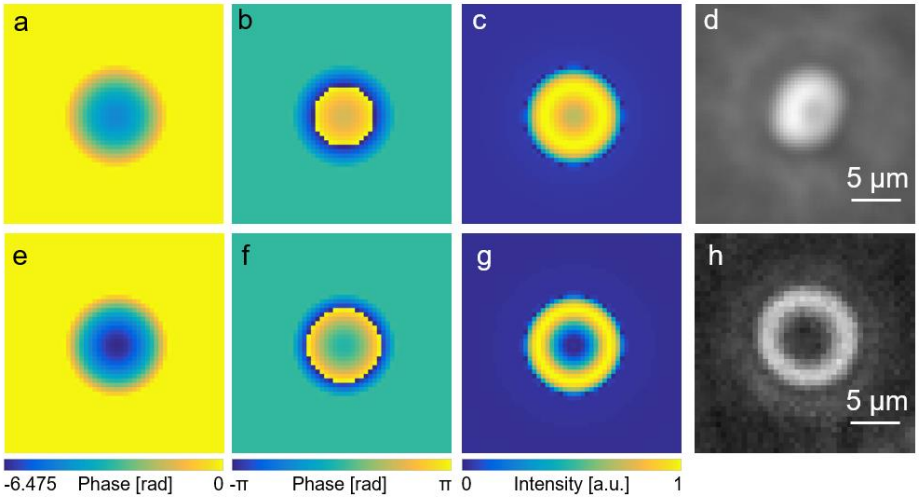

Fig. 4-10. Examination of the thick sample with phase wrapping, and the comparison between simulation and experimental results. (a-c) Simulation results of a micro lens with curvature of 6.67×10^{-4} µm^{-1}. (a) Phase retardation map. (b) The wrapped phase by setting the phase of the background as reference point 0 rad. (c) Simulation phase contrast image (positive phase contrast). (d) CF-ZPC experimental image of a TAG drop that is comparable with the simulation (d). (e-g) Simulation results of a micro lens with the curvature of 9.1×10^{-4} µm^{-1}. (e) Phase retardation map. (f) The wrapped phase by setting the phase of the background as reference point 0 rad. (g) Simulation phase contrast image (positive phase contrast). (h) CF-ZPC experimental image of a TAG drop that is comparable with the simulation.

To validate the CF-ZPC, we carried out a comparison between the simulation and experiment. In the simulation, the thickness of the micro lens can be changed by reducing the curvature of micro lens in **Fig. 4-5**b. The optical path length of two micro lenses with curvatures of 0.002 µm^{-1} and 0.001 µm^{-1} are shown in **Fig. 4-9**(a,b). For their corresponding phase contrast images (**Fig. 4-9**c,d), we observed that the

thick micro lens has higher intensity in the center and smaller dark ring. The dark ring can also be observed in the experimental results as shown in **Fig. 4-9**(e,f), which are obtained by imaging the TAG drops of different sizes from CF-ZPC. As the thickness of the micro lens increased, we observed the intensity wrapping from both simulation and experimental results (as shown in **Fig. 4-10**c,d and **Fig. 4-10**g,h), which can be expected from the plot of **Fig. 4-3**a.

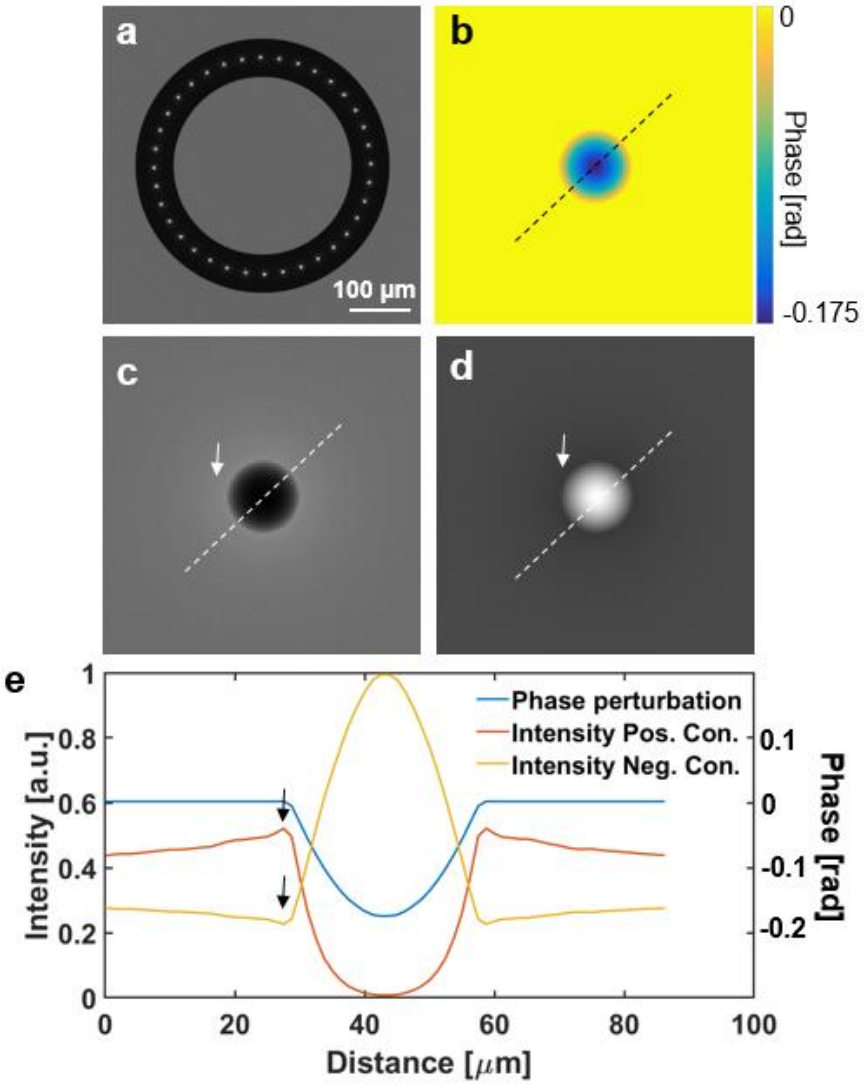

Fig. 4-11. ZPC imaging of the thin sample. a, The intensity image of the back focal plane during simulation. **b,** The phase map of the micro lens, with maximum phase retardation of 0.175 rad. **c,** Positive phase contrast image. **d,** Negative phase contrast image. **e,** Line profiles from the phase perturbation image (b), phase contrast images (c) and (d).

To simulate the thin sample, we adjust the thickness of the micro lens so that the optical path length difference of the micro lens is similar to the optical path length of the cells. **Fig. 4-11**b shows the phase perturbation map of the micro lens in thin sample condition. **Fig. 4-11**c,d depicts the positive and negative phase contrast images of this micro lens. **Fig. 4-11**e shows the line profiles crossing (b), (c) and (d). As we can observe in (c) and (d), the positive phase contrast gives dark contrast for the thin sample, while

the negative phase contrast image gives bright contrast. This observation consist with most of the cells measurement by ZPC microscopy. We also observe a bright “Halo” in the positive contrast micrograph, and the dark “Halo” in the negative phase micrograph (marked by the arrows in (c), (d), and (e)). This “Halo” artifact is clearer when using a larger phase ring (in this case, more deviated light travel through the phase ring).

The "Halo" artifact arises from the fact that a portion of deviated waves, experiences weak deviation as they pass through the sample. As the result of weak deviation, this portion of light mistakenly falls into the phase ring and keeps the $\pi/2$ phase shift relative to the surrounding wave. Since the relative phase between this portion of deviated light and surrounding light has not been changed, constructive or destructive interference cannot be produced in the imaging plane. The absence of interference creates a localized reversal contrast – a “Halo” surrounding the image of the object. The “Halo” artifact is bright in a positive phase image, and dark in a negative phase contrast image.

4.2 Phase-shifting microscopy (PSM)

The interference of the CF-ZPC microscopy is given by two components of illumination: deviated component and surrounding component, as shown in **Fig. 4-2**. The deviated component and surrounding component begin to deviate from each other after passing through the sample plane (due to the diffraction of the sample), and become well-separated on the back focal plane (BFP) of the objective. Here, in the BFP, the surrounding component is focused into a spot (or a ring, depending on the shape of illumination) and the deviated component distributes over the whole BFP. The two components are later overlapped to create an interferogram on the sensor plane – a microscopic image. Taking advantage of the separation on BFP, the surrounding component can be altered (on BFP) to maximize the constructed or destructed interference in the sensor plane. In CF-ZPC, the two interference components travel through the common optics (objective, or tube lens), forming the common path microscopy that is very robust against environmental vibration. However, since the CF-ZPC relies on the scattering property of sample, an un-scattering sample (for instance, a flat cell) usually illustrates weak image contrast. This is because one of the interference components from the sample – deviated component – is weak. Moreover, CF-ZPC does not provide an exact phase value according to the image it obtains. And its sensitivity to the optical path change is weak especially for the positive phase contrast phase microscope, since the phase-intensity conversion relation begins from a valley, where the slope is small (**Fig. 4-3**).

To overcome the above challenges, I proposed a new design for phase imaging as a follow-up work of using CF-ZPC as probe. In this design, the illumination light is divided into two components (sample beam and reference beam) before traveling through the sample plane of the microscope. Therefore, the interference does not rely on the scattering of the sample, and a quantitative phase-intensity relation can

be constructed. To maintain the advantage of the common path, we used a polarization phase-shifting interferometer (PSI), in which both the sample beam and reference beam travel through the same optics.

4.2.1 Polarization phase-shifting interferometer

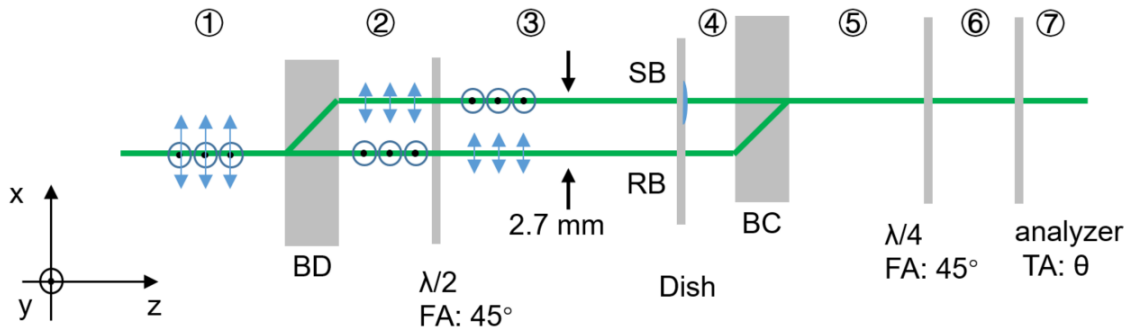

Fig. 4-12. Diagram of polarization phase-shifting interferometer. The polarization phase-shifting interferometer uses a monochromatic coherent light (532 nm) as input. The input light is 45° linear polarized light (Hereinafter refer to polarization angle as the polarized direction relative to x-axis). A birefringent crystal (beam displacer, BD) divides the beam into two paths with orthogonal polarization directions: the sample beam (SB) with x-axis polarization, and the reference beam (RB) with y-axis polarization. Afterward, the two beams travel through a haft wave plate with fast axis of 45°, which rotates the polarization of both beams by 90°. Then the sample beam travels through the sample so that a phase difference between the sample beam and the reference beam is introduced. Then the two beams travel through a birefringent beam combiner (BC) to be combined. Finally the combined beam travel through a quarter wave plate and an analyzer. FA: Fast Axis; TA: Transmission Axis.

As shown above in the polarization phase-shifting interferometer, a 45° linear polarization beam is separated into two orthogonally polarized beams by a birefringent beam displacer (BD). The ordinary beam (Reference Beam, RB) travels straight through the BD, resulting in a beam linearly polarized at 90° relative to the x-axis. While the extraordinary beam (Sample Beam, SB) exits the BD crystal in parallel with the RB but is 2.7 mm separated. SB is linearly polarized at 0° relative to x axis. The two beams then travel through a half-wave plate (fast axis: 45°), for the purpose of compensating the static optical path difference between the two beams. The polarization angles of the two beams are both 90° rotated after passing the half-wave plate. The two beams then travel through the sample plane and a beam combiner (which is an identical birefringent crystal as BD). Due to the 90° rotation of both beams, the beam combiner combines the beams in a symmetric way as they were divided, to compensate for static optical path length difference in the dividing path. Therefore, the optical path difference (i.e., phase retardation) is introduced only by the sample on the sample plane. The combined beam then travels through a quarter wave plate (with its fast axis: 45°) and an analyzer (a polarizer with a rotation motor), for the purpose of converting the OPD to intensity variation. Here we denote the transmission

axis angle of the polarizer as θ, which can be adjusted by controlling the rotation motor. By using the Jones vector (*79, 80*), here we derive the relation between the phase retardation introduced by the sample and the intensity of the interferogram.

4.2.2 Jones calculus interpretation

Using complex representation, the electric field of a linear polarized light can be expressed (Customarily, the equal sign here takes only the real part of the complex representation):

$$\overrightarrow{\boldsymbol{E_x}}(z,t) = \hat{\boldsymbol{x}} E_{x0} e^{i(kz-\omega t)} \qquad \textit{eq. 4-11}$$

Where $\hat{x}$ is a unit vector perpendicular to the propagation direction; E_{x0} is amplitude; k is wavenumber; z is propagation distance; ω is the angular frequency. According to eq. 4-11, the electric field of a linear polarized light always points along a defined direction (defined by a unit vector) with its magnitude or sign changing over time.

Imaging there is another collinear electromagnetic field (with angular frequency ω) traveling toward the same direction as the wave described by eq. 4-11, but vibrating in another direction perpendicular to both the x-axis and propagation direction, denoted as the y-axis:

$$\overrightarrow{\boldsymbol{E_y}}(z,t) = \hat{\boldsymbol{y}} E_{y0} e^{i(kz-\omega t+\epsilon)} \qquad \textit{eq. 4-12}$$

Where ϵ is a phase difference between the two waves. The resultant of the electric fields of eq. 4-11 and eq. 4-12 can be expressed as a two-dimensional vector:

$$\vec{\boldsymbol{E}}(z,t) = \overrightarrow{\boldsymbol{E_x}}(z,t) + \overrightarrow{\boldsymbol{E_y}}(z,t)$$

$$= \begin{pmatrix} E_{x0} e^{i(kz-\omega t)} \\ E_{y0} e^{i(kz-\omega t+\epsilon)} \end{pmatrix} \qquad \textit{eq. 4-13}$$

$$= \begin{pmatrix} E_{x0} \\ E_{y0} e^{i\epsilon} \end{pmatrix} e^{i(kz-\omega t)}$$

The Jones vector of the resultant wave is defined as the two-dimensional vector representing the amplitude and phase in the x and y directions:

$$\begin{pmatrix} E_{x0} \\ E_{y0} e^{i\epsilon} \end{pmatrix} \qquad \textit{eq. 4-14}$$

The Jones vector can be used to express the electric field of an elliptical polarization light, in which the special case is circular polarization light (when $\epsilon = \frac{\pi}{2} + 2\pi n$, where $n = \cdots, -2, -1, 0, 1, 2, \ldots$). Contrary to linear polarized light, where the electric field vibrating along a defined direction, the electric field direction of an elliptical polarization light rotates in the x-y plane when the light propagates forward.

A polarizer or phase retarder acting on the light is a projection from a two-dimensional Jones vector to a new two-dimensional Jones vector, so the effect of these optical elements on the light can be represented by multiplication of a 2×2 matrix (Jones matrix) to the Jones vector.

Table 4-1. Jones matrix of typical optical elements

Optical element	**Jones matrix**
Linear polarizer (TA: 45°)	$\begin{pmatrix} 1/2 & -1/2 \\ -1/2 & 1/2 \end{pmatrix}$
Linear polarizer (TA: θ °)	$\begin{pmatrix} cos^2(\theta) & cos(\theta)sin(\theta) \\ cos(\theta)sin(\theta) & sin^2(\theta) \end{pmatrix}$
Quarter-wave plate (FA: 45°)	$\frac{1}{2}e^{-i\frac{\pi}{4}}\begin{pmatrix} 1+i & 1-i \\ 1-i & 1+i \end{pmatrix}$
Quarter-wave plate (FA: θ °)	$e^{-i\frac{\pi}{4}}\begin{pmatrix} cos^2\theta + isin^2\theta & (1-i)sin\theta cos\theta \\ (1-i)sin\theta cos\theta & sin^2\theta + icos^2\theta \end{pmatrix}$
Half-wave plate (FA: 45°)	$e^{-i\frac{\pi}{2}}\begin{pmatrix} 0 & 1 \\ 1 & 0 \end{pmatrix}$
Half-wave plate (FA: θ °)	$e^{-i\frac{\pi}{2}}\begin{pmatrix} cos^2\theta - sin^2\theta & 2sin\theta cos\theta \\ 2sin\theta cos\theta & sin^2\theta - cos^2\theta \end{pmatrix}$

TA: Transmission Axis; FA: Fast Axis. The angle takes x-axis as reference.

In **Fig. 4-12**, assuming the electric field amplitude of input beam I_0 as unit 1, we present the input beam (location ①) as a Jones vector of:

$$\frac{1}{\sqrt{2}}\begin{pmatrix} 1 \\ 1 \end{pmatrix} \qquad \textit{eq. 4-15}$$

From ① to ②, the input beam is separated into two orthogonally polarized beams: 0° polarization (SB) and 90° polarization (RB), respectively. We consider this process as traveling through two orthogonal polarizers respectively: polarizer with a transmission axis of 0° and polarizer with a transmission axis of 90°. According to Table 4-1, these two polarizers can be expressed using the Jones matrix of $\begin{pmatrix}1 & 0\\0 & 0\end{pmatrix}$ and $\begin{pmatrix}0 & 0\\0 & 1\end{pmatrix}$. The beams in location ② can be expressed as the production of the Jones matrix of polarizers and Jones vector of input beam:

Reference beam,

$$\begin{pmatrix}0 & 0\\0 & 1\end{pmatrix}\cdot\frac{1}{\sqrt{2}}\begin{pmatrix}1\\1\end{pmatrix}=\frac{1}{\sqrt{2}}\begin{pmatrix}0\\1\end{pmatrix} \qquad \textit{eq. 4-16}$$

Sample beam,

$$\begin{pmatrix}1 & 0\\0 & 0\end{pmatrix}\cdot\frac{1}{\sqrt{2}}\begin{pmatrix}1\\1\end{pmatrix}=\frac{1}{\sqrt{2}}\begin{pmatrix}1\\0\end{pmatrix} \qquad \textit{eq. 4-17}$$

Since the Jones matrix of half-wave plate at 45° is $e^{-i\frac{\pi}{2}}\begin{pmatrix}0 & 1\\1 & 0\end{pmatrix}$, after the two beams travel through the half-wave plate, the beams in location ③ can be expressed as:

Reference beam:

$$e^{-i\frac{\pi}{2}}\begin{pmatrix}0 & 1\\1 & 0\end{pmatrix}\cdot\frac{1}{\sqrt{2}}\begin{pmatrix}0\\1\end{pmatrix}=\frac{1}{\sqrt{2}}e^{-i\frac{\pi}{2}}\begin{pmatrix}1\\0\end{pmatrix} \qquad \textit{eq. 4-18}$$

Sample beam,

$$e^{-i\frac{\pi}{2}}\begin{pmatrix}0 & 1\\1 & 0\end{pmatrix}\cdot\frac{1}{\sqrt{2}}\begin{pmatrix}1\\0\end{pmatrix}=\frac{1}{\sqrt{2}}e^{-i\frac{\pi}{2}}\begin{pmatrix}0\\1\end{pmatrix} \qquad \textit{eq. 4-19}$$

After the sample, in location ④, we assume that a phase difference δ is introduced to the sample beam:

We have the sample beam multiplied by $e^{i\delta}$,

$$\frac{1}{\sqrt{2}}e^{-i\frac{\pi}{2}}\,e^{i\delta}\,\begin{pmatrix}0\\1\end{pmatrix} \qquad \textit{eq. 4-20}$$

Reference beam keeps the same notation as before sample plane,

$$\frac{1}{\sqrt{2}}e^{-i\frac{\pi}{2}}\begin{pmatrix}1\\0\end{pmatrix} \qquad \textit{eq. 4-21}$$

In location ⑤, the two beams are combined:

$$\frac{1}{\sqrt{2}}e^{-i\frac{\pi}{2}}e^{i\delta}\begin{pmatrix}0\\1\end{pmatrix}+\frac{1}{\sqrt{2}}e^{-i\frac{\pi}{2}}\begin{pmatrix}1\\0\end{pmatrix}=\frac{1}{\sqrt{2}}e^{-i\frac{\pi}{2}}\begin{pmatrix}1\\e^{i\delta}\end{pmatrix} \qquad \textit{eq. 4-22}$$

In location ⑥, since the Jones matrix for the 45° quarter wave plate (QWP) is: $\frac{1}{2}e^{-i\frac{\pi}{4}}\begin{pmatrix}1+i & 1-i\\1-i & 1+i\end{pmatrix}$, the combined beam become:

$$\frac{1}{2}e^{-i\frac{\pi}{4}}\begin{pmatrix}1+i & 1-i\\1-i & 1+i\end{pmatrix}\cdot\frac{1}{\sqrt{2}}e^{-i\frac{\pi}{2}}\begin{pmatrix}1\\e^{i\delta}\end{pmatrix} \qquad \textit{eq. 4-23}$$

$$=\frac{1}{2\sqrt{2}}e^{-i\frac{\pi}{4}}e^{-i\frac{\pi}{2}}\begin{pmatrix}1+i+(1-i)e^{i\delta}\\1-i+(1+i)e^{i\delta}\end{pmatrix}$$

In location ⑦, the Jones matrix for the linear polarizer with the transmission axis angle θ can be expressed as:

$$\begin{pmatrix}cos^2\theta & sin\theta cos\theta\\sin\theta cos\theta & sin^2\theta\end{pmatrix} \qquad \textit{eq. 4-24}$$

By ignoring all the light attenuation due to the optical elements, the electric field at output beam can be expressed as:

$$E=\begin{pmatrix}cos^2\theta & sin\theta cos\theta\\sin\theta cos\theta & sin^2\theta\end{pmatrix}\cdot\frac{1}{2\sqrt{2}}e^{-i\frac{\pi}{4}}e^{-i\frac{\pi}{2}}\begin{pmatrix}1+i+(1-i)e^{i\delta}\\1-i+(1+i)e^{i\delta}\end{pmatrix} \qquad \textit{eq. 4-25}$$

The intensity is:

$$I\propto|E|^2=\frac{1}{2}\big(1+sin(2\theta+\delta)\big) \qquad \textit{eq. 4-26}$$

Where θ is the polarization angle, and δ is the phase difference introduced by the sample. eq. 4-26 states the relation between the phase retardation introduced by the sample, and the intensity of the interferogram.

4.2.3 Light polarization states in PSI

In this section, we discuss the polarization states of the beam as it travels through PSI, and understand how the phase-shifting mechanism can be carried out by PSI. According to whether there is phase perturbation on the sample beam, two situations (unperturbed case and perturbed case) will be discussed.

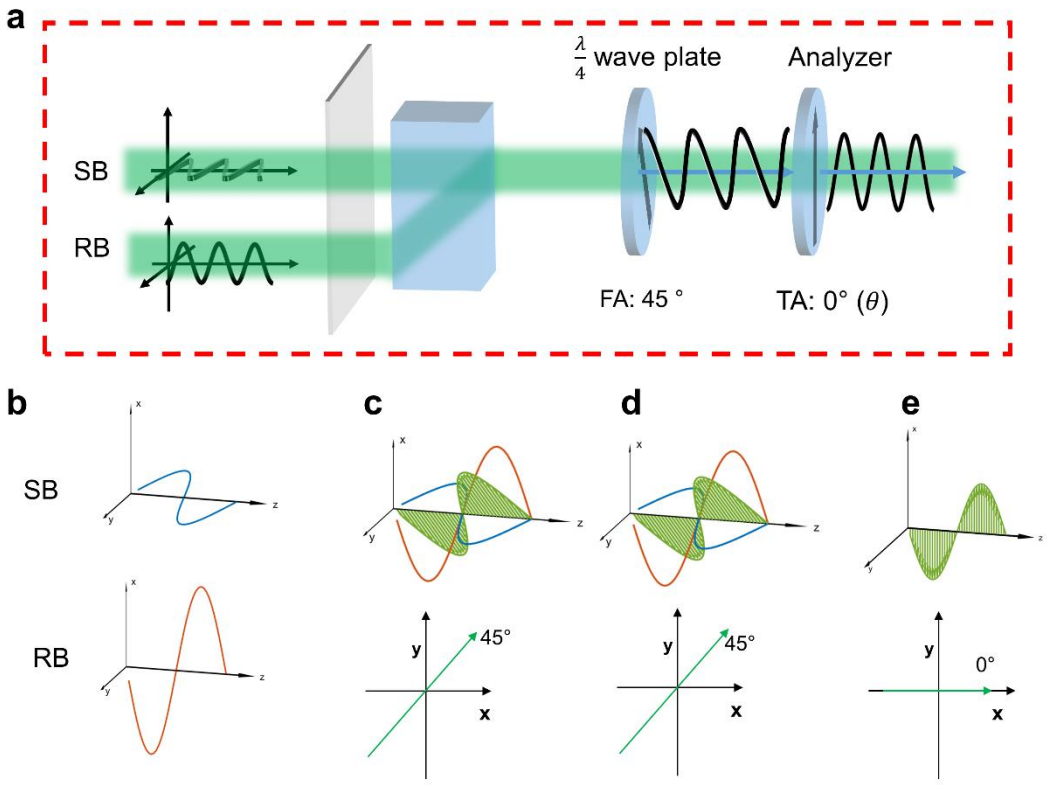

Fig. 4-13. Light polarization states in unperturbed case. **a,** 3D view of PSI with illustrations of electric waves. **b,** Illustrations of electric waves of SB and RB before beam combiner. SB: 90° polarized (on the y-axis); RB: 0° polarized (on the x-axis). **c,** Electric wave illustration of the combined beam after beam combiner. Polarization: 45°. **d,** Electric wave illustration of the beam after quarter-wave plate. Polarization: 45°. **e,** Electric wave illustration of the beam after analyzer. Polarization: 0°.

When both beams, SB and RB, travel the same optical path length (i.e., no optical perturbation on the sample plane) the combined probe beam out of the beam combiner is a 45° linearly polarized beam (**Fig. 4-13**c). This is because the vibration azimuth of the electric fields of both components are in phase. The combined beam then passes through a quarter-wave plate (fast axis: 45°; slow axis: 135°). Here, the polarization of the beam is not affected by the quarter-wave plate, since the beam does not have component in the direction of the slow axis of the quarter-wave plate (i.e., polarization of the beam is orthogonal to slow axis of quarter-wave plate). Therefore, the probe beam after the quarter-wave plate is still a 45° linearly polarized beam (**Fig. 4-13**d). If a single-point photodetector is placed just after the

quarter-wave plate, it would detect the same light intensity as the input beam, since the beam is identical to the input. However, if a polarizer (termed analyzer) with a transmission angle of 0° is placed just after the quarter-wave plate, before the single-point detector, the single-point detector will detect the x-axis polarization component of the light (**Fig. 4-13**e), the detected intensity following the Malus's law (which states that the intensity of linear polarization light that passes through an analyzer varies as the angle between the light's polarization plane and the transmission axes of the analyzer).

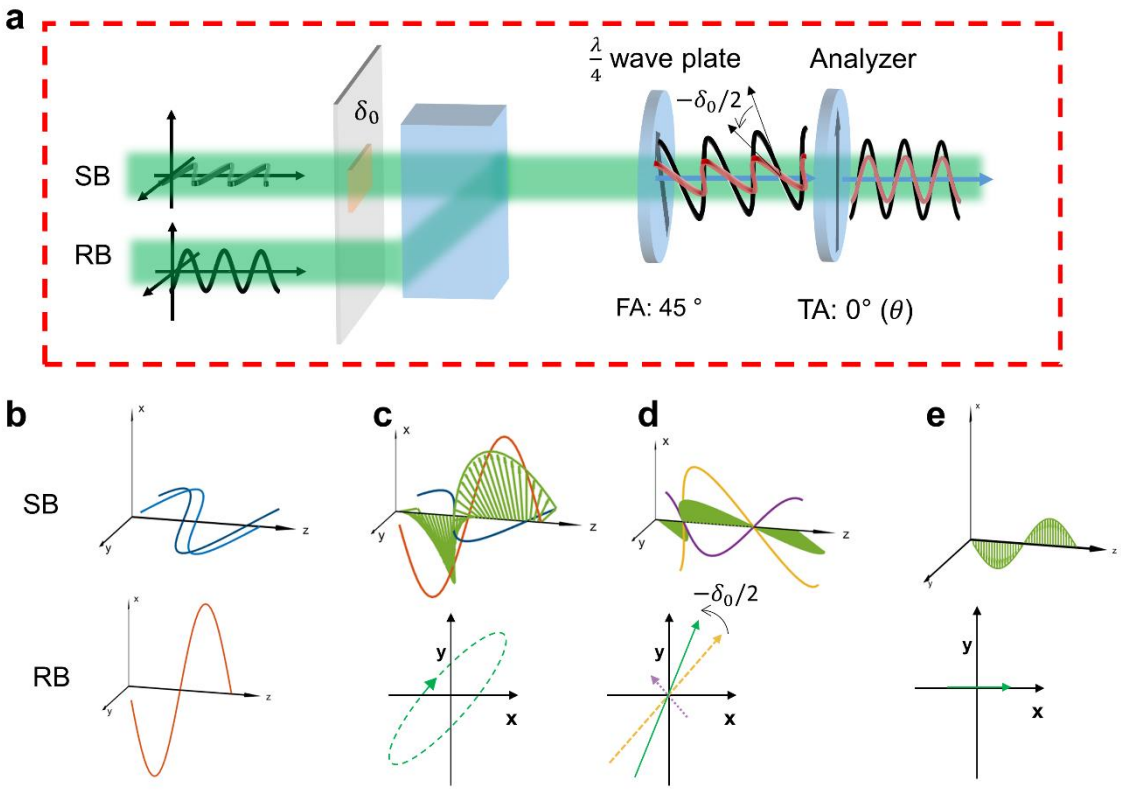

Fig. 4-14. Light polarization states in perturbed case. **a,** 3D view of PSI with illustrations of electric waves. A phase perturbation δ_0 is introduced to the SB from the sample plane. The black waves after $\lambda/4$ plate and analyzer illustrate polarizations of the probe beam in unperturbed case that have been discussed in **Fig. 4-13**. The orange wave illustrates the polarization of the beam in perturbed case. **b,** Electric wave illustration of SB and RB before beam combiner. The phase of SB is retarded by δ_0, which is a negative value denoting the phase retardation and positive value denoting the phase advance. SB: 90° polarized; RB: 0° polarized. **c,** Electric wave illustration of the combined beam after beam combiner in perturbed case. Polarization: elliptically polarized. **d,** Electric wave illustration of the beam after quarter-wave plate. Yellow and purple illustrate the two decomposition components along fast axis and flow axis of quarter-wave plate. Polarization: linear polarized at $45° - \delta_0/2$. **e,** Electric wave illustration of the beam after analyzer. Polarization: 0°.

On the other hand, when a phase retardation δ_0 is introduced to the SB (**Fig. 4-14**b), the resulting combined beam after the beam combiner is elliptically polarized (**Fig. 4-14**c). This is because after the

beam combiner, the vibration azimuth of the electric fields of both components are out of phase (**Fig. 4-14**b), and the direction of resultant of electric vector deviates away form 45° and the resultant draws an ellipse in the x-y plane (as shown in **Fig. 4-14**c). The larger the phase retardation δ_0 on the SB, the smaller is the eccentricity of the polarization ellipse, until the SB phase retardation is 90°; in which case, a circularly polarized probe beam (eccentricity = 0) is generated. The direction of major/minor axis of the polarization ellipse will be always 45° regardless of the phase retard value δ_0. When the elliptical polarized beam enters the quarter-wave plate (which, as mentioned, has its slow axis at 135°), it is converted to linear polarization beam because the slow axis of the quarter-wave plate is orthogonal to major axis of the polarization ellipse. The linearly polarized beam—after the quarter-wave plate—has a polarization angle of $45° - \delta_0/2$ (green arrow in **Fig. 4-14**d). This beam has been rotated by $-\delta_0/2$ relative to the no optical perturbed case (45°). Again, if a single-point photodetector is placed just after the quarter-wave plate, it would detect the same light intensity as input beam. However, if a analyzer with transmission angle of 0° is placed just after the quarter-wave plate, before the single-point detector, the single-point detector will detect an intensity change (compared with unperturbed case) due to the angle rotation $\delta_0/2$, according to the Malus's law (as shown in **Fig. 4-14**e).

Following the Malus's law, the same phase intensity relation as eq. 4-26, can be deduced:

$$I = \frac{1}{2}\left(1 + sin(2\theta + \delta_0)\right) \qquad \textit{eq. 4-27}$$

Here I is the intensity of the output light can be measured by the single-point detector, δ_0 is phase retard on SB, and θ is angle of analyzer. According to eq. 4-27, the intensity does not only dependent on the unknown phase perturbation δ_0 (which we want to measure), it also dependent on a known and controllable "phase-shift" — 2θ (termed global phase), which can be read/set from the analyzer of the system. Therefore, a phase-shifting mechanism is achieved, in which a controllable phase shift is added

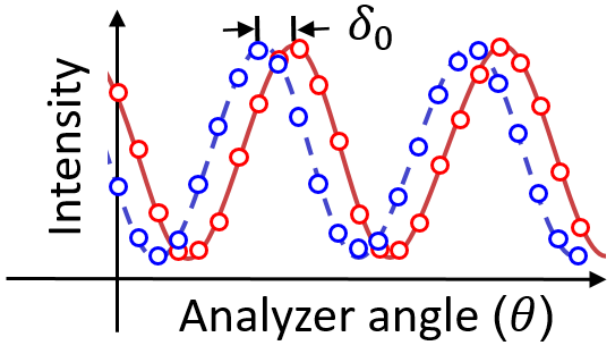

Fig. 4-15. The phase-intensity fitting curves. By rotating the analyzer, the phase-intensity relation is shifting along the θ-axis.

upon a phase perturbation of interested (*81*, *82*). Benefiting from the phase-shifting mechanism, the phase perturbation can be measured with high accuracy using the data acquired during a controlled phase shifting. For instance, to quantitatively obtain the phase perturbation δ_0, one can acquire multiple data points (at least 4 points) at different analyzer angles (i.e., shifting the global phase), and fit the data points to **eq. 4-27**. The phase perturbation δ_0 can be obtained from the shift of fitting curves as shown in **Fig. 4-15**.

4.2.4 Construction of phase-shifting microscopy

A phase-shifting interferometer with a single point detector only provides a single intensity value *I* according to the global phase retard on sample plane, lacking the capability of detecting localized phase retard in the sample plane (e.g. obtaining a phase image). For the purpose of detecting localized phase retard, an objective, a tube lens, and a camera are incorporated into PSI to construct a Phase-Shifting Microscopy (PSM, **Fig. 4-16**). Where in PSM, the objective and tube lens form a 4-f system, projecting the sample plane to the camera sensor.

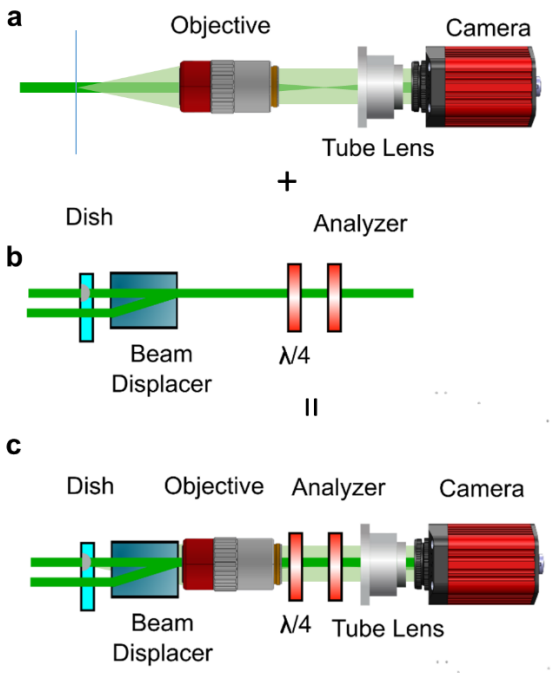

Fig. 4-16. Construction of Phase-Shifting Microscopy (PSM). **a,** An infinite microscopic system, constructed by an objective, a tube lens, and a camera. **b,** Phase-shifting interferometer. **c,** Integration of microscope with phase-shifting interferometer.

In **Fig. 4-16**, an infinite microscopic system is integrated into PSI. In the infinite microscopic system, the objective is supposed to project the sample plane to infinite distance, and a tube lens is used for converging the light to form an image on the camera sensor. Therefore, a parallel light space exist

between the objective and tube lens. PSM takes the advantage of this parallel light space for inserting the quarter-wave plate and analyzer to minimize the optical aberration.

As discussed in section **4.2.3,** a controllable phase-shifting process is needed for achieving high accuracy phase measuring. This can be achieved, for example, continuously rotating the analyzer using a rotation stage (termed free polarizer implementation, as shown in **Fig. 4-17**a). To circumvent the mechanical rotation, one can also apply a camera with polarizer grid integrated on the sensor (termed integrated polarizer implementation, as shown in **Fig. 4-17**b) to simultaneously capture multiple phase-shifting images. **Fig. 4-17**b shows an example of integrated polarizer implementation that the camera sensor is integrated with polarizer grid of 315° (or -45°), 0°, 45°, 90° micro-polarizers.

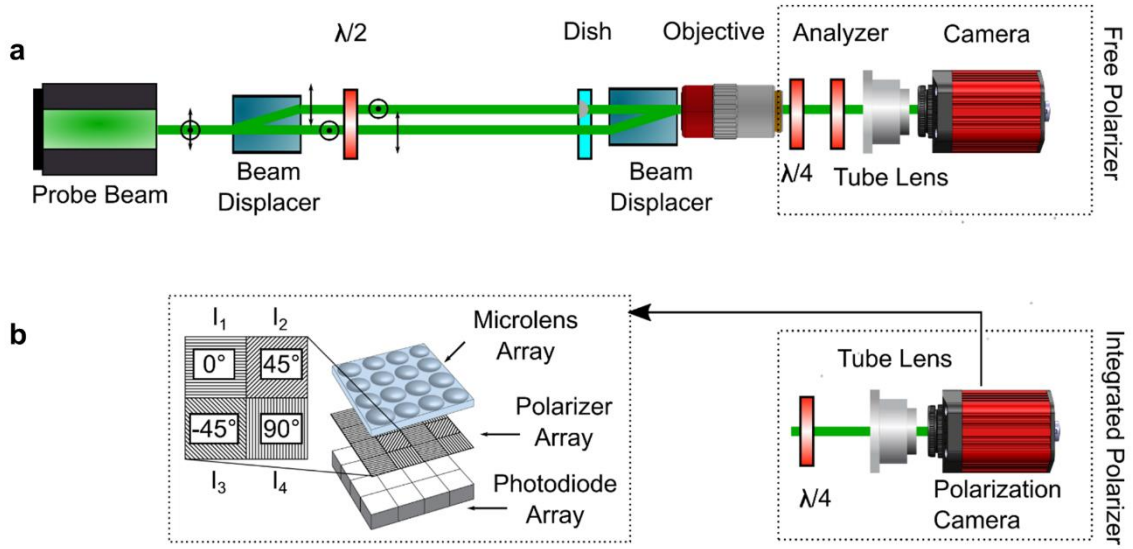

Fig. 4-17. Two implementations of PSM. **a,** Free polarizer implementation. **b,** Integrated polarizer implementation.

With a camera as our detector, PSM is able to collect an intensity image $I_{(x,y)}$ based on the localized phase retard $\phi_{0(x,y)}$ in the image plane, where (x, y) indicates the coordination. The relation of intensity image $I_{(x,y)}$ and phase retard $\phi_{0(x,y)}$ follows:

$$I_{(x,y)} = \frac{I_0}{2}\left(1 + sin\left(2\theta + \phi_{0(x,y)}\right)\right) \qquad eq.\ 4\text{-}28$$

When using PSM for measuring the living cells, the local phase change of $\phi_{0(x,y)}$ is mainly contributed from the cells' refractive index or the cells' thickness. We call this type of phase as "intrinsic-phase" in this thesis to distinguish it between the phase perturbations generated by the MIR illumination.

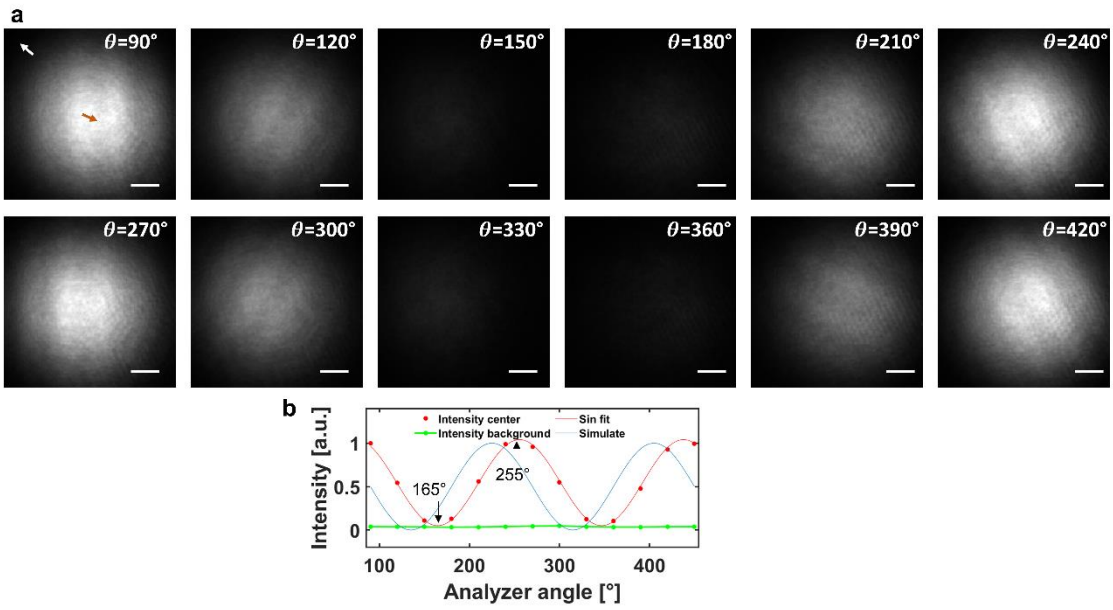

Fig. 4-18. Intensity images of the beam profile. a, PSM images of the beam profile (i.e., the whole FOV without any sample) when analyzer angle θ varying from 90° to 420° with step of 30°. Scale bar: 1000 μm. **b**, Sine fit of the data points obtained from the beam profile (as indicated by arrows in first image of Fig. a), and comparison with plot (labeled by "simulation") of eq. 4-28, by letting $\phi_{0(x,y)} = 0$, and $I_0 = 1$.

To experimentally validate sine function of eq. 4-28, we first capture the probe beam profile by changing the analyzer angle, as shown in **Fig. 4-18**a. This beam profile is captured when there is no sample on the FOV. **Fig. 4-18**b plots the intensity of a pixel obtained from the center of the FOV, together with its sine fit curve (red). For comparison, the intensity of a point from background (green), as well as eq. 4-28 are also plotted. It is observed that when the analyzer angle is around 165°, the light intensity of the FOV drop down to minimum of 0, and when the analyzer angle is around 255°, the intensity reach to maximum 1 (normalized value). Since the analyzer is a linear polarizer, this observation suggests that the light before entering the analyzer is a linear polarized light in angle of 255° (or 75°), indicating a phase retard of -60° (calculated from equation: $45° - \frac{\delta_0}{2} = 75°$) existing on SB paths. This static phase perturbation is system related, probably caused by the unperfected alignment of the system or unperfected optics due to manufacture.

PSM's capability of imaging phase objects can be validated by measuring a thin (~30 nm) and transparent phase target. **Fig. 4-19**a,b show two intensity images of a phase target with thin Indium-Tin-Oxide (ITO) structures, captured at analyzer angle of 150°. Due to the phase retardation in the ITO region (marked by "ITO" in **Fig. 4-19**a and **Fig. 4-19**b), the PSM renders its intensity darker than the background, where ITO is absent (marked by "BG"). Therefore, PSM provides higher image contrast compared with ZPC microscope (**Fig. 4-19**c and **Fig. 4-19**d), where the ITO structures have similar intensity compared to the background.

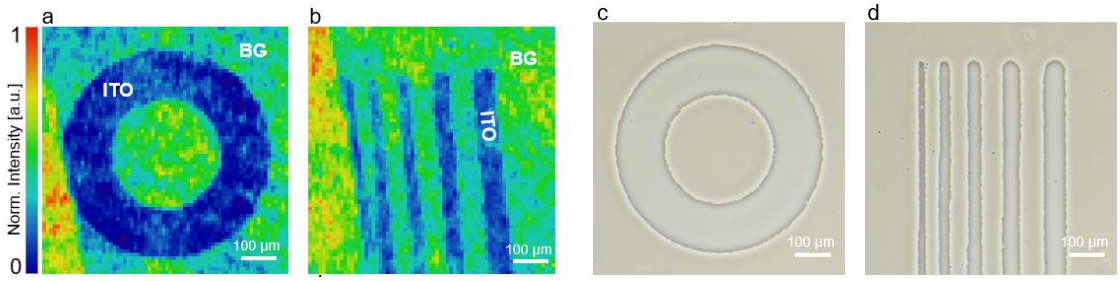

Fig. 4-19. Intensity images of Indium-Tin-Oxide (ITO) structure (analyzer angle: 150°). a, Intensity image of an ITO ring. **b,** Intensity image of 5 ITO stripes. (a,b) Acquired captured under a 1× objective and 11 µm pixel size camera. **c,d**, Corresponding image of (a,b) under a Zernike phase contrast microscope. The phase retard in the ITO region shows lower intensity compared to background (BG).

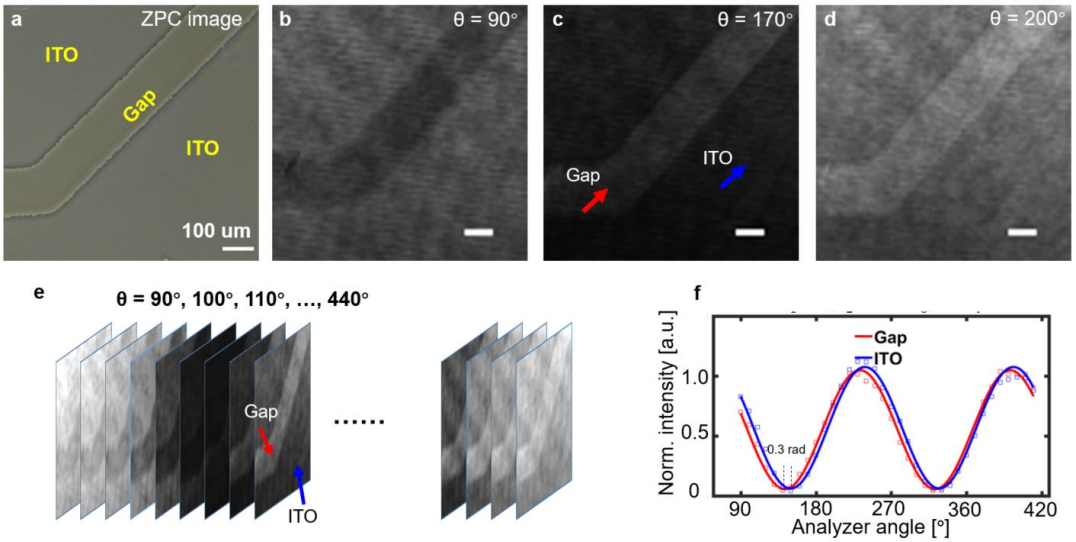

Fig. 4-20. Intensity images of ITO acquired by varying analyzer angle of PSM. a, ZPC image of the ITO structure. It is ITO layer with a gap (without ITO layer). **b-d,** PSM intensity images for analyzer angles of 90°, 170°, and 200°. **e,** Intensity images tack for analyzer angles from 90° to 440°, with step of 10°. **f,** Plot of pixel intensity varying with analyzer angle extracted from two points as indicated in (e), i.e., from ITO and gap respectively.

Measurement of the ITO phase target can be used to validate the phase-intensity relation given by eq. 4-28. In **Fig. 4-20**, we acquired intensity images of ITO by varying angle of analyzer from 90° to 200°, with step of 10°. The sample is two ITO layers separated by a gap as shown in **Fig. 4-20**a. Because of the phase difference between the gap region and ITO region, their corresponding intensity are different, as illustrated in **Fig. 4-20**b-d, where the ITO region is brighter than the gap region. By rotating the analyzer, one can obtain the image stack (**Fig. 4-20**e) where both intensity of ITO and gap are varying according to sinusoidal relation as given in eq. 4-28. As discussed before, one can fit the intensity of pixels to a sinusoidal function, to study the phase retardation. For instance, **Fig. 4-20**f plot intensity of two pixels from gap and ITO respectively (marked in **Fig. 4-20**c,e), the phase difference between these

two sinusoidal curves indicates the optical path difference of the light that travel through the gap and the ITO, which is c.a. 0.3 rad.

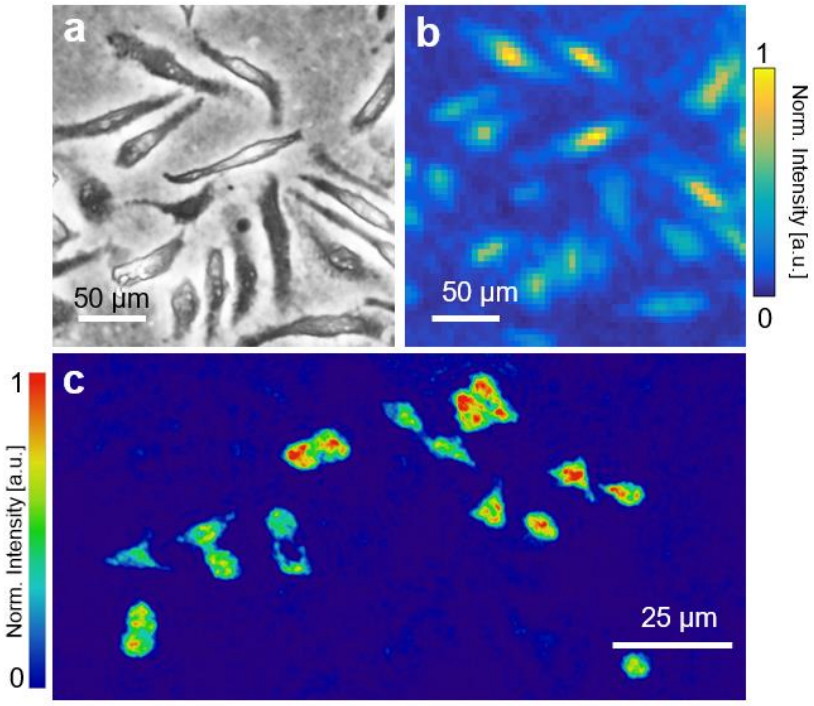

Fig. 4-21. Intensity images of HeLa cells and LS147T Cells imaging under PSM. **a,** Zernike phase contrast image of HeLa cells. **b,** PSM image of the same FOV as Fig. (a). (b) Captured by a 1× objective and 11 µm pixel size camera. **c**, PSM image of LS147T cells. (c) Captured by a 10× objective and 4.5 µm pixel size camera.

4.2.5 Quantitative phase reconstruction

In previous section, we already got some intensity images from a phase target using PSM. But the intensity image provided by PSM is not linearly related to the phase of the sample. Instead, it is a sinusoidal relation follows eq. 4-27**.** One straight forward method for acquiring a quantitative phase image (QPI) is to acquire the whole image stack from a range of analyzer angles (as shown in **Fig. 4-20**), and fit the sine curve for each location of the image. The quantitative phase value can be obtained the sine curves of every single pixels.

To demonstrate this idea of quantitative phase imaging, we reconstruct a quantitative phase image using the image stack acquired at **Fig. 4-20**. Here, we fit the z-profile of the imaging stack to a sine function: $P_1 sin(P_2 * \theta - P_3) + P_4$. With this method, each pixel on the FOV generates 4 parameters, corresponding to 4 parameters of the fit function. Collecting values from all pixels of the FOV, these 4 parameters construct 4 images, as illustrated in **Fig. 4-22**a-d. The parameter P1 is amplitude of the sine function, corresponding to the localized light intensity of the illumination. Parameter P2 is the factor in from of the analyzer angle, which is supposed to be 2 according to the eq. 4-27. Parameter P3 is the phase retard

caused by the sample, showing the localized phase retardation in the FOV. Therefore, acquiring image of P3 can be our aim: a quantitative phase image. Parameter P4 is the baseline intensity related to the dark noise of the camera. The similar measurement was also performed on a ring shape structure of the ITO target (**Fig. 4-23**). One can observe that the optical phase retardation of the light that travels through the ITO ring is around 0.366 rad (**Fig. 4-23**o), corresponding to ITO thickness of around 35.2 nm (considering the refractive index of ITO as 1.88).

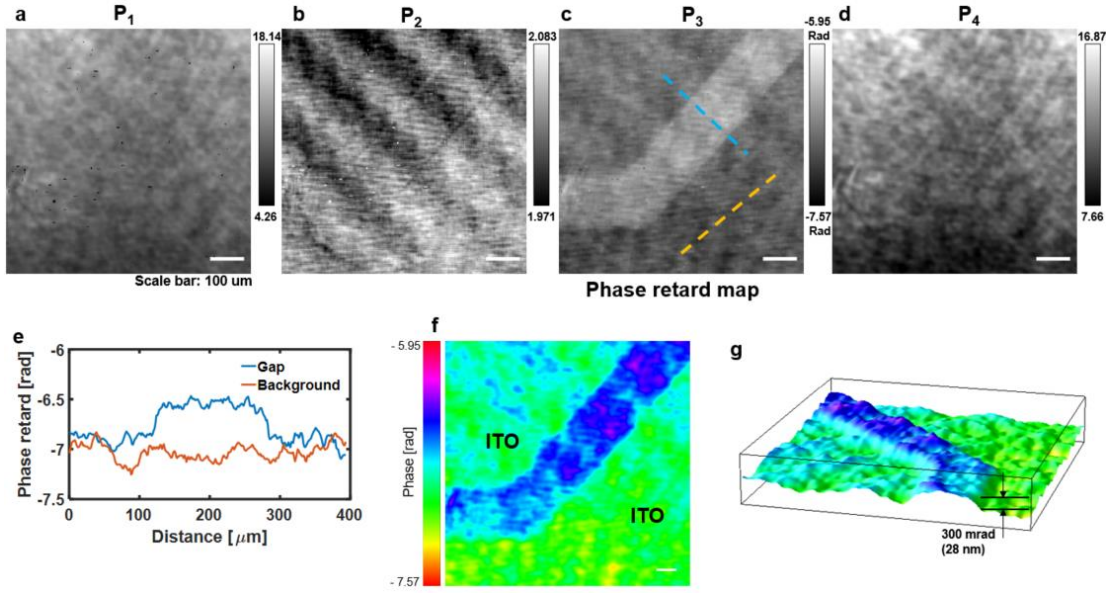

Fig. 4-22. Quantitative phase image reconstruction by sine fit. **a-d**, 4 Parameter images obtained by fitting the image stack of **Fig. 4-20e** to sine function: $P_1 sin(P_2 * \theta - P_3) + P_4$, where the parameter P_3 indicates a QPI image. **e**, Line profile of the QPI image from the ITO background and the gap respectively. **f**, QPI image rendered by "Phase" color code. **g,** 3D view of the QPI image.

In the sine fit method above, a robust fitting requires an image stack with as many images as possible. While the acquisition of multiple images is time consuming due to the rotation of analyzer. During the time of measurement, ambient vibration might be introduced to the interferometer to increase the noise. To reduce the imaging time, here we introduce 4-step phase-shifting method for QPI imaging, where only 4 intensity images from analyzers of 315°, 0°, 45°, 90° are needed.

According to the phase-intensity relation given in eq. 4-28, 4 frames of MIR off intensity images at analyzer angle of 315°, 0°, 45°, 90° can be expressed as:

$$I_{1(x,y)} = I_0/2\left(1 + sin\left(630° + \phi_{0_{(x,y)}}\right)\right) \qquad \textit{eq. 4-29}$$

$$I_{2(x,y)} = I_0/2\left(1 + sin\left(0° + \phi_{0_{(x,y)}}\right)\right) \qquad \textit{eq. 4-30}$$

$$I_{3(x,y)} = I_0/2\left(1 + sin\left(90° + \phi_{0(x,y)}\right)\right) \qquad \textit{eq. 4-31}$$

$$I_{4(x,y)} = I_0/2\left(1 + sin\left(180° + \phi_{0(x,y)}\right)\right) \qquad \textit{eq. 4-32}$$

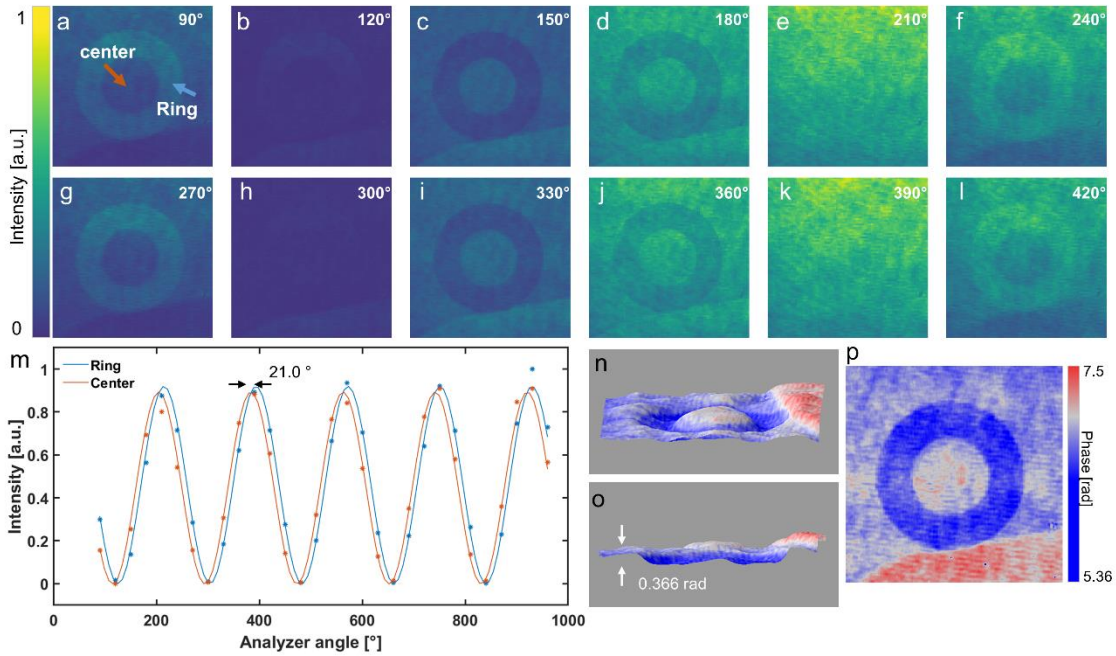

Fig. 4-23. Quantitative phase image of a ring shape ITO structure. a-l, Intensity images of ring shape ITO structure when polarizer angle θ (analyzer) varying from 90° to 420° with step of 30 °. **m,** Sine fits of two points from the ITO structure (indicated by "Ring"), and background (indicated by "center"). **n,o,** 3D illustration of the phase retard. **p**, Quantitative phase image of the phase ring (i.e., phase retardation map).

Tangent of intrinsic-phase can be obtained using the above 4 intensity images.

$$\frac{I_{2(x,y)} - I_{4(x,y)}}{I_{3(x,y)} - I_{1(x,y)}} = \frac{I_0/2\left(1 + sin\left(\phi_{0(x,y)}\right) - 1 + sin\left(\phi_{0(x,y)}\right)\right)}{I_0/2\left(1 + cos\left(\phi_{0(x,y)}\right) - 1 + cos\left(\phi_{0(x,y)}\right)\right)} = \frac{sin\left(\phi_{0(x,y)}\right)}{cos\left(\phi_{0(x,y)}\right)}$$
$$= \tan\left(\phi_{0(x,y)}\right) \qquad \textit{eq. 4-33}$$

Therefore, we have:

$$\phi_{0(x,y)} = tan^{-1}\left(\frac{I_{2(x,y)} - I_{4(x,y)}}{I_{3(x,y)} - I_{1(x,y)}}\right) \qquad \textit{eq. 4-34}$$

One can notice that the initial intensity $I_0/2$ is canceled out from eq. 4-33. With this cancelation, the intrinsic-phase obtained by eq. 4-34 is not affected from the Gaussian profile of the probe beam, where in the Gaussian beam I_0 is location dependent. However, since the codomain of the arctangent function is limited in range of $(-\pi/2, \pi/2)$, the intrinsic-phase obtained using eq. 4-34 is wrapped to the range of $(-\pi/2, \pi/2)$. Therefore the phase unwrapping method is used.

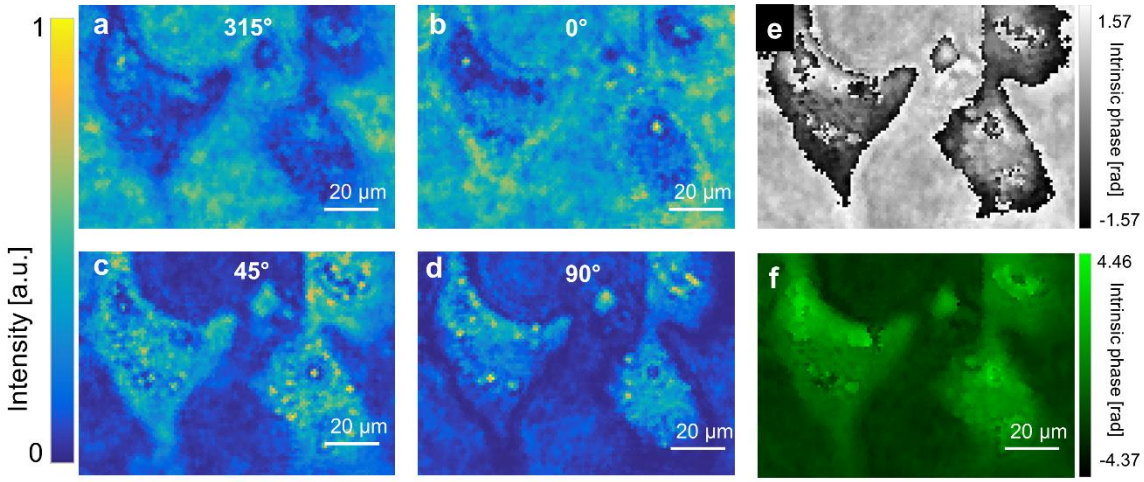

Fig. 4-24. Intensity images and QPI image of 3T3-L1 cells from small FOV. **a-d**, Intensity images of cells at analyzer angle of 315°, 0°, 45°, and 90°. **e**, Phase-wrapping intrinsic-phase image reconstructed according to eq. 4-34. **f,** QPI image reconstructed from (e) by applying quality guide phase unwrapping method (*83*, *84*).

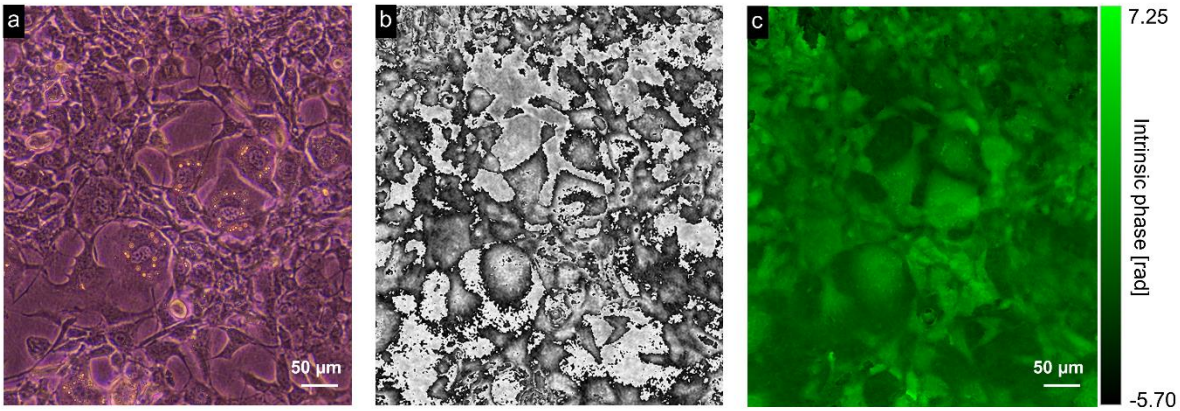

Fig. 4-25. QPI phase of 3T3-L1 cells from large FOV (500×437 μm). a, ZPC image of the FOV. **b**, Wrapped phase image obtained by eq. 4-34. **c,** Unwrapped QPI phase (intrinsic-phase) image.

To validate the 4-step phase-shifting QPI method, we performed the measurement on the 3T3-L1 cells using PSM. **Fig. 4-24** and **Fig. 4-25** show two measurements of 3T3-L1 cells in a small FOV for illustrating single cell (**Fig. 4-24**) and a large FOV (**Fig. 4-25**) for covering a large number of cells. **Fig. 4-24**a-c show the PSM intensity images from analyzer angles of 315°, 0°, 45°, 90°. By applying eq. 4-34, a phase wrapping image is obtained as shown in **Fig. 4-24**e (**Fig. 4-25**b in the case of large FOV). QPI

images can be further reconstructed using quality guide phase unwrapping method (*83, 84*), as shown in **Fig. 4-24**f and **Fig. 4-25**c.

4.3Summary

Phase contrast imaging modality is capable of converting a phase image to an intensity image, where the intensity is linearly or non-linearly related to the phase. This chapter mainly discussed two phase contrast imaging methods: Condenser-free Zernike phase contrast (CF-ZPC) microscopy and phase-shifting microscopy (PSM).

In the discussion of CF-ZPC microscopy, we analytically developed a phase-intensity relation of CF-ZPC in the scenario of thin sample and scenario of thick sample. To explore the imaging characterization of CF-ZPC, we established a wavefront propagation simulation of CF-ZPC, and simulated the imaging performance and compared with the experimental results.

To discuss phase-shifting microscopy, we first introduced the polarization phase-shifting interferometer (PSI), and Jones calculus. Utilizing the Jones calculus, we were able to mathematically deduce the phase-intensity relation of PSI. We later discussed the polarizations of the beam at each stage of system to understand the phase-shifting mechanism carried out by PSI. We later incorporated the PSI with an infinite correct microscope to build a phase-shifting microscope. The experimental validation of phase-shifting microscopy was achieved by imaging phase sample ITO target and the living cells. Finally, we introduced the quantitative phase imaging (QPI) capability of PSM.

Chapter 5 Implementation of wide-field optothermal microscopy by CF-ZPC

This chapter mainly demonstrates the application of CF-ZPC for achieving wide-field optothermal mid-infrared microscopy (WOMiM). As a pilot study, we firstly validate the imaging concept that has been discussed in section 3.1, and study the process of optothermal effect in water. Finally, we move to imaging the vibrational contrast of TAG drops.

This Chapter contains the adapted text, figures from the publication by Tao Yuan et al. [Anal. Chem. 2021, 93, 46, 15323–15330]. Copyright [2021] American Chemical Society (*77*).

5.1 Methods

5.1.1 Experimental setup

As shown in **Fig. 5-1**a, WOMiM is pump-probe system, where an optical parametric oscillator (OPO) laser generated MIR pump light, and a CF-ZPC microscope was used for detecting the phase difference introduced by MIR absorption. A triggers generator was used to generate the triggers pulse to synchronize the pump light, probe light (microscopic illumination) and the camera of the microscope.

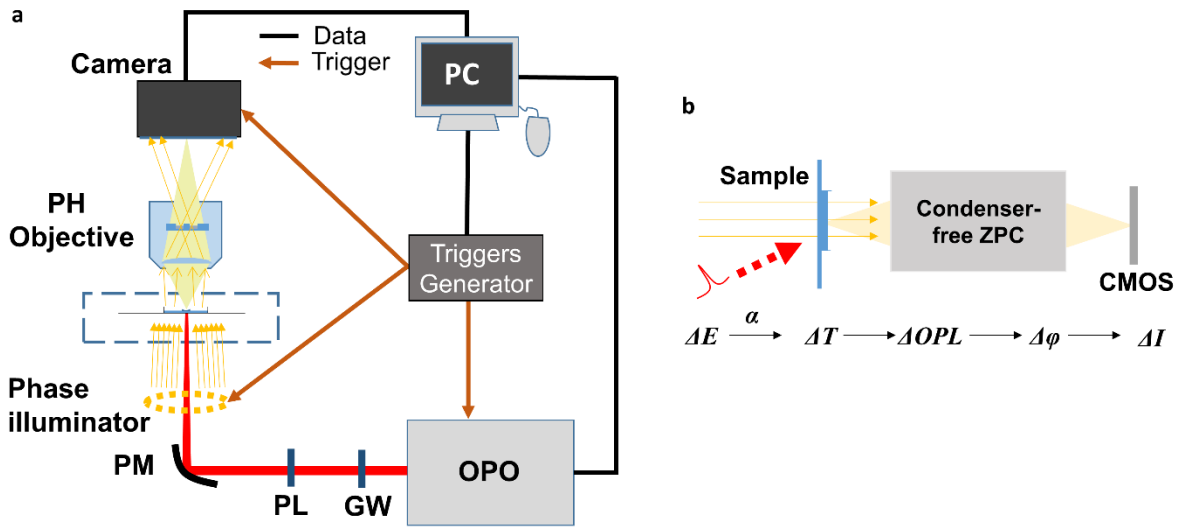

Fig. 5-1. CF-ZPC-based wide-field optothermal mid-infrared microscopy (WOMiM) and evolution of process denoted by physical quantities. a, Diagram of WOMiM. GW: germanium window; PL: MIR polarizer; PM: parabolic mirror; PC: computer. **b**, Illustration of physical process in WOMiM. A mid-infrared laser pulse with energy ΔE is absorbed by the sample. The absorption leads to a temperature increase ΔT due to optothermal effect; the temperature increase results in an optical path change ΔOPL of the probe beam (phase illumination) due to thermo-optics effect and thermal expansion. The optical path change relates to a phase change can be detected as intensity change ΔI by the camera (CMOS sensor) of CF-ZPC microscope.

The pump beam was a 1 kHz pulse light generated from a MIR OPO laser (NT277, EKSPLA; 9 ns pulse width). The OPO output beam first passes through a germanium window (GM) to filter out the visible signal beam (generated by the parametric process inside OPO). The MIR beam –idler beam from the OPO – traveled through a MIR linear polarizer, which can be rotated to adjust the MIR transmission power. After the polarizer, the MIR beam was reflected by a parabolic mirror (#37248, Edmund Optics Ltd.; NA = 0.062) to the bottom of the sample, generating a MIR excitation spot of around 186.2 μm in diameter on the sample plane. To facilitate the MIR penetration, the sample was held on a custom-made petri-dish, the bottom of which was made by a ZnS window (4ZNS F2505, Crystal GmbH).

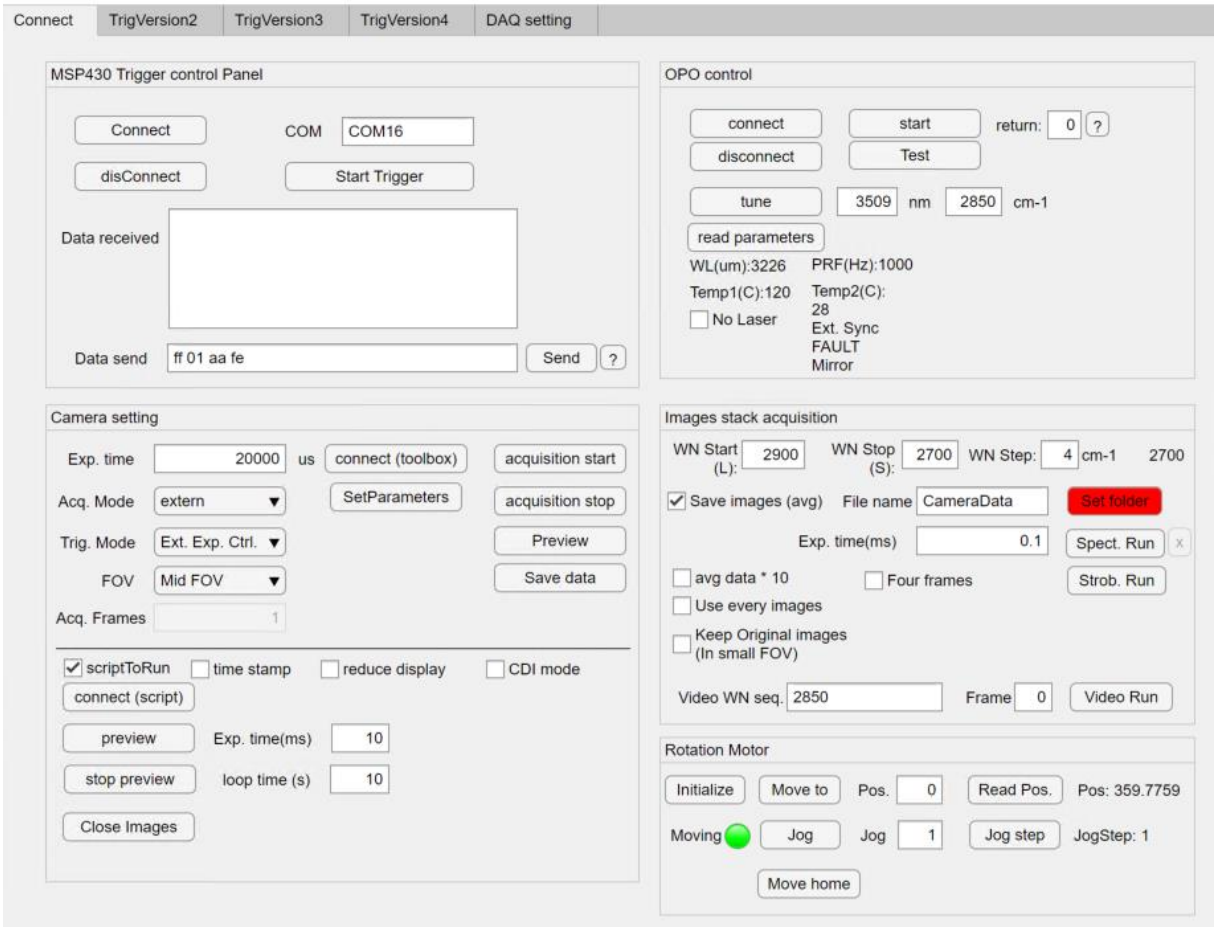

Fig. 5-2. MATLAB user interface of WOMiM.

The probe light was white light generated from an annular illuminator (Aura, Cairn Research Ltd.); and the illuminator was fixed on a plane conjugated to the phase plate of objective (20×, Nikon; NA = 0.4) so that the Zernike phase contrast can be generated properly. A hole in the middle of the annular illuminator permitted the perpendicular transmission of MIR light through the illuminator, to irradiate the sample vertically. On top of the microscopy, a high-speed camera (PCO.dimax cs4, PCO AG) was installed to capture the phase images (MIR-ON/MIR-OFF).

The high-speed camera, OPO laser were connected to a programmable microcontroller (MSP430, Texas Instruments Inc.), which worked as a trigger generator. High time-precision trigger pulses were generated using timer interrupt of the microcontroller. The high-speed camera and the microcontroller were connected to the computer to work collaboratively. The whole system was operated by a custom-made MATLAB user interface (coded by Appdesigner, see **Fig. 5-2**).

5.1.2 Synchronization

In proof-of-concept measurements (will be discussed in **section 5.2**), the camera was synchronized with ON/OFF states of the MIR OPO laser (refer to as "ON-OFF-level synchronization"). In ON-OFF-level synchronization as shown in **Fig. 5-3**, switching frequency of OPO was c.a. 0.117 Hz (period: 8.5 s), and the camera captured images at frame rate of 0.235 Hz (period: 4.25 s, the capture frequency was double of MIR switching frequency). An exposure delay of 4 s existed between camera exposure time and OPO state toggle time (see **Fig. 5-3**b) to allow sample to be heated up or cooled down, so that a true "Hot" image, and "Cold" image can be acquired. The exposure time of MIR-OFF and MIR-ON image were both 250 ms. Despite its slow switching frequency of MIR, ON-OFF-level synchronization provided a straightforward method for characterizing and demonstrating the working principle of WOMiM.

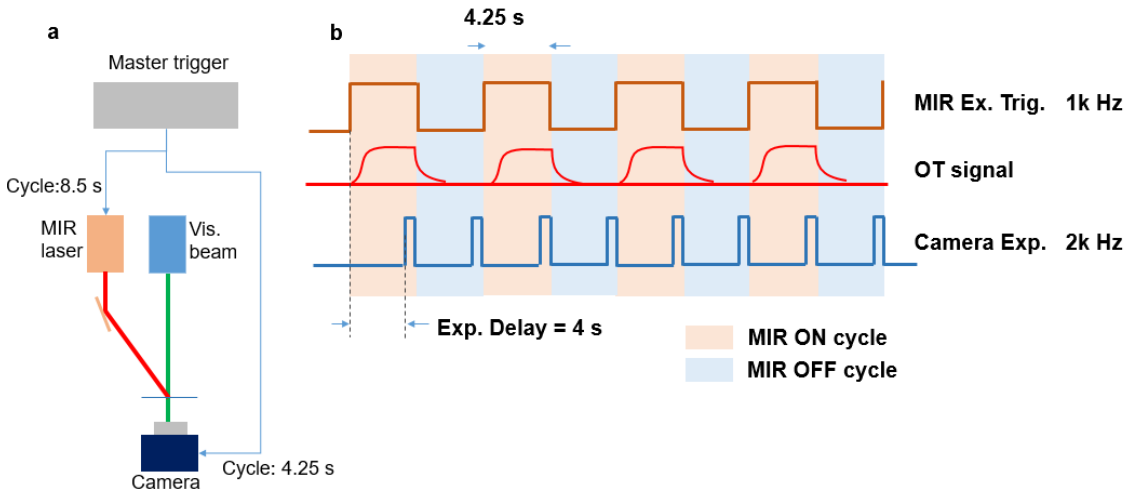

Fig. 5-3. ON-OFF-level synchronization. **a**, Trigger connection of WOMiM. **b**, Synchronization logic of ON-OFF-level synchronization.

For the measurements of single-pulse characterization, and hyperspectral imaging (will be discussed in **section 5.3)**, the camera was synchronized with every single MIR pulse (refer to as "single-pulse-level synchronization"). In single-pulse-level synchronization, both MIR-ON and MIR-OFF images were captured at a frame rate of 1 kHz (see **Fig. 5-4**b), with an exposure time of 5.5 μs. With pre-designed sequence that have been programmed in microcontroller, 50 of MIR-OFF images and 50 MIR-ON images were acquired. A subtraction image was obtained by subtracting the average of 50 MIR-ON

images from the average of 50 MIR-OFF phase images. As one can see from **Fig. 5-4**b, an exposure delay existed between the MIR trigger and camera trigger to properly capture the optothermal signal at the time when MIR pulse hit the sample. This exposure delay can be adjusted to obtain the time dependent optothermal signal.

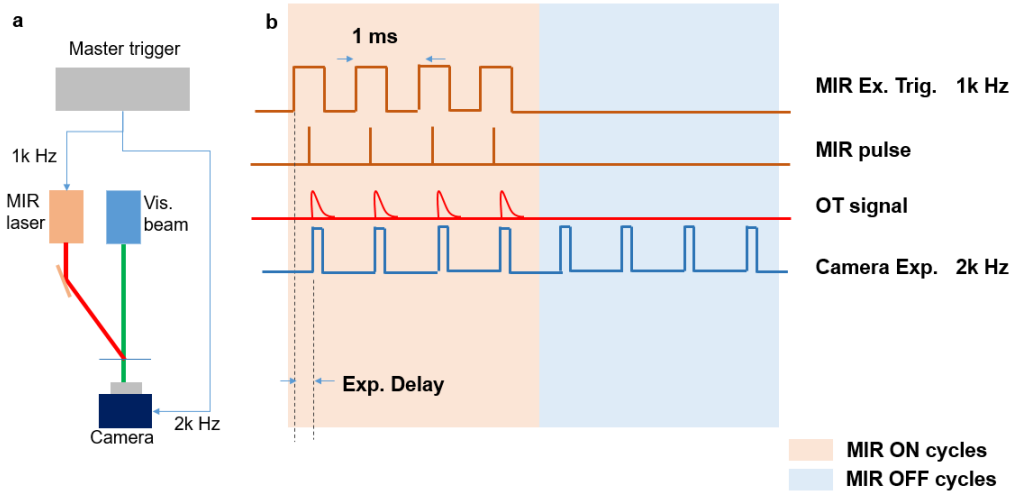

Fig. 5-4. Single-pulse-level synchronization. **a**, Trigger connection of WOMiM. **b**, Synchronization logic of single-pulse-level synchronization.

5.1.3 Sample

We used triglyceride (TAG) as our testing sample, which has abundant CH_2 and CH_3 groups in its chemical structure. The CH bond vibrational information from these two groups can be studied by tuning the MIR excitation wavenumber to around 2850 cm^{-1} or 2920 cm^{-1}. TAG drops were prepared by dissolving 1 mg of 1,2-dioleoyl-3-palmitoyl-rac-glycerol (Sigma-Aldrich Inc.) solution in 100 µL of a chloroform–methanol solution (2:1), and then placing 2 µL of the prepared solution on custom-made Petri dish (with a ZnS window as bottom). The TAG drops with size around 1 µm to 20 µm can be obtained after the evaporation of chloroform–methanol.

5.2 Proof-of-Concept measurement

Using ON-OFF-level synchronization (discussed in **section 5.1**), imaging concept in **Fig. 5-5b** can be validated experimentally in **Fig. 5-5c-e**, where a MIR-OFF image (**Fig. 5-5**c), a MIR-ON image (**Fig. 5-5**d) (MIR at 2850 cm^{-1}), and a subtraction image (**Fig. 5-5**e) of TAG drops on petri-dish are shown. One can observe from the subtraction image (**Fig. 5-5**e) that center of TAG drops shows positive value (red) due to the intensity increase in the MIR-ON image, whereas subtraction value of background (region where there is no TAG drop) is close to zero since the background does not absorb MIR light.

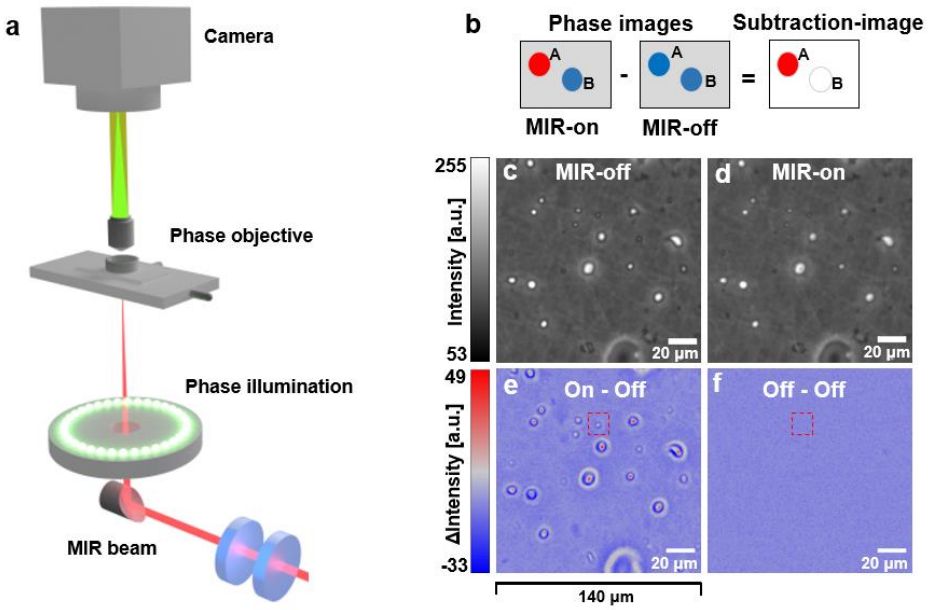

Fig. 5-5. 3D representation of WOMiM and its imaging acquisition. **a,** 3D presentation of WOMiM. **b,** Cartoon demonstration of how WOMiM generates an image. **c-e**, Experimental demonstration of the WOMiM image generation: Firstly, a MIR-ON and a MIR-OFF image are acquired respectively (c,d); then a WOMiM image (e) is obtained by subtraction of the two images, illustrating the difference caused by MIR absorption. **f**, The subtraction does not show contrast if both images are MIR-OFF. Sample in (c-f): Triglyceride (TAG) drop in open air. The figure is adapted from ref. (*77*).

Fig. 5-5f shows a subtraction image from a control experiment, where both phase images were acquired without MIR (MIR-OFF images). The control experiment shows no TAG drop, suggests that the image contrast of **Fig. 5-5e** is related to MIR illumination only. The standard deviation (STD) of the all image pixels of **Fig. 5-5f** is calculated as 1.02 in grayscale, serving as the STD of optical noise. Since the STD of noise is close to grayscale unit of 1 (analog to digit conversion resolution), the optical noise might bellow the detection ability of camera.

To characterize the resolution of WOMiM, **Fig. 5-6**a,b show two zoomed in subtraction images of a FOV with a smallest observed TAG drop, as marked by red dashed squares in **Fig. 5-5**e,f. **Fig. 5-6**c plots the line profiles crossing center of the TAG drop, as well as a line profile of the same location in **Fig. 5-6**b. As indicated in **Fig. 5-6**c, the line profile of the TAG drop gives a Full-Width-at-Half-Maximum (FWHM) of 1.85 µm, which is close to Abbe diffraction limit of 1.75 µm when using a high NA MIR objective ($d = \lambda/2NA$, where NA = 1 and $\lambda = 3.508$ µm). WOMiM approaches this limit with low NA optics (i.e., a MIR parabolic mirror with NA = 0.062 and a visible objective with NA = 0.4). WOMiM achieves high resolution MIR image with low NA optics by using the pump-probe detection, where the resolution of a MIR absorption image is determined by the wavelength of visible light instead of wavelength of MIR

light itself (WOMiM uses white light as probe light which has wavelength range: 400-800 nm, and wavelength of MIR light is 3.5 μm in experiment of **Fig. 5-5/Fig. 5-6**).

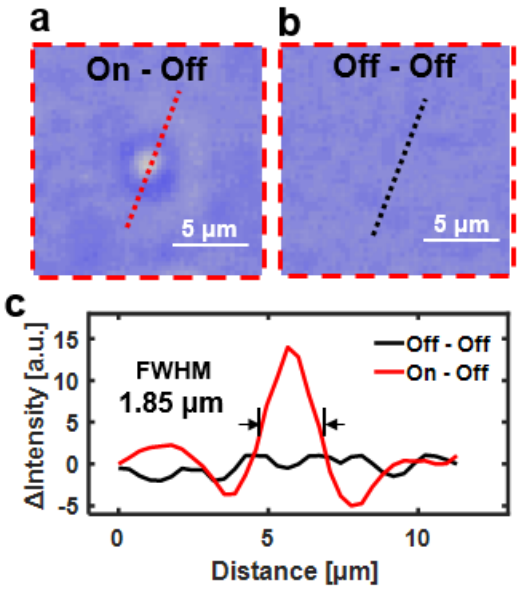

Fig. 5-6. WOMiM imaging resolution characterization. a,b, Imaging FOV of a smallest TAG drop from **Fig. 5-5**e (marked by the red dashed square), and a corresponding area of **Fig. 5-5**f. **c**, Line profiles crossing the center of TAG drop from (a) and (b) were plotted respectively. The figure is adapted from ref. (*77*).

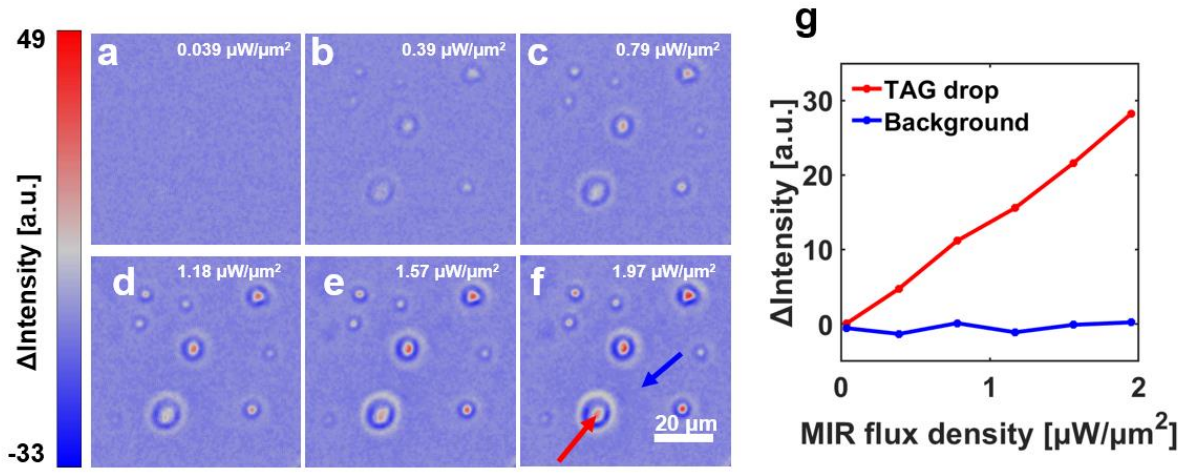

Fig. 5-7. Linear relation of subtraction image intensity and the pump Power Flux Density (PFD). a-f, Subtraction images as pump PFD increasing from 0.039 μW/μm^2 to 1.97 μW/μm^2. **g**, Plot of the subtraction intensity varying according to the pump PFD (values obtained from two locations as indicated in (f). The figure is adapted from ref. (*77*).

To understand the relation between the MIR pump power and the imaging contrast of subtraction image, we acquired subtraction images under different MIR pulse energy (achieved by rotating the MIR polarizer in **Fig. 5-1**a), i.e., under different MIR Power Flux Density (PFD, radiant energy per unit time

per unit area). **Fig. 5-7**a-f depict six subtraction images acquired as the MIR PFD increasing from 0.039 to 1.97 μW/μm^2. From **Fig. 5-7**a-f, it is observed that the imaging contrast enhances as the increase of MIR power flux density. The subtraction values of a TAG drop (red arrow in **Fig. 5-7**f) from these 6 images is observed to be linearly correlated with MIR PFD, as shown in **Fig. 5-7**g. For comparison, the background (blue) stays near 0 during the increasing of pump PFD. Importantly, the image contrast can be observed at a low power flux density of 0.39 μW/μm^2 (**Fig. 5-7**b), which is ~5 orders of magnitude lower than the pump power flux density of Raman microscopy (15 mW/μm^2) (*85*) because Raman microscopy focuses light on a small spot (as shown in **Fig. 3-1**d) to irradiate the sample. The low MIR flux density provides an advantage of reducing photodamage to living cells, which has been observed in Raman scattering base microscopies (*40, 41*).

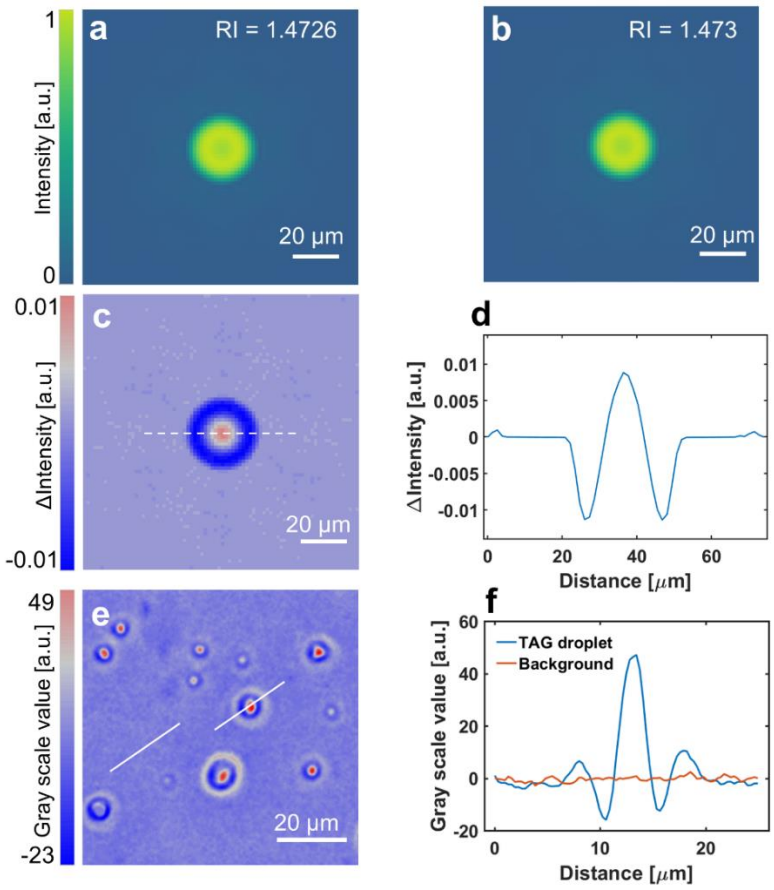

Fig. 5-8. Simulation of the WOMiM's imaging acquisition. a,b, Two images of micro lens acquired by simulation of CF-ZPC, simulating the imaging of TAG drop. The refractive index is 1.4726 and 1.473 respectively. The diameter of the micro lens is 30 μm. **c,d,** Subtraction image and profile of micro lens from simulation (Fig. b minus Fig. a). **e,f,** Subtraction image and profile of TAG drop by experiment. RI: refractive index; TAG: triglyceride.

As observed in the subtraction images in **Fig. 5-5** to **Fig. 5-7,** the absorption of MIR light leads to a positive center and negative "Halo" for each TAG drop. One can understand this phenomenon using the

simulation discussed in **section 4.1.3**. As shown in **Fig. 5-8**, the TAG drop in MIR-ON and MIR-OFF states are modeled by a virtual micro lenses with different refractive indexes, and their corresponding ZPC images were obtained using simulation of CF-ZPC. Consider the negative thermo-optic coefficient of TAG (see Table 3-1), the refractive index of MIR-ON is configurated as 1.4726 (as shown in **Fig. 5-8**a); the refractive index of MIR-OFF is configurated as 1.473 (as shown in **Fig. 5-8**b). With this configuration, the refractive index difference of these two cases (MIR-ON/MIR-OFF) corresponding to temperature change of around 1 °C (tacking into account the thermo-optic coefficient of TAG in Table 3-1). **Fig. 5-8**c shows a subtraction image obtained by subtracting **Fig. 5-8**b (MIR-OFF) from **Fig. 5-8**a (MIR-ON). Similar to the experimental result, the subtraction image illustrates a positive center surrounding by a negative "Halo". The negative "Halo" is created due to the fact that in the phase-intensity relation of a positive phase contrast objective (**Fig. 4-3**a), a positive slope exists on the region near phase retard of 0 rad (that is, the phase retard range of [-0.3 0] rad). Using this information, one can quantitatively assign the phase of [-0.3 0] rad to the halo region of a ZPC image, although ZPC is known as a qualitative phase contrast method.

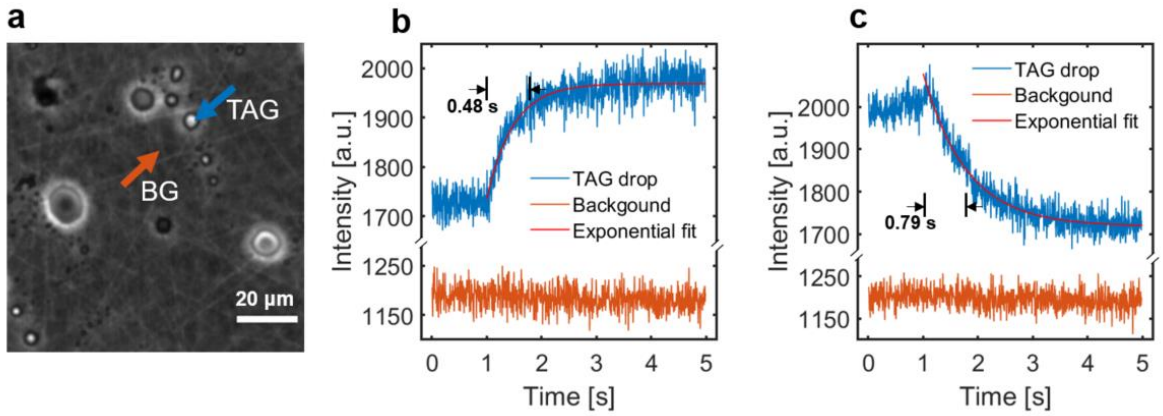

Fig. 5-9. Heating up and cooling down process of TAG drops. a, The image FOV, with the TAG drop marked by the blue arrow, and background marked by the orange arrow. **b,** Intensity of the TAG drop and background (marked in **Fig. 5-9a**) plotted over observation time. The MIR laser was off at beginning, and was turned on at time = 1 s to demonstrate the heating up process. **c**, Intensity profile of TAG drop and background plotted over time. The MIR laser was on at beginning, but was turned off at time = 1 s to observe the cooling down process. Sample: Triglyceride (TAG) in open air. The figure is adapted from ref. (*77*).

Study of the heating up and cooling down process of optothermal transition can be achieved by monitoring the sample during the switching of MIR laser. **Fig. 5-9** shows an experiment demonstrating the heating up and cooling down process during the time course of MIR switching. In this measurement, the camera kept running over a time course of 5 s, and captured video on a FOV as shown in **Fig. 5-9a**. The heating up measurement started with MIR off state; and the MIR laser switched on at time = 1 s. In the cooling down measurement, the MIR switched off at time = 1 s. **Fig. 5-9b,c** shows the two

measurements respectively, plotting the intensity of a TAG drop and intensity of background over time. As we can see in **Fig. 5-9b**, the intensity of TAG increase immediately as the MIR switching on. The temporal profile of the intensity of TAG can be fitted to an exponential curve with time constant of 0.48 s. For comparison, the temporal profile of background stays at a stable level over time. In the cooling down experiment of **Fig. 5-9c**, the intensity of TAG decrease immediately as the MIR switching off. The exponential fit of the cooling down process gives a time constant of 0.79 s. Both time constant of heating up and cooling down are much less than the exponential delay (4 s) of ON-OFF-level synchronization (as shown in **Fig. 5-3**).

5.3 Optothermal signal characterization and hyperspectral imaging

Since the cells are living in aqueous environment, optothermal signal characterization in water is fundamental for applying this technology for imaging of cells. Knowing that the water has the highest specific heat capacity among the liquids, the optothermal signal time course in water should be much shorter than in open air condition. Therefore the slow ON-OFF-level synchronization is not suitable for observing the optothermal signal in water. To achieve the aim of observing optothermal signal in water, we take the advantage of pulse MIR laser, and designed single-pulse-level synchronization for WOMiM (**Fig. 5-4**).

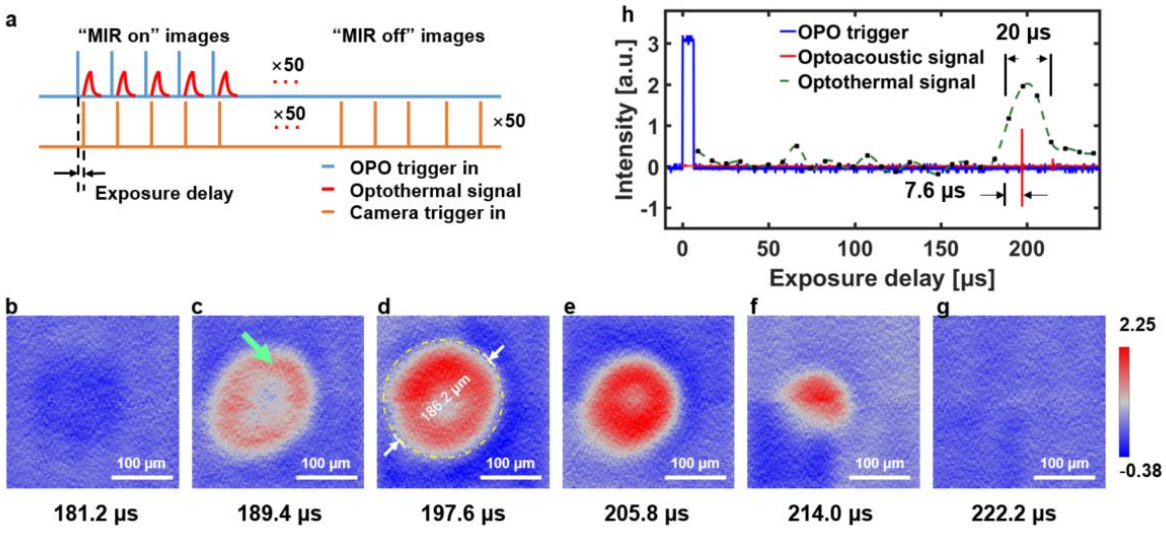

Fig. 5-10. Single-pulse-level synchronization and optothermal signal characterization in water. a, Diagram of trigger trains for single-pulse-level synchronization. **b-g,** WOMiM images of optothermal signal in water at exposure times ranging from 181.2 to 222.2 µs (MIR wavenumber: 3510 cm^{-1}). **h,** Plot of OPO external trigger, optothermal signal obtained from the WOMiM images, and an optoacoustic single. The figure is adapted from ref. (*77*).

As shown in **Fig. 5-10**, the microcontroller generated 1 kHz external trigger trains to drive the OPO laser, resulting in a 1 kHz output of MIR pulses. A similar 1 kHz external trigger was also generated for

activating the high-speed camera to capture the phase images. Due to the internal electric delay, the MIR pulse was not immediately generated upon receiving an external pulse. A delay (referred to as "exposure delay") was introduced to the camera exposure trigger pulse to synchronize the exposure time with the MIR generation time. As the pre-determined number (for instance, we used 50) of MIR-ON images obtained, the OPO external trigger stops, and the camera continues to acquire same number of MIR-OFF images. Then the average of 50 MIR-ON images subtracted the average of 50 MIR-OFF images for a WOMiM image.

To characterize the temporal profile of the single-pulse optothermal signal, we varied the exposure delay so that different stages of the optothermal signal development could be captured. As shown in **Fig. 5-10**b-g, six WOMiM subtraction images acquired at exposure delay of 181.2 μs, 189.4 μs, 197.6 μs, 205.8 μs, 214.0 μs, and 222.2 μs are depicted (MIR wavenumber: 3510 cm^{-1}). No optothermal signal can be observed at an exposure delay of 181.2 μs (**Fig. 5-10**b) since the MIR pulse has not yet reach the sample when the camera started exposing (i.e. pre-excitation stage). The first subtraction image with optothermal signal was observed at exposure delay of 189.4 μs (**Fig. 5-10c**), illustrating a hot spot. And the signal reached maximum at exposure time of 189.4 μs, and decreased afterward. At exposure delay of 222.2 μs, the FOV returned back to the pre-excitation stage as **Fig. 5-10**b, in which no optothermal signal can be observed. The above observation suggests that the optothermal signal last around 32.8 μs (222.2–189.4 μs) in water. This is time course much shorter than the open air case in **Fig. 5-9**b,c, which have time constants of 0.48 s and 0. 79 s. The optothermal signal lasted shorter due to the large specific heat capacity of water, which any heat increase can be dissipated away in a very fast way. As the optothermal signal reach its maximum, the hot spot spanned a circle area with diameter of 186.2 μm (**Fig. 5-10d**). The area is the effective optothermal FOV of WOMiM, which can be expanded by vertically changing the position of parabolic mirror (see **Fig. 5-5**a).

Beyond the six frames presented in **Fig. 5-10**b-g, further measurement was performed by changing exposure delay from 9 μs to 238.6 μs, with step of 8.2 μs, obtaining a subtraction image stack with total 29 images. As shown in **Fig. 5-10h**, intensity of a location (as indicated in **Fig. 5-10c**) from the whole subtraction image stack is plotted over time. A cubic spline interpolation was applied to the data points in **Fig. 5-10**h for further analysis. The FWHM of optothermal time course was observed to be ~20 μs. For comparison, the optoacoustic signal was also acquired by substituting the objective by a transducer, and using data acquisition card to acquire the signal of transducer. As we can see, the optoacoustic signal (around 200 ns) was much shorter than the optothermal signal. Moreover, the optoacoustic signal was around 7.6 μs behind the optothermal signal, this is because the optothermal signal was probed by the visible light, and the light speed was much faster than acoustic wave in water (Consider the working distance of transducer: 1 cm, the acoustic wave need to travel 1 cm to reach the transducer).

In the above single-pulse optothermal signal characterization, 50 of MIR-ON image have been acquired and averaged for WOMiM image, corresponding to a time course of 50 ms. During this time course, the energy of 50 MIR pulses keep accumulating in the water. Although the energy of a single pulse dissipates locally in a fast way (32.8 µs) as shown in **Fig. 5-10**, the global heat of the water keep increasing until a thermal equilibrium established. To demonstrate the heating process within this 50 ms time course, **Fig. 5-11** presents the intensity variation of the excitation area from the 50 MIR-ON images, and 50 MIR-OFF image (2.9 s after excitation). The experiment was performed at MIR wavenumber of 3530 cm^{-1}, 3300 cm^{-1}, and 3100 cm^{-1} respectively. **Fig. 5-11**a shows a MIR-ON image, and **Fig. 5-11**b plots the time profile of intensity in a circle indicated in **Fig. 5-11**a.

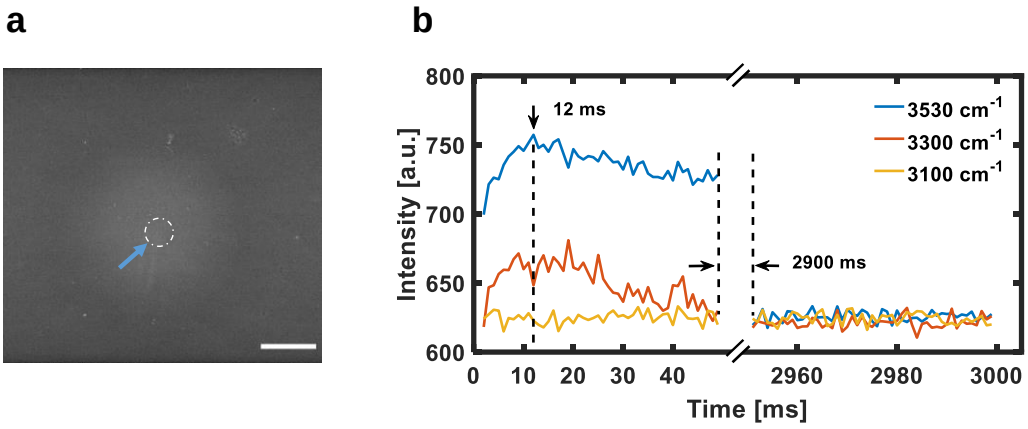

Fig. 5-11. Image stack of 50 MIR pulses and its corresponding intensity variation. a, One image from image stacks. Scale bar: 100 µm. **b,** Z-profiles of an area marked by the white circle in (a). Here, three z-profiles from three stacks are shown, corresponding to wavenumber of 3530 cm^{-1}, 3300 cm^{-1} and 3100 cm^{-1}. The z-profile value is average intensity of the white circle. In this measurement, the OPO was turned on for 50 ms to acquire 50 MIR-ON images. After the MIR-ON image acquisition was complete, the OPO was turned off. The camera was turned on again 2.9 s after MIR-ON image acquisition; 50 MIR-OFF images were acquired without MIR illumination.

In **Fig. 5-11**b, a difference of around 125 greyscale between MIR-ON and MIR-OFF is observed for measurement at wavenumber of 3530 cm^{-1}. The intensity reached its maximum at 12th ms after MIR switched on. Afterward, the intensity slightly dropped down but was still higher than MIR-OFF. For the measurement at wavenumber of 3300 cm^{-1}, the intensity maximum was also observed around 12th ms. After that, it dropped down to MIR-OFF level at the end of MIR-ON time course. For wavenumber of 3100 cm^{-1}, MIR-ON and MIR-OFF were found to have same intensity probably due to the low phase sensitivity of ZPC microscope.

To understand how the WOMiM image (subtraction image) contrast changing regarding to the wavenumber of excitation beam, we fixed the exposure delay to the maximum value found in **Fig. 5-10**, which is 197.6 µs, and varying the excitation wavenumber from 2800 cm^{-1} to 3500 cm^{-1} (as shown in **Fig. 5-12**) to acquire a hyperspectral stack of water. In **Fig. 5-12**a, three spectra were extracted from three

different locations of the hyperspectral imaging stack. An absorption peak around 3500 cm^{-1} was observed, coinciding with the OH asymmetric stretching absorption peak around 3500 cm^{-1} (*59*).

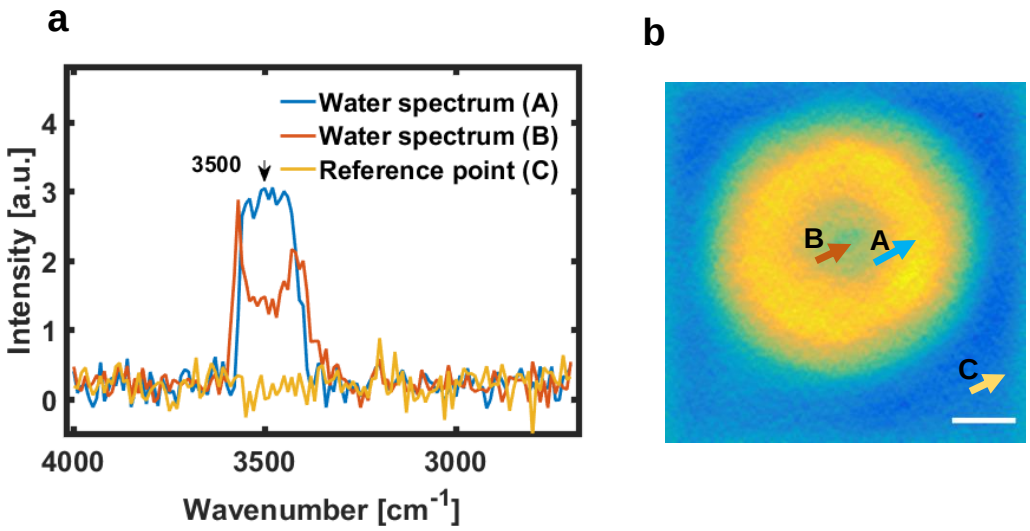

Fig. 5-12. Wavenumber dependent of WOMiM image contrast. a, Water spectra obtained from two MIR illuminated locations and a reference point. **b,** Locations where the spectra were extracted. Scale bar: 50 μm. For point A, absorption peak at wavenumber of 3500 cm^{-1} was observed. While for the center point B, we saw a wrap of the peak at around 3500 cm^{-1}. This is probably caused by the phase wrapping when phase advance (consider thermo-optics coefficient of water) more than $\pi - 0.3$ rad, as shown in **Fig. 4-3**a.

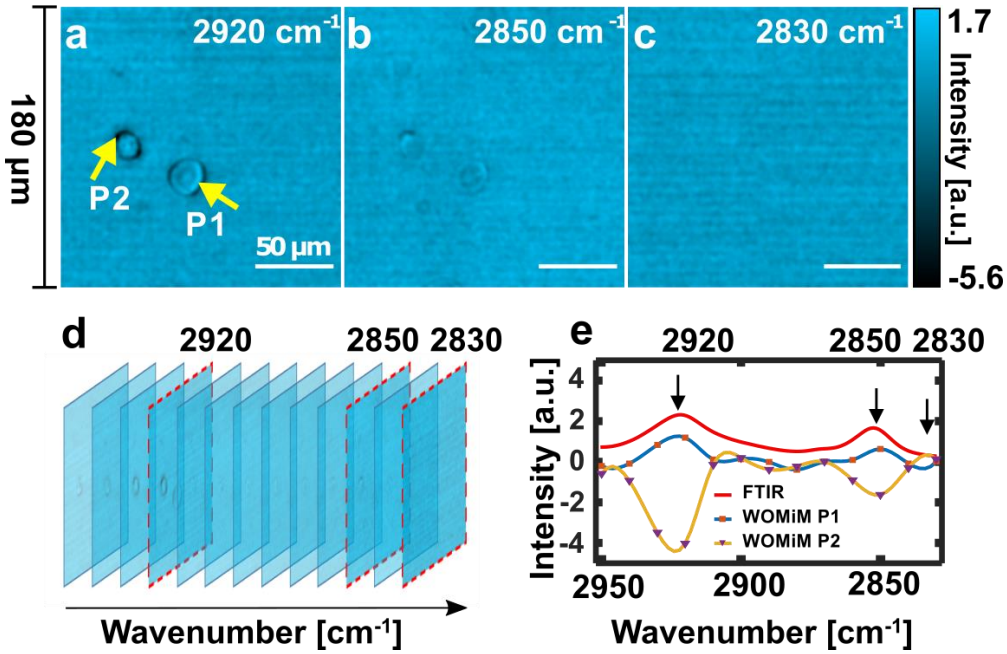

Fig. 5-13. Hyperspectral imaging of TAG drop in water. a-c, Three WOMiM subtraction images acquired at MIR wavenumber of 2920 cm^{-1}, 2850 cm^{-1}, and 2830 cm^{-1}, respectively. **d,** Hyperspectral imaging stack. **e**, Spectrum of TAG extracted from the hyperspectral imaging stack and compared with spectrum of TAG acquired from Fourier-transform infrared spectroscopy (FTIR). The figure is adapted from ref. (*77*).

To validate WOMiM's chemical-contrast imaging ability, a hyperspectral imaging measurement was performed using TAG drops in water, as shown in **Fig. 5-13**. **Fig. 5-13**a-c depicts three WOMiM images from wavenumber 2920, 2850, and 2830 cm^{-1}, respectively. TAG drops were observed at wavenumber of 2920 and 2850 cm^{-1}, invisible at wavenumber of 2830 cm^{-1}. This can be understood since both 2920 cm^{-1} and 2850 cm^{-1} are absorption peaks of TAG, corresponding to the CH_2 asymmetry stretch vibration and CH_2 symmetry stretch vibration. The three images in **Fig. 5-13**a-c were obtained from the hyperspectral imaging stack of 13 images **Fig. 5-13**d, covering the wavenumber range of 2950 to 2830 cm^{-1}. It is worth noting that benefiting from the high imaging speed, the net acquisition time of the stack only took around 0.26 s. In **Fig. 5-13** the comparison of spectrum from Fourier-transform infrared spectroscopy (FTIR) and WOMiM agree well with each other, both show two absorption peaks around 2920 and 2850 cm^{-1}.

5.4 Summary

This chapter mainly focuses on an approach for implementing wide-field optothermal microscopy based on CF-ZPC microscope. As discussed in Chapter 3, the wide-field optothermal microscopy is a pump-probe system where the mid-infrared (MIR) light works as the pump beam, and the visible phase imaging system serves as probe system. To achieve snapshot of a large FOV, the MIR beam illuminates the sample on a very large area instead of focusing on a single spot. As the wavenumber of MIR light matches the vibrational absorption band of specific chemical bond, the localized temperature increase. Taking the advantage of thermo-optics effect (temperature change induces refractive index change), the corresponding optical path length difference can be observed by a phase imaging system. Therefore, a vibrational contrast image can be obtained by subtracting a MIR-OFF image from a MIR-ON image.

With the working principle introduced, a pilot study of a wide-field optothermal microscopy based on a CF-ZPC microscope is presented in Chapter 5. Here we firstly introduced the building block of whole system, and the external trigger pulses used for synchronizing the pump and probe (section 5.1). Using the described setup, we were able to proof the imaging concept by an MIR-ON/OFF measurement (see **Fig. 5-5**). Later, we were able to characterize its imaging resolution by imaging triglyceride (TAG) drop (see **Fig. 5-6**), and demonstrated that this imaging contrast is linearly correlated with the MIR pump power (see **Fig. 5-7**). With the aid of a simulation discussed in Chapter 4, the imaging contrast of optothermal image of TAG drop can be explained. Furthermore, we also explored the heating up and cooling down process during the switching of the MIR laser (see **Fig. 5-9**), as well as single pulse optothermal signal (see **Fig. 5-10**). Although the cells are living in the water environment, single pulse optothermal characterization on water has not been carried out by the recent studies, instead, it was performed using oil film (or beads in DMSO). The study of thermal process in water provides an experimental foundation for making use of the optothermal mechanism for imaging, and for understanding the imaging speed potential of the imaging concept. For instance, according to the single

pulse optothermal signal characterization in **Fig. 5-10**, the minimum time interval between an MIR-ON (**Fig. 5-10**c) and MIR-OFF (**Fig. 5-10**g) image can be as short as 32.8 μs. It suggests that a pair of MIR-ON and MIR-OFF image can be obtained within 32.8 μs, corresponding to frame rate of c.a. 30 kHz. One can approach this frame rate by increasing the repetition rate of MIR pulse, and frame rate of camera, both are technically feasible. Later, we also shown the hyperspectral imaging capability using this setup. The OH asymmetric stretching absorption peak around 3500 cm^{-1} (*59*), and CH_2 stretching absorption peak around 2920 cm^{-1} is observable in the measurement of water and TAG drops, as shown in **Fig. 5-12** and **Fig. 5-13**. However, due to the detection sensitivity of CF-ZPC microscopy, this setup only able to detect large TAG drops, and lack the sensitivity for small target such as lipid droplets in living cells.

Chapter 6 Implementation of wide-field optothermal microscopy by PSM

Since the CF-ZPC microscope uses common path design and applies incoherent light as light source, it is very stable against the environment disturb and its image is speckle free. The CF-ZPC microscope has been used for proofing the imaging concept of wide-field imaging in Chapter 5. However, it cannot measure quantitative phase change caused by MIR absorption (i.e., MIR-phase), and its image usually suffers from the "Halo" and "Shade-off" artifact. Moreover, its sensitivity to the optical path change is weak, since the phase-intensity conversion relation begins from a valley, where the slope is small (**Fig. 4-3**). In this section, we apply the PSM (have been discussed in **section 4.2**) as phase imaging system for high sensitivity detection of the MIR-phase, hereinafter refer as Phase-Shifting Optothermal Microscopy (PSOM), as shown in **Fig. 6-1**. This Chapter contains the adapted text, figures from the publication by Tao Yuan et al. [Sci. Adv. 2024, 10(8), eadj7944]. Copyright [2024] American Association for the Advancement of Science (*86*).

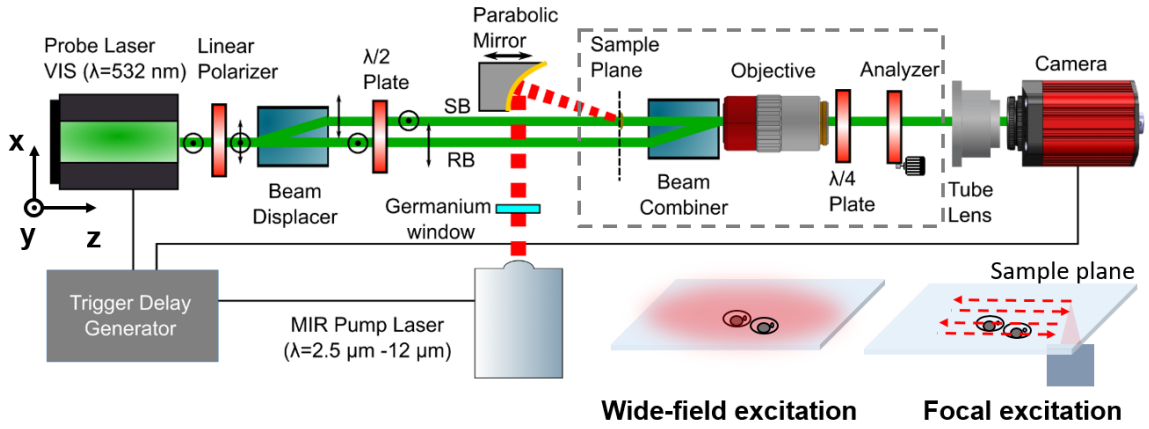

Fig. 6-1. Wide-field optothermal microscopy based on PSM.

Here, a new phase-shifting mechanism for measuring MIR-phase will be introduced in **section 6.1**. Using this phase-shifting mechanism, measuring MIR-phase independent to intrinsic-phase can be achieved, the proof-of-concept measurement of the new system will be demonstrated in **section 6.3,** and later, the system will be characterized and move to measure the living cells as shown in **section 6.4,** and **section 6.5**.

6.1 Phase-shifting mechanism under MIR excitation

In the PSM, without MIR light illuminating the sample, a MIR-OFF intensity $I_{f(x,y)}$ can be written as (from **eq. 4-28**):

$$I_{f(x,y)} = \frac{I_0}{2}\left(1 + sin\left(2\theta + \phi_{0(x,y)}\right)\right) \qquad eq.\ 6\text{-}1$$

When the sample is irradiated by MIR light with wavenumber k (generated by MIR pump laser as shown in **Fig. 6-1**), absorption of MIR light by the sample creates a localized temperature change $\Delta T_{(x,y,k)}$ according to eq. 3-1 (Here use Cartesian coordinates x,y to denote the location).

$$\Delta T_{(x,y,k)} = \frac{\Delta Q_{(x,y,k)}}{c\ m} = \frac{\mu_{(x,y,k)} E_{(x,y)}}{cA\ \rho} \qquad eq.\ 6\text{-}2$$

The temperature increasing results in a local phase perturbation $\Delta\varphi_{(x,y,k)}$ (as see in **eq. 3-6**, termed MIR-phase) that superimposes to the intrinsic-phase $\phi_{0(x,y)}$. Therefore, the MIR-ON intensity image $I_{n(x,y)}$ can be expressed as:

$$I_{n(x,y)} = \frac{I_0}{2}\left(1 + sin\left(2\theta + \phi_{0(x,y)} + \Delta\varphi_{(x,y,k)}\right)\right) \qquad eq.\ 6\text{-}3$$

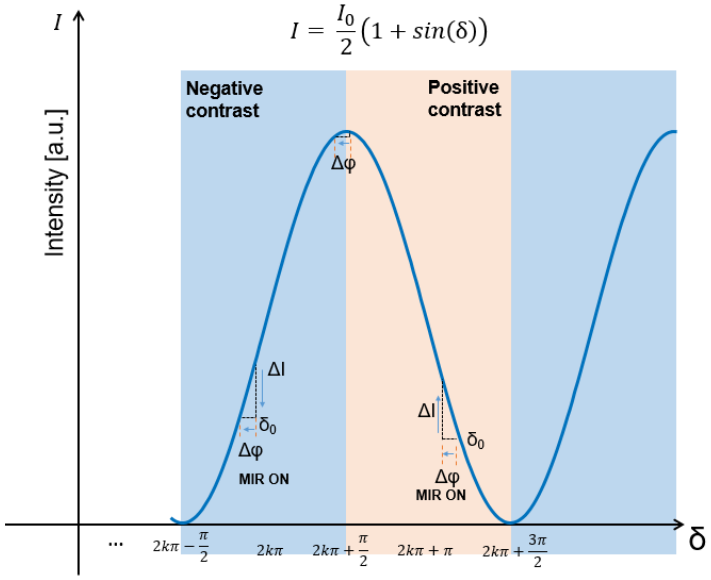

Fig. 6-2. Positive and negative contrast of sinusoidal phase-intensity relation. Here the sinusoidal phase-intensity relation (see **eq. 4-27**, by letting phase sum $\delta = 2\theta + \delta_0$) is plotted. Considering the negative thermo-optic coefficient (*dn/dT*) for triglyceride (*67*), the increasing of temperature causing a decreasing of phase sum δ, i.e., MIR-phase $\Delta\varphi$ is negative. If initial phase sum δ locates in range ($\mathbf{2k\pi - \pi/2}$, $\mathbf{2k\pi + \pi/2}$), a dropdown of intensity can be expected. While if initial phase sum δ locates in range ($\mathbf{2k\pi + \pi/2}$, $\mathbf{2k\pi + 3\pi/2}$), an increase of intensity can be expected. If δ locates close to intensity peak value $\mathbf{2k\pi + \pi/2}$ or intensity valley value $\mathbf{2k\pi + 3\pi/2}$, little change of intensity can be observed.

To obtain the intensity change image $\Delta I_{(x,y)}$, the system subtracts the MIR-OFF intensity image from the MIR-ON intensity image:

$$\Delta I_{(x,y)} = I_{n(x,y)} - I_{f(x,y)} \qquad \textit{eq. 6-4}$$

Here we discuss how the image contrast of $\Delta I_{(x,y)}$ can be affected by the intrinsic-phase: Since the phase-intensity relation **eq. 4-28** is sinusoidal relation, the imaging contrast provided by a single subtraction image $\Delta I_{(x,y)}$ relies on the sum of intrinsic-phase δ_0 and the analyzer angle θ (See **Fig. 6-2**). Depending on whether the sum $\delta = 2\theta + \delta_0$ is located on positive slope or negative slope of the curve, the subtraction can be positive contrast (increase of intensity) or negative contrast (decrease of intensity) (see **Fig. 6-3**). Although the analyzer angle θ is controllable within the sum $\delta = 2\theta + \delta_0$, the intrinsic-phase δ_0 always varies according to different types of sample, which cannot be controlled. Therefore the image contrast of $\Delta I_{(x,y)}$ cannot be used to quantitatively determine if the sample absorb the MIR light.

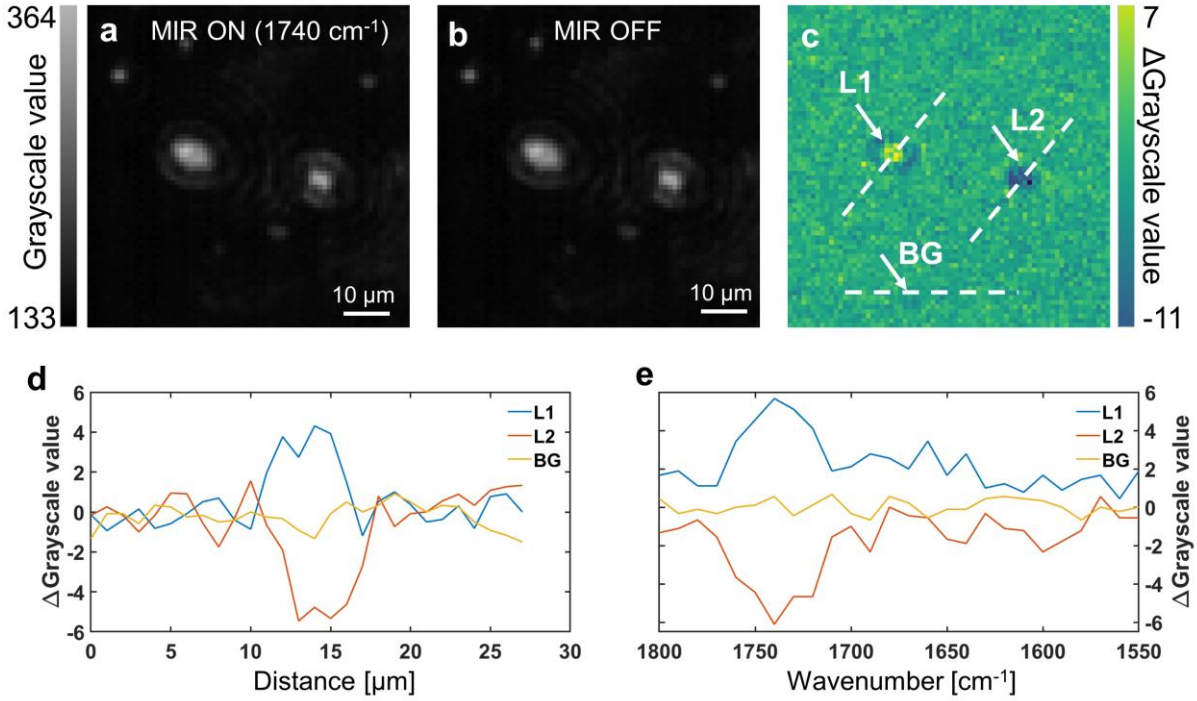

Fig. 6-3. Intensity images of TAG drops and MIR-ON/OFF subtraction. **a**, MIR-ON intensity image at MIR wavenumber of 1740 cm^{-1}. **b,** MIR-OFF intensity image of the corresponding FOV as (a). **c,** Subtraction image (MIR-ON minus MIR-OFF). **d,** Line profiles of two TAG drops and background (as indicated in Fig. c). **e,** Spectra acquired from three locations in (c), in the range of 1550-1800 cm^{-1}. L1 shows positive contrast, and L2 shows negative contrast. The contrast difference is due to whether their intrinsic-phase locate in the positive contrast/negative contrast region as shown in **Fig. 6-2**.

To quantitative obtained the MIR-phase, multiple intensity subtraction images are needed under different analyzer angles. By changing the analyzer angle, the sum $\delta = 2\theta + \delta_0$ can be shifted to a new location of the phase-intensity relation. Here, the phase-shifting mechanism is achieved by rotating the analyzer to angles of 315°, 0°, 45°, or 90° to acquire four intensity subtraction images: $\Delta I_{1(x,y)}$, $\Delta I_{2(x,y)}$, $\Delta I_{3(x,y)}$, $\Delta I_{4(x,y)}$. These four subtraction images can be expressed by (Let I_0 = 1):

$$\Delta I_{1(x,y)} = sin\left(\phi_{0(x,y)} + \frac{\Delta\varphi_{(x,y)}}{2}\right) sin\left(\frac{\Delta\varphi_{(x,y)}}{2}\right) \qquad \textit{eq. 6-5}$$

$$\Delta I_{2(x,y)} = cos\left(\phi_{0(x,y)} + \frac{\Delta\varphi_{(x,y)}}{2}\right) sin\left(\frac{\Delta\varphi_{(x,y)}}{2}\right) \qquad \textit{eq. 6-6}$$

$$\Delta I_{3(x,y)} = -sin\left(\phi_{0(x,y)} + \frac{\Delta\varphi_{(x,y)}}{2}\right) sin\left(\frac{\Delta\varphi_{(x,y)}}{2}\right) \qquad \textit{eq. 6-7}$$

$$\Delta I_{4(x,y)} = -cos\left(\phi_{0(x,y)} + \frac{\Delta\varphi_{(x,y)}}{2}\right) sin\left(\frac{\Delta\varphi_{(x,y)}}{2}\right) \qquad \textit{eq. 6-8}$$

As we can see, all the above 4 subtraction images can be expressed by multiplication of two parts. First one is sine or cosine function of the sum: $\phi_{0(x,y)} + \frac{\Delta\varphi_{(x,y)}}{2}$; second one is a common term $sin\left(\frac{\Delta\varphi_{(x,y)}}{2}\right)$ shared by eq. 6-5 to eq. 6-8. The first part is depended on intrinsic-phase $\phi_{0(x,y)}$, while the second part is independent on intrinsic-phase $\phi_{0(x,y)}$. Here we take the square sum of these 4 subtraction images (as shown in **Fig. 6-4**):

$$\sigma_{(x,y)}{}^2 = \Delta I_{1(x,y)}{}^2 + \Delta I_{2(x,y)}{}^2 + \Delta I_{3(x,y)}{}^2 + \Delta I_{4(x,y)}{}^2 \qquad \textit{eq. 6-9}$$

We have,

$$\sigma_{(x,y)}{}^2 =$$

$$2\left[sin^2\left(\phi_{0(x,y)} + \frac{\Delta\varphi_{(x,y)}}{2}\right) + cos^2\left(\phi_{0(x,y)} + \frac{\Delta\varphi_{(x,y)}}{2}\right)\right] sin^2\left(\frac{\Delta\varphi_{(x,y)}}{2}\right) \qquad \textit{eq. 6-10}$$

Using the relation: $sin^2(\alpha) + cos^2(\alpha) = 1$, one can easily cancel out the dependence of intrinsic-phase $\phi_{0(x,y)}$ and obtain:

$$\sigma_{(x,y)}{}^2 = 2sin^2\left(\frac{\Delta\varphi_{(x,y)}}{2}\right) \qquad \textit{eq. 6-11}$$

Here ${\sigma_{(x,y)}}^2$ denoted the square sum of 4 subtraction images. We take the square root from both sides:

$$\sigma_{(x,y)} = \sqrt{2}\left|sin\frac{\Delta\varphi_{(x,y)}}{2}\right| \qquad eq.\ 6\text{-}12$$

Because the cancelation carried out in eq. 6-11, the resulting $\sigma_{(x,y)}$ in eq. 6-12 is independent of the intrinsic-phase image $\phi_{0(x,y)}$.

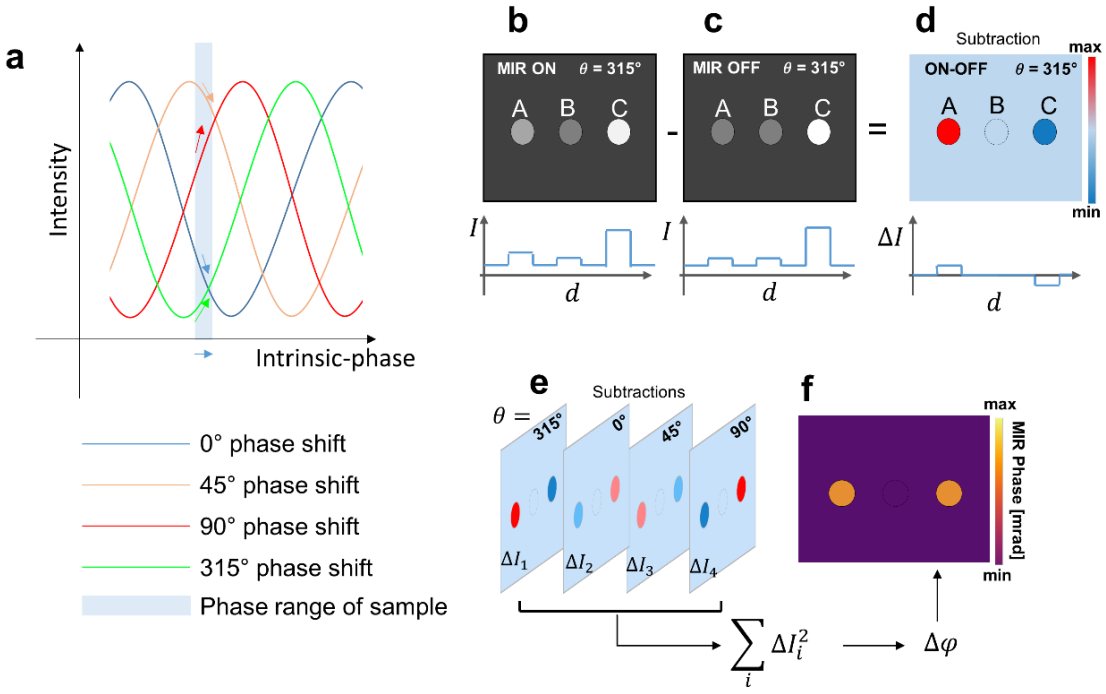

Fig. 6-4. Demonstration of a PSOM image acquisition. a, 4 shifted phase-intensity relations. The arrows indicate the change of intensity caused by MIR absorption. **b-d**, MIR-ON and MIR-OFF intensity subtraction (analyzer angle: 315°), with profiles crossing the three objects in the FOV. Object A: absorption target; Object B: non-absorption target; Object C: absorption target at high dynamic range. **e,f,** Illustration of the square sum for a PSOM image. PSOM image (f) shows quantitative MIR phase regardless of the dynamic phase range of the sample (*86*).

With phase-shifting mechanism, it is worth noting that even if the intrinsic-phase of the sample is wrapped, we do not need to perform any phase unwrapping method. While the phase unwrapping method is error-prone and may introduce error larger than the MIR-phase, which is very small. Large phase range, and complicated phase wrapping usually arises from the image of large cells population, especially when cells aggregate, stack, and produce large organelles. The method describe here detects MIR-phase independent of the intrinsic-phase, which makes it able to distinguish the small MIR-phase among a large intrinsic-phase background. Consider the MIR-phase-shift $\Delta\varphi_{(x,y)}$ is very small, we can make the following approximation from eq. 6-12:

$$\sigma_{(x,y)} \approx \left| \frac{\sqrt{2}\Delta\varphi_{(x,y)}}{2} \right| \qquad \textit{eq. 6-13}$$

Note that the approximation is made when intensity image of MIR-ON/OFF were normalized to [1,0]. eq. 6-13 suggests that quantitative MIR-phase $\varphi_{(x,y)}$ can be obtained by multiplying $\sigma_{(x,y)}$ to a factor $\sqrt{2}$.

$$\Delta\varphi_{(x,y)} \approx \left| \sqrt{2}\sigma_{(x,y)} \right| \qquad \textit{eq. 6-14}$$

6.2 Methods

6.2.1 Experimental setup

As shown in **Fig. 6-1**, in the phase-shifting microscope, a green (wavelength: 532 nm) pulse laser (Coblt 06-Tor, HÜBNER GmbH & Co KG, 2k Hz, 2-3 ns pulse width) was used to generate a linear polarized probe beam (polarization: 90°; the angle is defined as clockwise angle around positive semi-axis of x). The output of laser directly traveled through a linear polarizer (LPVISC050-MP2, Thorlabs, Inc., with its transmission axis of 45°) to obtain 45° linear polarized beam (which is a decomposed polarization component on the transmission axis). After the polarizer, the beam entered a birefringent beam displacer (BD27, Thorlabs, Inc.); it was separated into two parallel beams with orthogonal polarization directions: polarization of 0° and 90°, respectively. In the beam displacer, the 90° component (termed reference beam, RB) traveled straightly through the whole beam displacer; while the 0° component (termed sample beam, SB) deviated away from the RB. At output of beam displacer, the two parallel beams were separated by a distance of 2.7 mm, and had the same intensity. Then both RB and SB traveled thought a half-wave plate (WPHSM05-532, Thorlabs, Inc) with fast axis of 45°. Thus, the half-wave plate rotated polarizations of both beams 90° regarding to the fast axis, resulting a 0° polarization RB and 90° polarization SB. Then they traveled through a sample plane where supposed to have sample only on the side of SB. Afterward, they entered a symmetrically placed BD27 (termed beam combiner here), so that the two beams were spatially combined again. When there is sample on the sample plane, the combined beam will be elliptically polarized as discussed and illustrated section 4.2.3. After the beam combiner, the combined beam entered an objective (MY10X-803, Thorlabs, Inc), which had its focus on the sample plane. A quarter-wave plate (WPQSM05-532, Thorlabs, Inc) with fast axis of 45° was placed after the objective to convert the elliptical polarized beam into linear polarized beam. After the quarter-wave plate, the beam traveled through a linear polarizer (LPVISC050-MP2, Thorlabs, Inc, termed analyzer) that mounted on rotational stage, so that the angle of polarizer can be controlled. A tube lens was then used to focus the light to a high-speed camera (Dimax cs4, Excelitas PCO GmbH), forming an image on camera sensor.

The mid-infrared (MIR) pump beam was pulse laser generated from an Optical Parametric Oscillator (OPO) laser (NT277, EKSPLA; 1 kHz pulse repetition rate, 9 ns pulse width). A Germanium window in front of OPO laser was used to filter out the visible "signal" beam generated by means of second-order nonlinear optical interaction within OPO laser. The mid-infrared "idler" beam directly traveled through the Germanium window, and then was focused by a low numerical aperture (NA) gold parabolic mirror (#37248, Edmund Optics Ltd.; NA = 0.062) on the sample. The distance between the parabolic mirror and sample can be adjusted to achieve desirable excitation FOV (ranging from 50×50 μm to 1000×1000 μm).

6.2.2 Synchronization

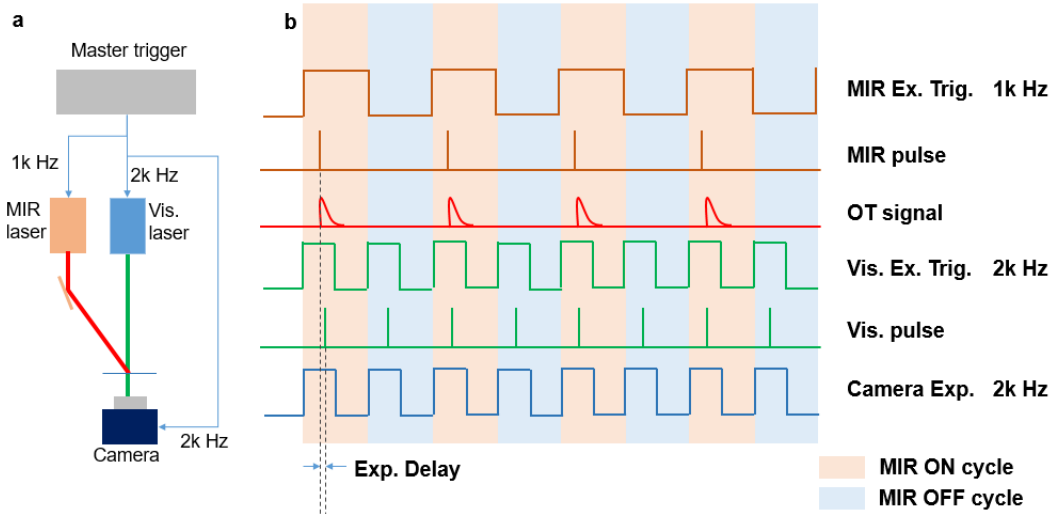

Fig. 6-5. System synchronization. **a**, Diagram of simplified PSOM, emphasizing the synchronization relation and pump-probe mechanism. **b,** Diagram of the trigger pulse trains and its corresponding MIR/Vis pulse output, and optothermal (OT) signal. MIR Ex. Trig.: MIR external trigger. VIS Ex. Trig.: visible external trigger. The three synchronized trigger signals (MIR Ex. Trig., VIS Ex. Trig. and Camera Exp.) are generated by a master trigger, where the MIR Ex. Trig. is a 1k square pulse trains, both VIS Ex. Trig. and Camera Exp. are 2k Hz square pulse trains.

As shown in **Fig. 6-5**, a programmable master trigger generator (Texas Instruments, MSP430F5529 LaunchPad) was connected to MIR laser, VIS laser and high-speed camera to synchronize the pump-probe detection. A 1 kHz pulse trains trigger was generated as external trigger to activate the OPO laser (i.e. MIR laser), resulting in MIR pulse (9 ns pulse width) output at repetition rate of 1 kHz. While a 2 kHz pulse trains was generated as external trigger for VIS laser to produce the 2 kHz VIS pulse (2-3 ns pulse width). The exposure of the camera was controlled by another 2 kHz trigger pulse to synchronize the camera exposure with VIS pulse. Since the trigger frequency of VIS laser and camera was twice of the trigger frequency of OPO laser, the three trigger signals could be configured in a way that half of the images captured at the time of MIR pulse illuminating the sample (served as MIR-ON images), and half of the images captured between two MIR pulses (served as MIR-OFF images). Besides, a delay

(Exposure delay, Exp. Delay) was introduced to MIR external trigger and VIS external trigger so that varying this exposure delay obtained the time dependent optothermal transient signal (will be discussed in **Fig. 6-14** and **Fig. 6-20**).

6.2.3 Sample preparation and sample holding

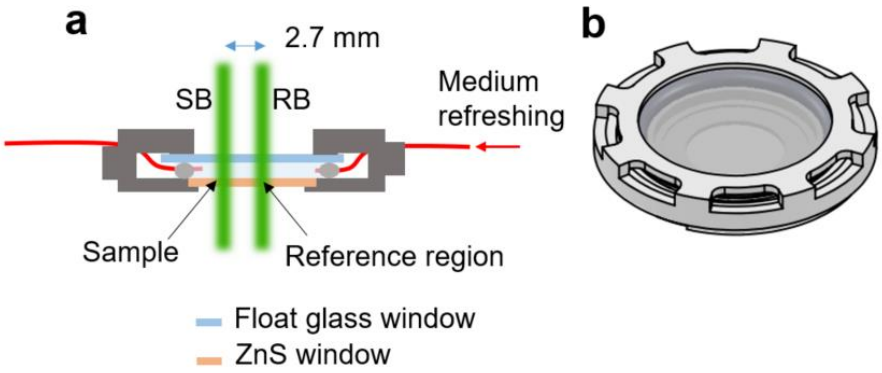

Fig. 6-6. Custom-made petri-dish. a, Cross section of the dish. The sample beam (SB) travels through the region with sample, while the reference beam (RB) travels through a clean region without sample. **b,** 3D illustration of the custom-made petri-dish (*86*).

To minimize the optical perturbation from the environment, an enclosed custom-made petri-dish was designed for containing the sample, as shown in **Fig. 6-6**. The bottom of the dish was made of ZnS window, for penetration of MIR light from bottom, and the top was a cover glass for protecting water evaporation, and for minimizing optical path difference introduced by environment vibration. A reference region without sample was intentionally created for the reference beam passing through. In the TAG drops measurements, the dish was perfused with deionized water, maintaining 3 mm thick water that covered the TAG drops. In the living cells measurements, the dish was perfused with culture medium, and can be refreshed by two circulation tubes go into the dish.

For charactering the system and proof the imaging concept, the TAG drops were were prepared in the same way as described in **section 5.1**. While for the living cells measurement, the cells were prepared as follow: the pre-adipocytes (3T3-L1, ATCC: CRL-1658) were plated in the custom-made petri-dish (**Fig. 6-6**) and cultured in growth medium - low glucose (1g l-1) DMEM (Merck) supplemented with 10% FBS (Merck), and 1% penicillin-streptomycin (Merck). Once 100% confluence was reached, the cells were differentiated to adipocytes. For this purpose, a differentiation medium, composed of high glucose (4.5 g l-1) DMEM (Merck), 10% FBS, 1% penicillin-streptomycin, 1µg ml-1 insulin (Sigma-Aldrich), 0.25 µM dexamethasone (Sigma-Aldrich), 0.5mM 3-isobutyl-1-methylxanthine (Sigma-Aldrich) and 1/1000 volume ABP (50 mg ml-1 L-ascorbate, 1mM biotin, 17 mM pantothenate (Sigma-Aldrich)) was added to the cells on day 0 and day 2. On day 4, the cells were cultured with differentiation medium supplemented only with 1µg ml-1 insulin and 1/1000 volume ABP. On day 6, the differentiation medium was changed back to growth medium (low glucose). Cells were kept in an incubator at 37°C with 5%

CO2 and measured by PSOM while the cells were in growth medium (low glucose). A cell-free region for the reference beam (RB) was created by covering half of dish with a medical grade tape (ARcare 90445Q, Adhesives Research, Inc.), which was removed during PSOM measurement.

6.3 Proof-of-concept measurement

The PSOM image acquisition concept in **Fig. 6-4**b-f can be firstly validated by intentionally manipulating the phase on the object plane, which can be achieved by translating a phase target with a thin indium tin oxide (ITO) layer covered (**Fig. 6-7**). To mimic the phase change induced by MIR absorption, the phase target was translated so that the ITO layer occupies half of the FOV, and a PSM intensity image captured in this situation is considered as a "MIR-ON" image (**Fig. 6-7**a). Another PSM image was captured after the ITO layer was moved away for mimicking a "MIR-OFF" image (**Fig. 6-7**b). An intensity subtraction

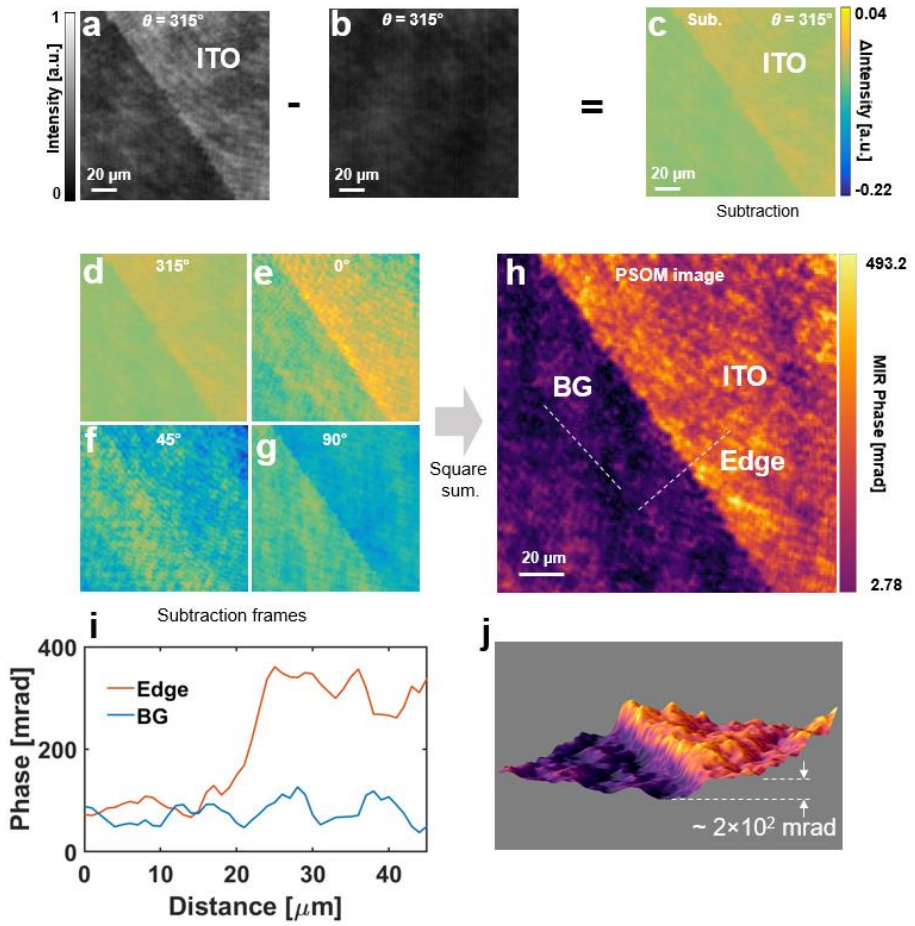

Fig. 6-7. Proof-of-concept measurement of PSOM using an ITO phase target. a, A PSM intensity image (at 315°) with half of the FOV covered by a ITO layer, mimicking MIR-ON. **b,** A PSM intensity image (at 315°) after the ITO layer was removed out of the FOV, mimicking MIR-OFF. **c**, A intensity subtraction image. (Fig. a minus Fig. b). **d-g,** 4 subtraction images from analyzer angles 315°, 0°, 45°, 90°, respectively. **h,** A PSOM image obtained from (d-g), yields quantitative phase that relate to the manipulated phase change by removing out the ITO. **i,** Line profiles crossing the background (BG) and edge of the ITO layer. **j,** 3D surface plot of the ITO layer.

image can be obtained by subtraction **Fig. 6-7**b from **Fig. 6-7**a, as shown in **Fig. 6-7**c. The same procedure was repeated 4 times at 4 different analyzer angle: 315°, 0°, 45°, 90°, obtaining 4 subtraction images as illustrated in **Fig. 6-7**d-g. A quantitative phase image relates to the phase change can be obtained using eq. 6-14, as shown in **Fig. 6-7**h. The phase difference caused by the ITO layer is measured as around 200 mrad, as shown in **Fig. 6-7**i,j.

To further validate the imaging concept of PSOM, the TAG drops (in water) were prepared on our custom-made dish (**Fig. 6-6**), and were measured under MIR excitation (at absorption wavenumber of TAG: 2850 cm^{-1}). **Fig. 6-8**a and **Fig. 6-8**b show a MIR-ON image and a MIR-OFF image respectively, acquired at analyzer angle of 315°. **Fig. 6-8**c depicts a subtraction image, illustrating the intensity difference of TAG drops caused by MIR absorption. Since the phase-intensity relation given in **eq. 4-28** is sinusoidal relation, the intensity difference value of the TAG drops can be positive, or negative, or zero, depending on the intrinsic-phase of TAG drops (as discussed in **Fig. 6-2**). As the phase-shifting mechanism applied (**Fig. 6-8**d-h), quantitative MIR-phase (phase induced by MIR absorption) map is obtained (**Fig. 6-8**h), with the phase range of 0 – 15 mrad, which is 3 order of magnitude smaller than the intrinsic-phase of cells *(54)*.

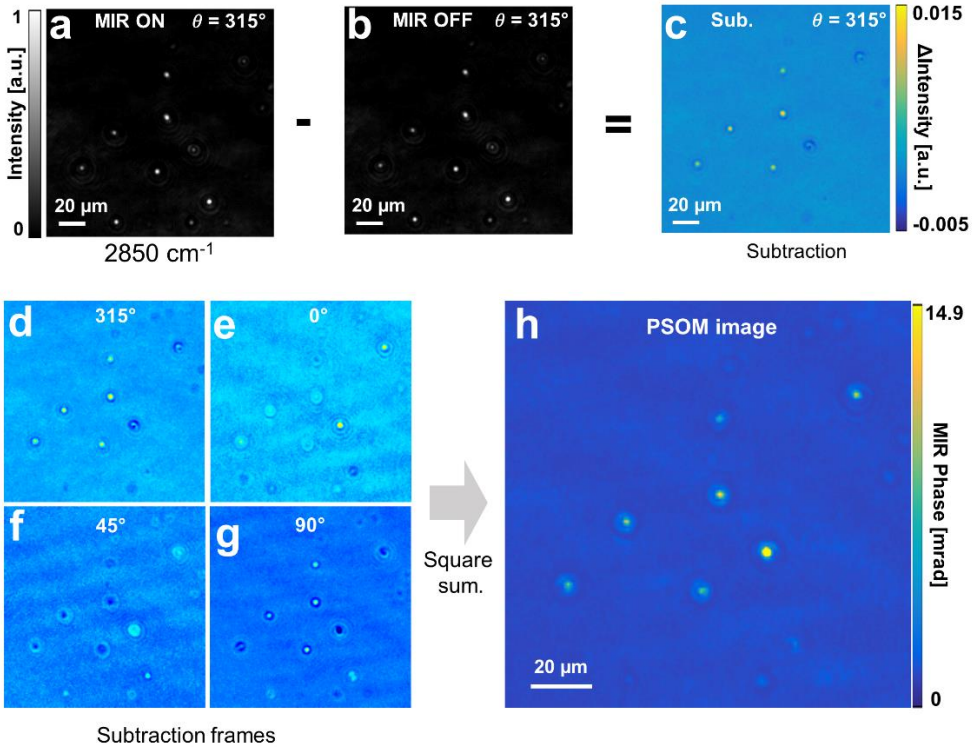

Fig. 6-8. **Proof-of-concept measurement of PSOM using TAG drops. a-c,** Intensity subtractions of TAG drops images, at analyzer angle of 315°. **d-g**, 4 subtraction images from analyzer angles 315°, 0°, 45°, 90°, respectively. **h,** A PSOM image obtained from (d-g), yields quantitative phase that relate to the MIR absorption at 2850 cm^{-1}.

Next, we validate the hyperspectral imaging capability that benefits from the linear relation between MIR-phase and absorption coefficient, formulated by **eq. 3-6**. For this purpose, MIR wavenumber was changing from 2960 cm^{-1} to 2800 cm^{-1}, with step of 4 cm^{-1}. **Fig. 6-9**a depicts partial of the PSOM image along the wavenumber axis (17 out of 41 images). It is observed that the imaging contrast of TAG drops is enhanced around 2850 cm^{-1} (MIR-phase: 52.8 mrad) and 2920 cm^{-1} (MIR-phase 72.7 mrad), due to the strong absorption of MIR light around this two wavenumbers (Corresponding to the CH_2 asymmetry stretch vibration and CH_2 symmetry stretch vibration, similar as observed in **Fig. 5-13**). Once the hyperspectral imaging stack is acquired, the spectrum of TAG drops can be extracted from the imaging stack. For further validation, **Fig. 6-9**b plots spectra of TAG (the location indicated in **Fig. 6-9**a) extracted from PSOM hyperspectral imaging stack, and compared with the TAG spectrum obtain from FTIR. Both spectra are characterized by absorption peaks near 2920 and 2850 cm^{-1}.

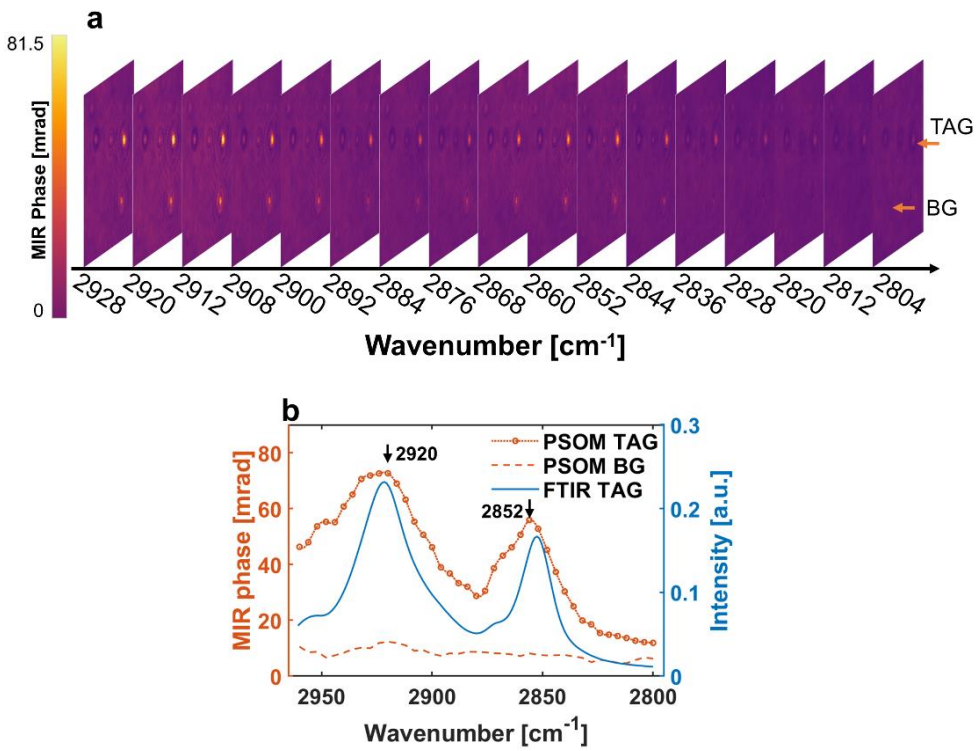

Fig. 6-9. Proof-of-concept for hyperspectral imaging. a, Hyperspectral imaging stack acquired by varying the excitation wavenumber from 2960 cm^{-1} to 2800 cm^{-1} (Only partial of hyperspectral imaging stack is shown due to the space limitation). **b,** Spectrum extracted from hyperspectral imaging stack (marked by "TAG" in Fig. a), compared with TAG spectrum acquired from FTIR.

6.4 Characterization of PSOM

To understand the imaging resolution of PSOM, and characterize the phase noise level, two PSOM images of the same FOV (FOV with TAG drops) were acquired with or without MIR excitation. With MIR excitation at 2850 cm^{-1}, the TAG drops can be observed as shown in **Fig. 6-10**a. Without MIR

excitation, the PSOM obtains a homogenous background that illustrates the noise of the optical system (**Fig. 6-10**b). The standard deviation of the noise is calculated as 0.33 mrad, which is later used for calculating the signal to noise ratio (SNR) or contrast to noise ratio (CNR) (see Appendix B). **Fig. 6-10**c shows a PSM intensity image at analyzer angle of 45°, obtained for purpose of comparing the imaging resolution of pump-probe system (PSOM) and the probe-only system (PSM). **Fig. 6-10**d plots the line profiles crossing a smallest drop found in the FOV. According to the plot of **Fig. 6-10**d, the Full-Width-at-Half-Maximum (FWHM) of the PSOM profile is 2.0 μm, and the FWHM of PSM is 3.1 μm. The smaller FWHM from PSOM may be caused by the fast thermal dissipation around the interface of TAG drop and water, similar result has been observed in ref (*52*).

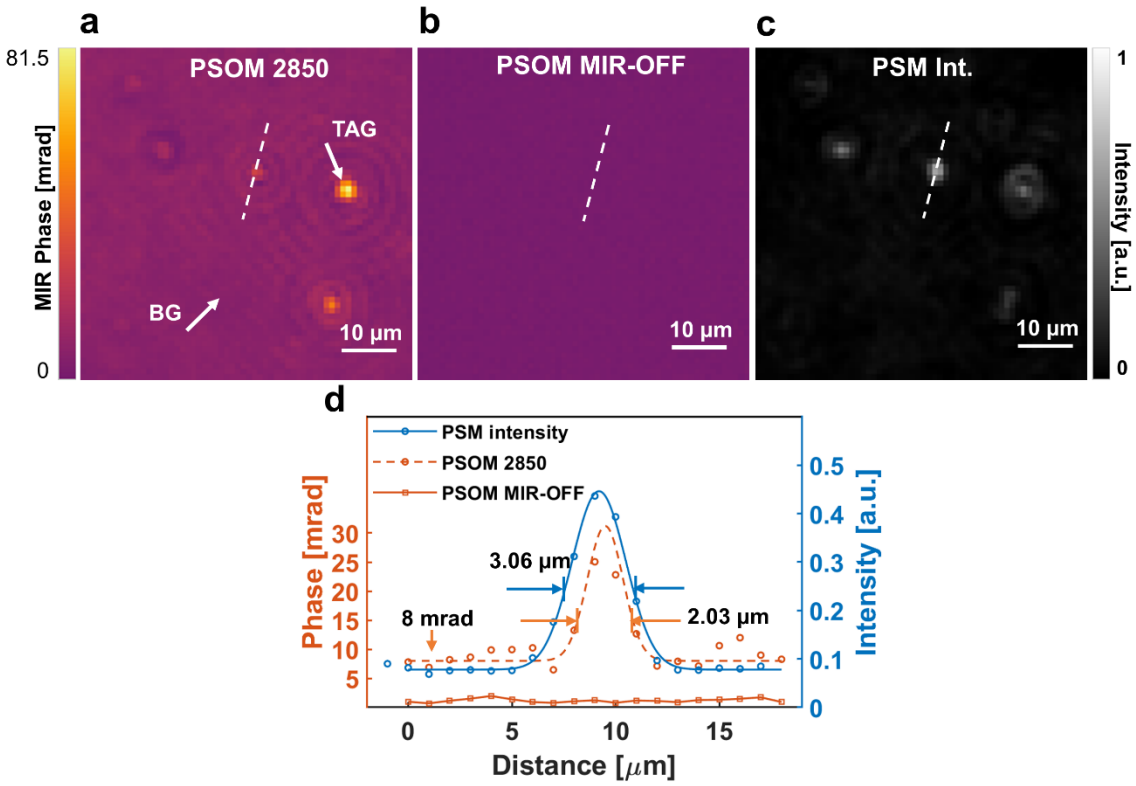

Fig. 6-10. Resolution and shutdown noise characterization of PSOM. **a,** PSOM image of TAG drops, at excitation wavenumber of 2850 cm^{-1}. **b,** PSOM image of the same FOV as (a), but shutdown the MIR laser during the measurement. **c,** A PSM intensity image at the same FOV as (a). d, Line profiles crossing the smallest TAG drop as indicated in (a-c) (*86*).

It is also interesting to understand the temporal noise of the system over time. Since some of our measurements can take few hours, especially monitoring the living cell in a long time. For this purpose, we run the system for 1 hour without MIR excitation and plot the temporal profile, as shown in **Fig. 6-11**. It is observed that during the measurement, the noise remain in a low level around 0.23 mrad to 0.27 mrad, this value is 1/4 of the state of art method (~ 1 mrad) (*53*), and the value corresponding to optical path length of around 0.021 nm.

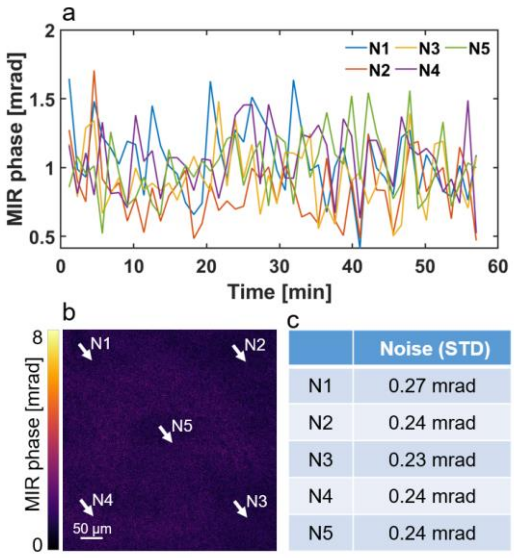

	Noise (STD)
N1	0.27 mrad
N2	0.24 mrad
N3	0.23 mrad
N4	0.24 mrad
N5	0.24 mrad

Fig. 6-11. Characterization of temporal noise of PSOM. **a,** Temporal profiles at 5 different locations of the FOV. **b,** A single MIR shutdown image with the 5 locations indicated. **c,** Standard deviation of the 5 profiles.

To characterize the MIR excitation response of PSOM micrograph, and verify the linear relation given by eq. 3-6, we changed the excitation pulse energy of the MIR light, and acquired PSOM micrographs under different pulse energy. As shown in **Fig. 6-12**a-i, the visibility of TAG drops increasing as the pulse energy increasing. It is observed that the MIR-phase value of a particular TAG drop (marked by an arrow) is linearly related to the pulse energy, as shown in **Fig. 6-12**j. According to eq. 3-6, this linear relation can be written as $\eta E_{\vec{r}} = \Delta\varphi_{(\vec{r},k)}$, where the slope $\eta = \frac{2\pi}{\lambda A}\frac{(l\alpha+nl\beta)}{c\rho}\mu_k$. The spectra extracted from the hyperspectral stack were also found to follow this linear relation as the excitation energy varying, as shown in **Fig. 6-13**. Moreover, it is observed from **Fig. 6-12**j that the MIR-phase of 7.8 mrad (corresponding to SNR of 23.6, which is evaluated by dividing this MIR-phase value by standard deviation of MIR shutdown noise given in **Fig. 6-10**b) is obtained under MIR pulse energy of 11.3 µJ/pulse. Considering the MIR repetition rate of 1 kHz, and its irradiation area of 400×700 µm^2 (elliptical area) (see **Fig. 6-16**), we have excitation power flux density of 0.05 µW/ µm^2, which is 6 orders of magnitude lower than the MIR flux density of Raman scattering microscopy, for instance, excitation flux density of 15 mW/µm^2 for Coherent Anti-Stokes Raman Scattering (CARS) (*85*). The low MIR flux density provides an advantage of reducing photodamage to living cells, which has been observed in Raman scattering base microscopies (*40, 41*). In living cells measurement, to enhance the signal, we use maximum MIR pulse energy of 36.9 µJ/pulse.

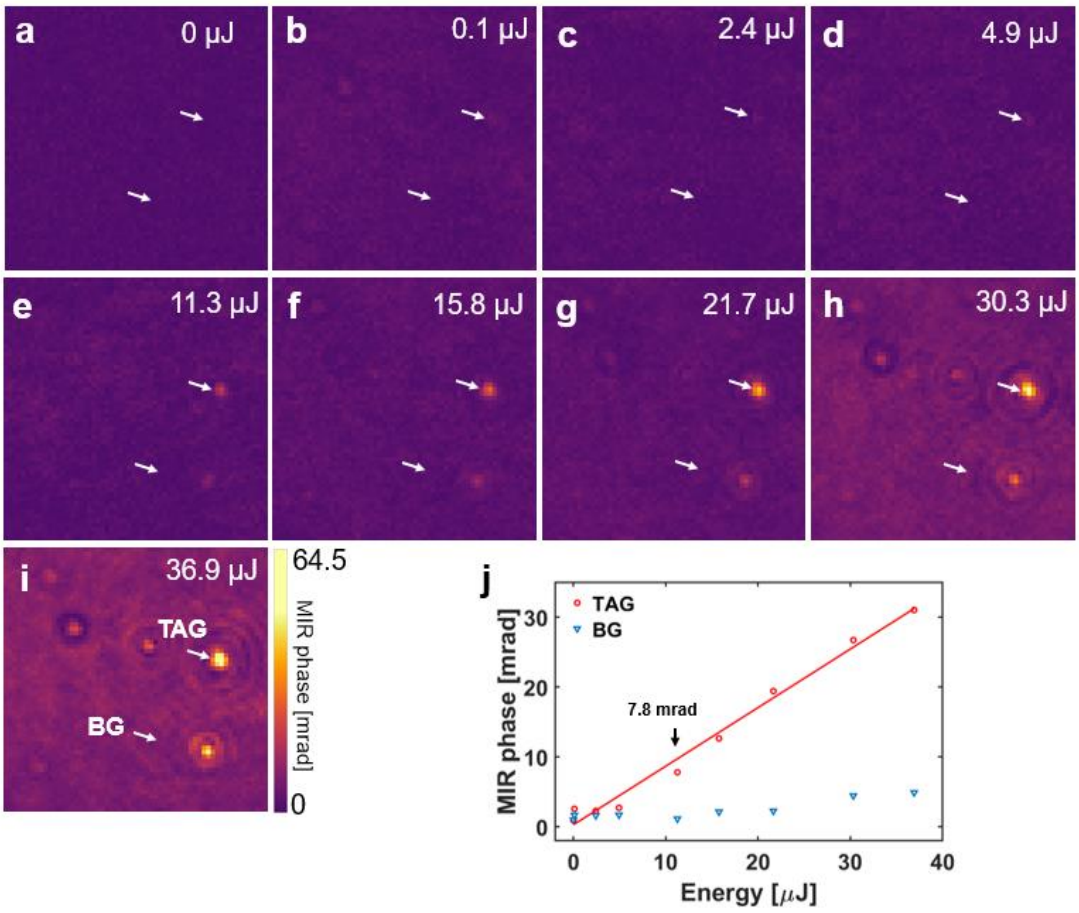

Fig. 6-12. Linear MIR excitation response of PSOM's image. a-i, PSOM images with different MIR pulse energy on the sample, ranging from 0 µJ to 36.9 µJ. **j,** Plot of the MIR phase values at location of TAG and background (BG).

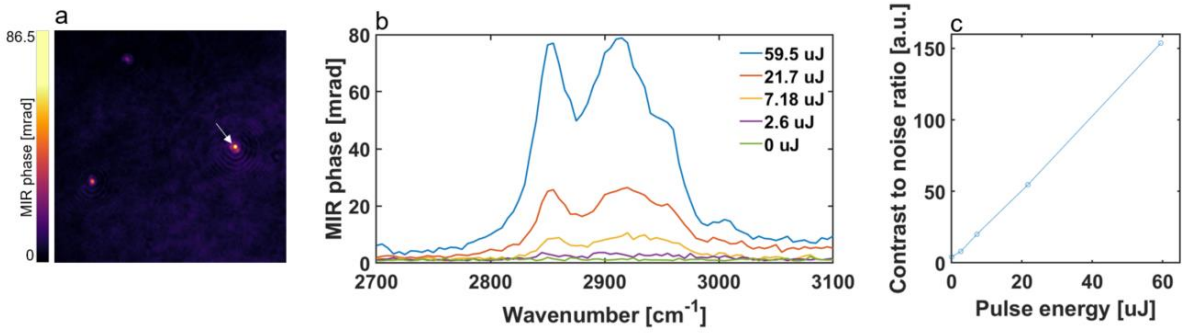

Fig. 6-13 Linear MIR excitation response of PSOM's spectrum. a, Measurement FOV. **b,** Spectra of TAG drop (marked by arrow in a) under different excitation energy. **c**, Plot of contrast to noise ratio at difference pulse energy.

Next, we characterized the time dependent optothermal response of a single MIR pulse, by varying the exposure delay (introduced in the synchronization of method **section 6.2**). **Fig. 6-14** shows the PSOM micrographs of the TAG drops (Same FOV as **Fig. 6-10** and **Fig. 6-12**), as we varying the exposure delay. **Fig. 6-14**a-c depict three micrographs acquired at the exposure time (time = 0 µs) just before the

MIR pulse arrive the sample, at the time of MIR pulse arrive (time = 1.64 µs), and at the time of thermal relaxation (time = 80 µs). **Fig. 6-14**d plots the MIR-phase of a TAG drop (marked by arrow in **Fig. 6-14**b) changing over time, and the exponential fit of the thermal decay. **Fig. 6-14**e illustrates the exposure delay that is changed to achieve single pulse response in this measurement. Here in **Fig. 6-14**d, we observed that the optothermal signal reaches its maximum within 1.64 µs. At the optothermal signal peak, we obtained maximum MIR-phase of 66.42 mrad (corresponding to image of **Fig. 6-14**b), afterward, it exponentially decays with a time constant of 15.44 µs. During the decay process, the heat dissipates into the water, which surrounds the TAG drops and has high specific heat capacity. At the time around 80 µs, the signal is quite close to it's pre-optothermal level that hard to be resolved from the background, which suggests an optothermal cycle of around 80 µs. One can take the advantage of this optothermal cycle to approach PSOM's imaging speed limit. For example, using a MIR pump source with repetition cycle of 80 µs, and designing a corresponding trigger signal for the camera, one can obtain a pair of MIR-ON and MIR-OFF images in 80 µs, and reach the frame rate of 12.5 kHz.

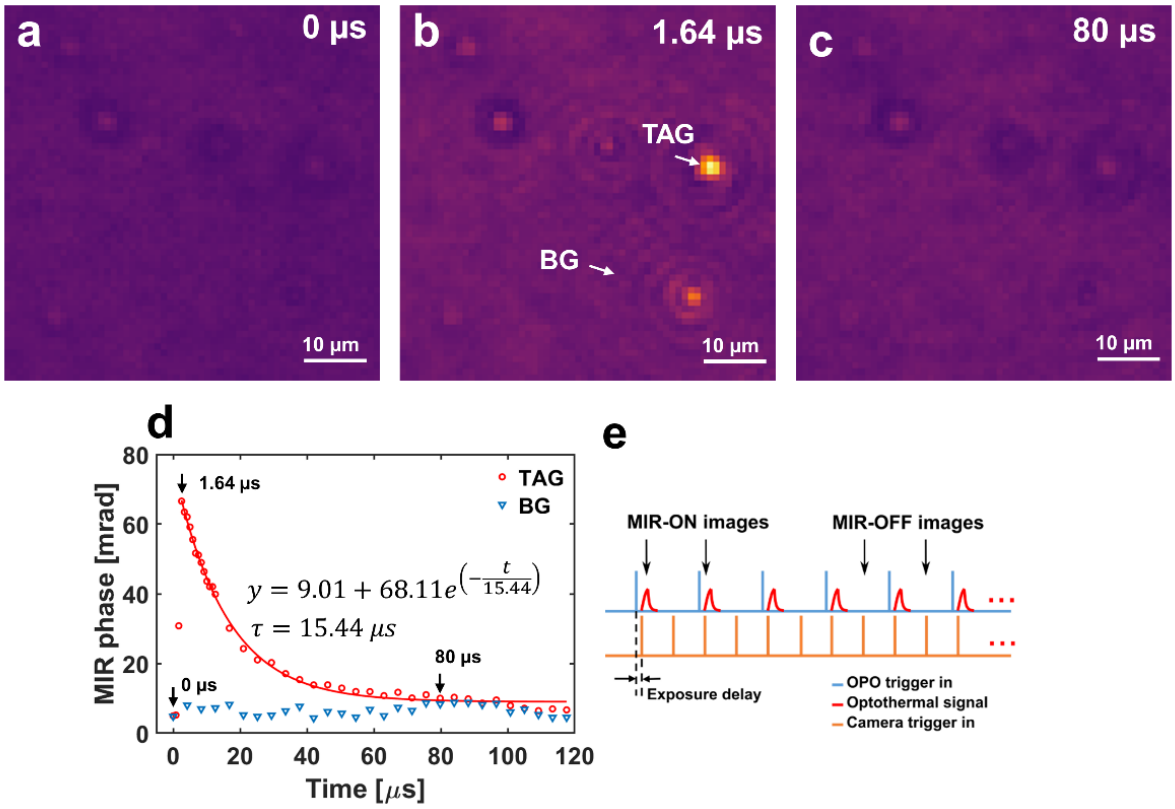

Fig. 6-14. Time dependent optothermal response of single MIR pulse. a-c, PSOM image of the FOV at exposure delay of 0 µs, 1.64 µs and 80 µs. **d,** Plot of MIR phase value from location of TAG and BG as marked in (b). **e,** The trigger pulse train used in this measurement. The single-pulse optothermal signal profile (d) is obtained by varying exposure delay between the two trigger trains (OPO trigger in and camera trigger in) to scan the optothermal signal in time (see Methods **section 6.2**).

6.5 PSOM imaging for living cells

Compared with the focused excitation configurations (see **Fig. 3-1d**), which have been applied in CARS, SRS, MiROM (*37, 62, 87*), MIR power flux density of PSOM is dramatically reduced. This is directly benefits from the expanding of excitation beam from a diffraction limit spot (c.a. 1 μm^2) to the whole imaging FOV (c.a. 500000 μm^2). Low excitation power flux density reduce phototoxic or photodamage to living cells that occurs in focused excitation configuration, for instance, CARS and SRS (*40, 41*). It is observed that cellular structure such as myelin sheath can be tore and split by the plasma induced ablation of the focused spot (*40*). For the other side, the wide field excitation configuration of PSOM provides a high-speed imaging scheme for large FOVs, relaxing the trade-off between large FOV and fast imaging speed in point-by-point scanning scheme. This is because the imaging speed of PSOM does not relay on the scanning speed, instead, it relays on the exposure time of camera as well as the minimum time course of MIR-ON and MIR-OFF image. Exposure time of a commercially available camera can reduce to 1 μs and the minimum time course of MIR-ON and MIR-OFF images can be reduce to a optothermal cycle of around 80 μs (see **Fig. 6-14**).

Firstly, we demonstrate a proof-of-concept measurement of living cells on a small FOV, to verify the single-cell analysis capability of PSOM. As shown in **Fig. 6-15**, three differentiated 3T3-L1 cells (day 6 after differentiation) in a FOV is measured by PSOM. **Fig. 6-15**a-d depict the PSM intensity images (MIR-OFF image) at four analyzer angles: 315°, 0°, 45°, and 90° (intensity has been normalized to 0 - 1). **Fig. 6-15**e,f illustrate a ZPC image and a quantitative intrinsic phase image constructed from **Fig. 6-15**a-d using eq. 4-34 and quality guide phase unwrapping method (*83, 84*). **Fig. 6-15**g-j show the corresponding subtraction images at the four analyzer angles (MIR-ON image obtained at excitation wavenumber of 2850 cm^{-1}). It is worth noting that the maximum intensity change is two order of magnitude smaller than the intensity image (intensity range of subtraction image: -0.015 to 0.024; intensity range of PSM intensity image: 0 to 1). The small intensity change indicates that MIR induced phase change (i.e., MIR-phase) is extremely small compared with the intrinsic-phase. **Fig. 6-15**k shows a PSOM micrograph constructed from **Fig. 6-15**g-j, by applying eq. 6-12. Different from the quantitative intrinsic-phase image **Fig. 6-15**f, the PSOM micrograph here only illustrates high contrast for lipid droplets (due to CH_2's strong vibrational absorption at 2850 cm^{-1}), which's MIR-phase ranging from 0.1 to 31.9 mrad. **Fig. 6-15**l merges the MIR-phase (**Fig. 6-15**k) together with the quantitative intrinsic-phase (**Fig. 6-15**f). It is observed that artifacts occurs in the location of lipid droplets, probably due to strong phase wrapping that failed to recovered using quality guide phase unwrapping method.

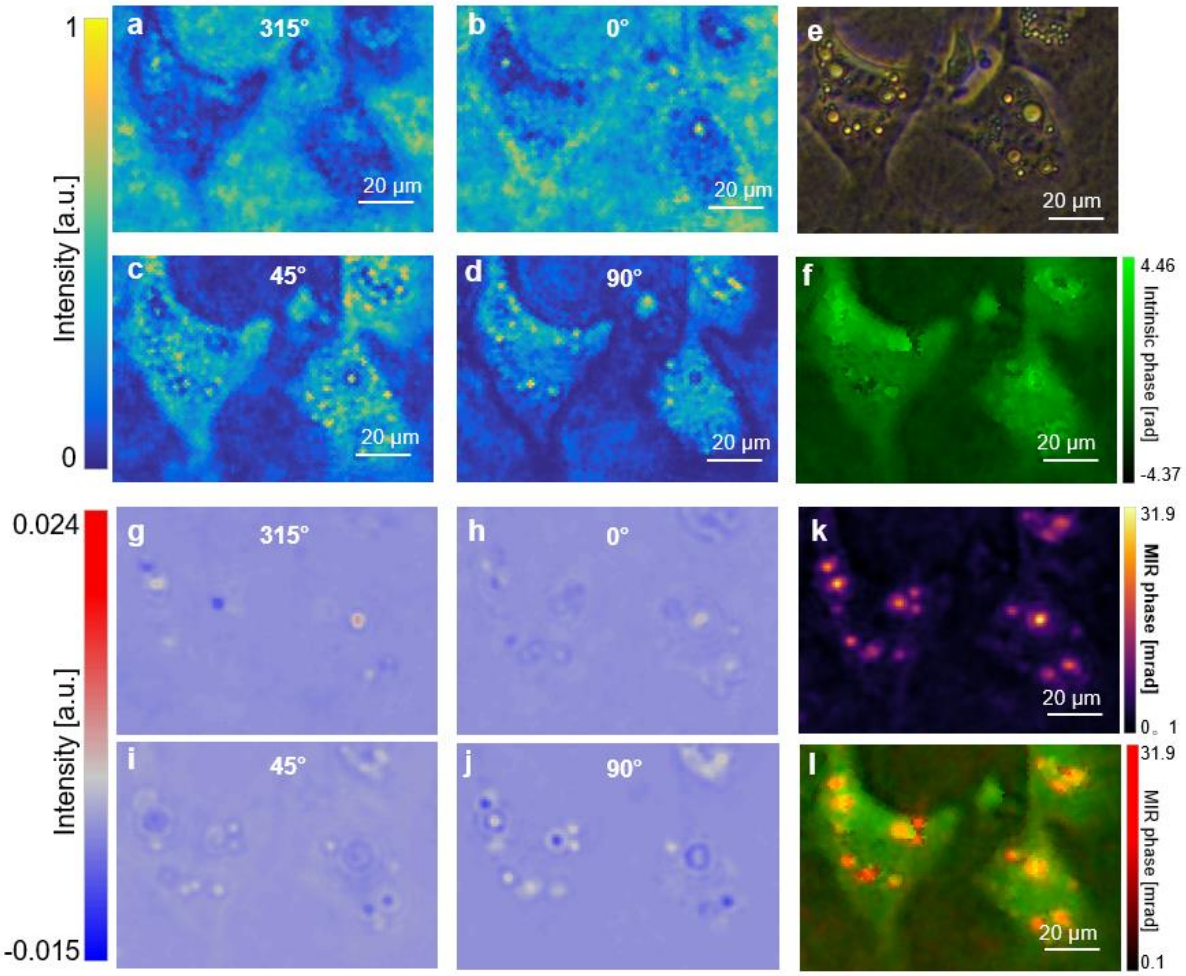

Fig. 6-15. Proof-of-concept measurement of 3T3-L1 cells. a-d, MIR-OFF intensity images (obtained by PSM) of cells at analyzer angle of 315°, 0°, 45°, and 90°. **e**, Image FOV of (a-d) acquired by Zernike's phase contrast microscope. **f**, Quantitative intrinsic-phase reconstructed from (a-d) using eq. 4-34, and applied quality guide phase unwrapping method (*83, 84*). **g-j**, Subtraction images for analyzer angle 315°, 0°, 45°, and 90°. k, PSOM image constructed using eq. 6-14.

Then the other measurement was carried out to verify the large FOV imaging capability of PSOM, as shown in **Fig. 6-16**. A Zernike phase contrast image of the imaging area is depicted in **Fig. 6-16**a, illustrating a FOV fully occupied by 3T3-L1 cells (day 6 after differentiation), i.e., 100% confluency. It is worth noting that acquiring quantitative phase image (QPI) of such a high confluency cells sample is challenging due to the strong scattering, thus challenging the state-of-art QPI based optothermal microscopies, such as bond-selective transient phase (BSTP) microscope (*52*), and molecular vibrational quantitative phase imaging (MV-QPI) (*51*). However, measuring living cells at high confluency is important because many cellular processes are substantially affected by high confluency; for instance, the differentiation of myoblasts into myotubes and the differentiation of preadipocytes into adipocytes (*88*), as demonstrated in this experiment.

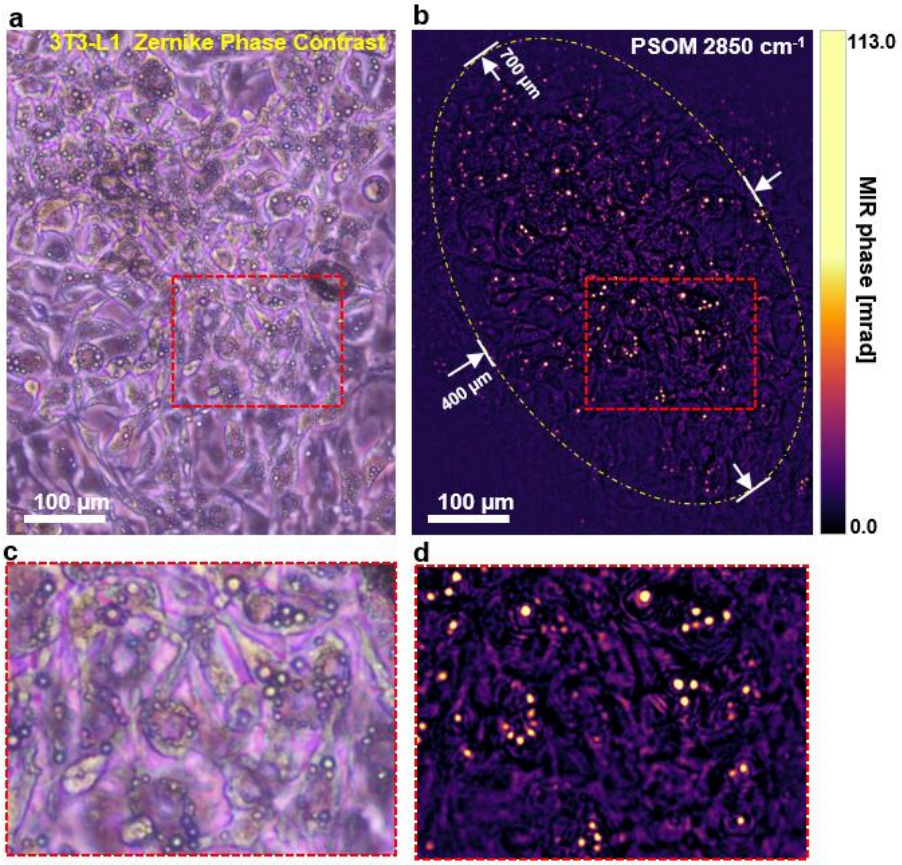

Fig. 6-16. Living cells demonstration of PSOM in large FOV and high confluency. **a,** ZPC image of the imaging FOV. **b,** PSOM micrograph of the same FOV as (a), acquired at MIR excitation wavenumber of 2850 cm^{-1}. **c,d,** Zoom in FOVs of the area marked by red dashed rectangles in (a) and (b) (*86*).

To selectively imaging the lipid droplets of the cells, we tune the PSOM excitation wavenumber to 2850 cm^{-1} (CH_2 streching vibration wavenumber), acquire a PSOM micrograph as shown in **Fig. 6-16**b. As indicated by the white dashed line, the MIR illumination area is an ellipse with major axis of 700 µm, and minor axis of 400 µm, given an effective chemical-contrast FOV with area of 2.2×10^5 μm^2. For the first time, such a large living cells imaging area at 100% confluency is achieved by mid-infrared optothermal/photothermal microscopy. **Fig. 6-16**c and **Fig. 6-16**d depict two zoomed-in FOVs of the red dashed area marked in **Fig. 6-16**a and **Fig. 6-16**b, for comparing the two micrographs. Without chemical contrast, the lipid droplet in ZPC micrograph can only be recognized according to its morphology, which is hard to be distinguish from the strong background that originated from all other content of the cell body. This confusing background make lipid droplets hard to be segmented for automated quantitative analyzed. In **Fig. 6-16**d, this background is effectively suppressed (benefits from the intrinsic-phase cancelation carried out by eq. 6-10), and the dominated imaging contrast is provided by CH_2 stretching vibration (mainly from lipid droplets). Furthermore, it is observed that compared with the low cells confluency measurement in **Fig. 6-15**, where the cells do not tightly adhere to one another, the MIR-

phase of lipid droplets in **Fig. 6-16**b reaches up to 113.0 mrad (CNR = 318:1). This high value is probably caused by more efficient lipogenesis under higher confluency of 100%.

To examine the intrinsic phase wrapping under different confluencies, a comparison is carried out in **Fig. 6-17**. As we can observed from day 2 (after differentiation) to day 6 (**Fig. 6-17**a-c), the cells occupy more and more space, and contact more and more with each other. The phase wrapping can be observed in all cases from day 2 to day 6, but are severe in day 6 (**Fig. 6-17**d-f). The strong phase wrapping observed in day 6 is mainly caused by the thick cells and large lipid droplets, and the corresponding QPI is failed to be reconstructed by quality guide phase unwrapping method (*83, 84*) due to severe phase wrapping (**Fig. 6-17**g-i). PSOM circumvents this phase reconstruct problem by acquiring native MIR-phase image—i.e., independently of intrinsic-phase.

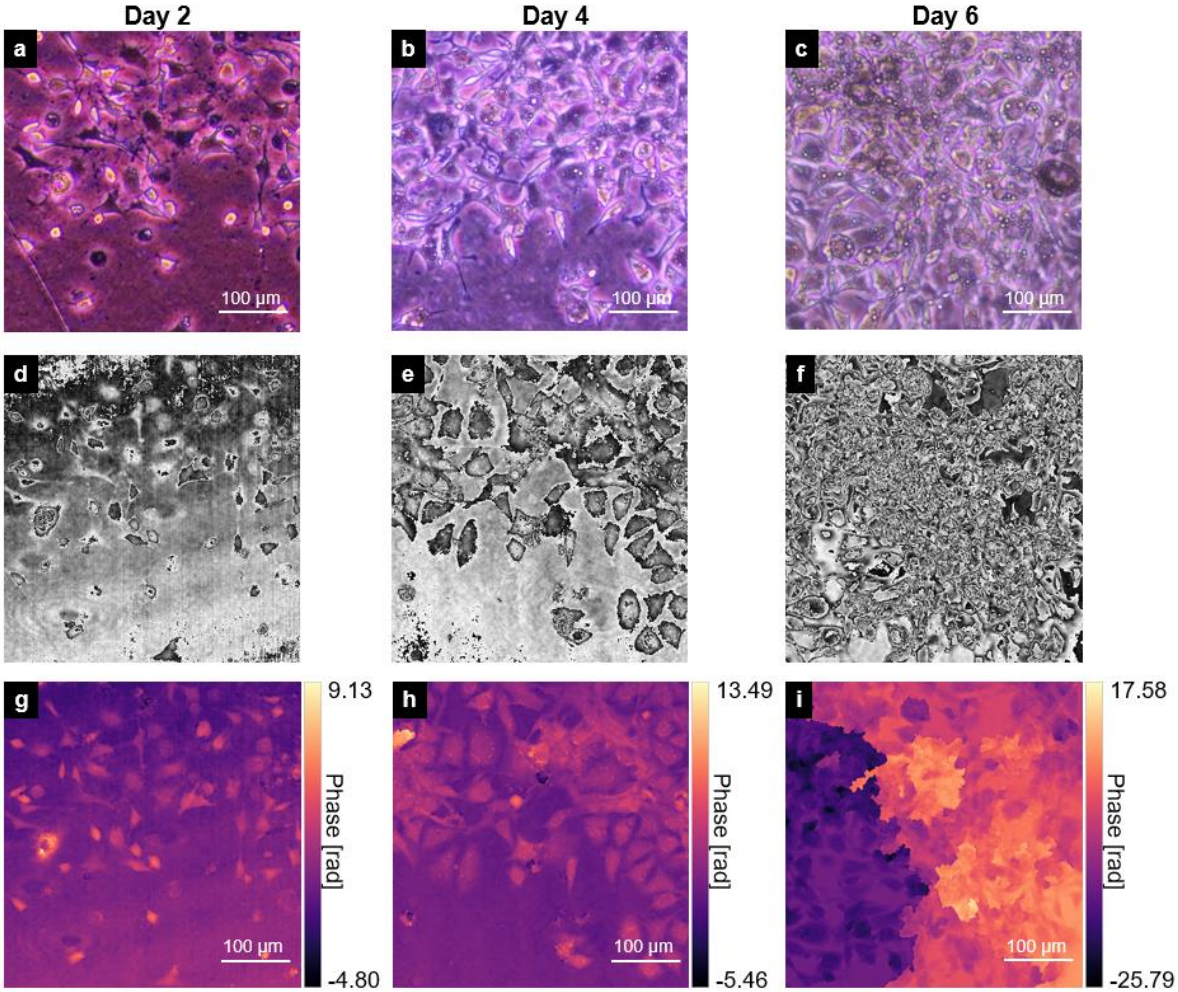

Fig. 6-17. Zernike's phase contrast and quantitative phase contrast (intrinsic-phase) of 3T3-L1 cells at different day (day 2, day 4, and day 6) after differentiation. a-c, ZPC micrographs. **d-f,** Wrapped phase for the corresponding FOVs. **g-i,** Phase unwrapping using Quality Guide method (*83, 84*). At high confluence (i), due to strong scattering of thick cells, the phase unwrapping method failed.

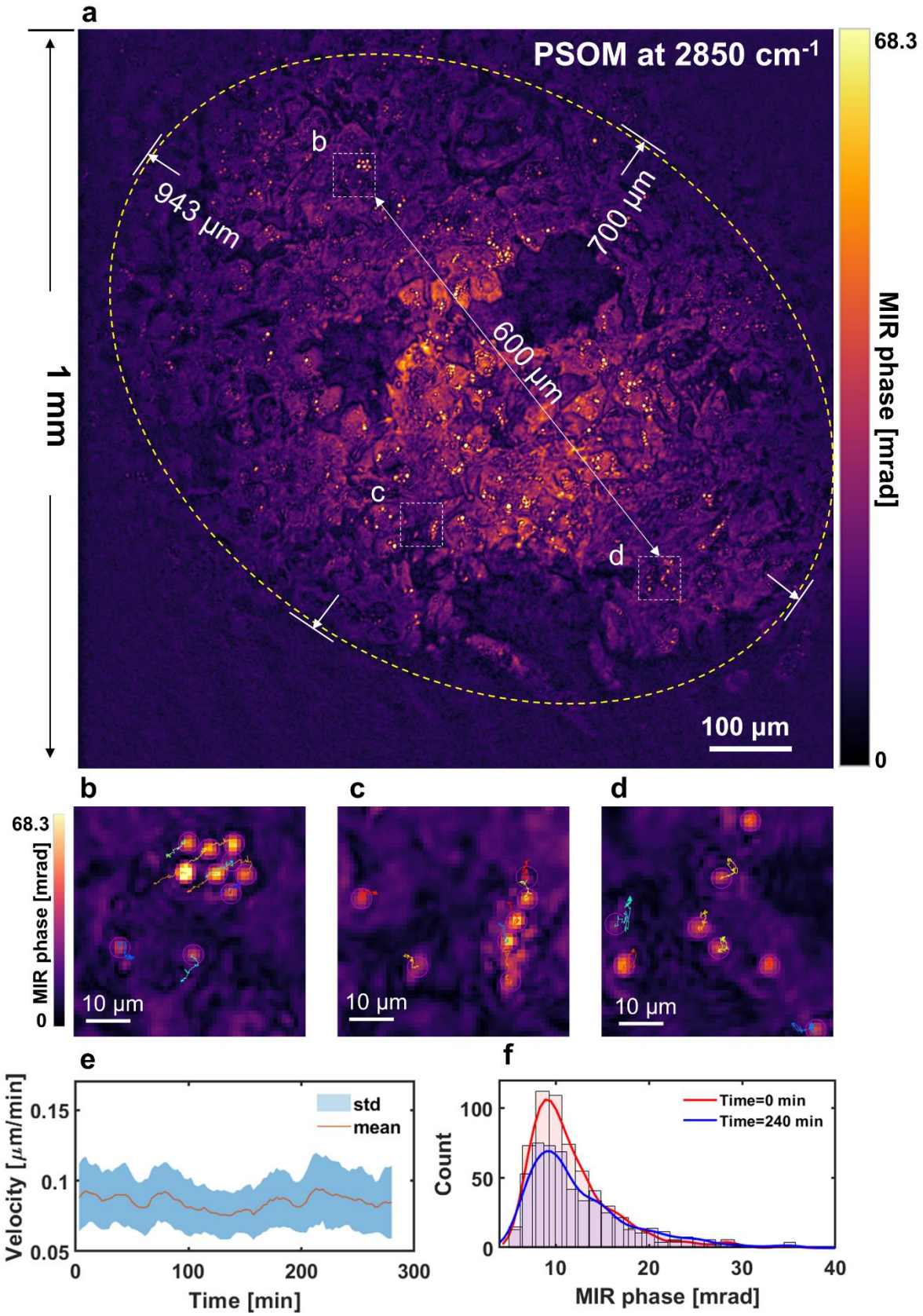

Fig. 6-18. FOV expanding and lipid droplets dynamic monitoring. a, Illustration of an expending FOV (major axis: 934 μm; minor axis: 700 μm). **b-d**, Three zoom in FOVs with automated tracing paths of lipid droplets. **e**, Plot of velocity of tracked lipid droplets in the FOV during the dynamic monitor of 4 h. **f**, Statistic analysis of lipid droplets in the first frame and last frame of the dynamic monitoring measurement.

Next, we demonstrate that larger FOV can be achieve by simply expanding the MIR excitation beam, as shown in **Fig. 6-18**. **Fig. 6-18**a shows a PSOM micrograph (MIR wavenumber 2850 cm^{-1}) with effective FOV of 5.18×10^5 μm^2 (elliptical FOV with major axis of 943 μm and minor axis of 700 μm). Such a large living cells imaging area (5.18×10^5 μm^2) at nearly 100% confluency is unprecedented in optothermal microscopy—c.a. 50 times larger than state-of-art FOV of 1.0×10^4 μm^2 (100×100 μm^2) by computationally stitching 10 frames of 4.0×10^3 μm^2 FOVs (63×63 μm^2) (*89*) and c.a. 20 times larger than the FOVs of 2.5×10^4 μm^2 (180 μm in diameter) obtained by method discussed in **Chapter 5** (*77*).

The capability of large FOV enable PSOM to statistically study large number of cells to minimize the bias in analyzing single cells. Here, using wide-field optothermal microscopy, we are able to demonstrate a (4 hours) dynamic statistical analysis of LDs in such a FOV (5.18×10^5 μm^2) as shown in **Fig. 6-18**a. To study the overall activity over the whole FOV during the observation of 4 hours, all of the LDs' trajectories in the FOV is tracked, and the corresponding velocity is calculated. **Fig. 6-18**b-d depict three areas of the monitoring FOV (as indicated in **Fig. 6-18**a), showing the tracking paths of the LDs in three distant cells. **Fig. 6-18**e plots velocity over time for all of the tracked LDs, and statistic mean and standard deviation. A stable mean velocity (~0.1 μm/min) suggests a stable activity of cells during the measurement time course. **Fig. 6-18**f shows the MIR-phase (maximum value in the automated segmented lipid droplets) histogram of the tracked lipid droplets in the first frame (Time = 0 min) and the last frame (Time = 240 min) of the monitoring. It is observed that the number of lipid droplets with MIR-phase of around 10 mrad dropped down at the last frame compared with the first frame. Moreover, in this experiment, it is worth noting that the observation area of **Fig. 6-18**b is 600 μm away from the area of **Fig. 6-18**d, simultaneous monitoring of such two far area is usually challenge for raster scanning system, but can be achieved by snapshot using PSOM.

In order to investigate how the PSOM micrograph varies with wavenumber and to capture a hyperspectral imaging stack of living cells across a wide field of view, we adjust the excitation wavenumber to selectively excite or not excite specific chemical bonds. **Fig. 6-19**a,b show two PSOM micrographs of 3T3-L1 cells illustrates the CH_2 on-resonance wavenumber 2850 cm^{-1} (the imaging contrast mainly from lipid droplets), and CH_2 off-resonance wavenumber 2700 cm^{-1} (b), without contrast of lipid droplets. By tuning the wavenumber from 2950 to 2700 cm^{-1} (step: 5 cm^{-1}), PSOM is able to obtain spectrum as plotted in **Fig. 6-19**c, where the spectrum is extracted from a selected lipid droplet (marked as "LD" in **Fig. 6-19**a) of a hyperspectral stack (as shown in **Fig. 6-19**d). Similar to the FTIR measurement of TAG (**Fig. 6-19**c), the spectrum extract from lipid droplet is characterized by two absorption peaks near 2920 cm^{-1} and 2850 cm^{-1}, this is because the mainly composition of lipid droplet is variant of TAG, where the molecular structure of TAG contain large number of CH_2 bonds. It is worth noting that for such an imaging stack (consist of 51 images, each image has FOV of 2.5×10^5 μm^2, corresponding to 2.5×10^5 pixels for a single image), the actual acquisition time is around 41 s (Without considering the time consumed by data transferring from camera to PC). For comparison, a point-by-

point scanning vibrational microscopy usually takes hours for a similar hyperspectral imaging stack. For instance, a hyperspectral imaging stack with FOV of 2.25×10^4 pixels took 3.125 h for a confocal Raman microscopy (*90*).

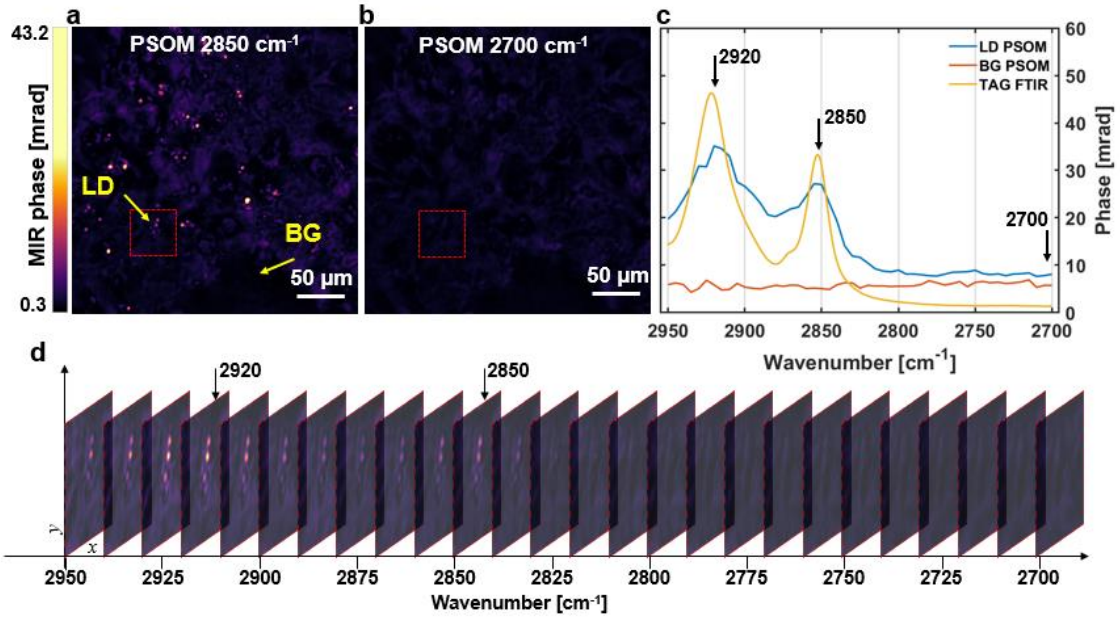

Fig. 6-19. Hyperspectral imaging of living cells by PSOM. a,b, PSOM images of 3T3-L1 cells at lipid specific (CH_2 vibrational contrast) wavenumber 2850 cm^{-1} (a), and lipid unspecific wavenumber of 2700 cm^{-1} (b), respectively. They are two images selected from a hyperspectral imaging stack. **c**, Spectra extracted from hyperspectral imaging stack, showing spectrum of lipid droplet (LD) and spectrum from background (BG), where there is no cell. The fourier-transform infrared spectroscopy (FTIR) measurement of triglyceride (TAG) is plotted together for comparison. **d**, Hyperspectral imaging stack (illustrates 26 images out of a 51 images stack for simplicity) for a selected area marked in rectangles in (a) and (b), illustrating chemical-contrast change of three lipid droplets from wavenumber of 2950 cm^{-1} to 2700 cm^{-1} (*86*).

To understand the how the imaging contrast of living cells evolving after a single MIR pulse illuminate the sample, we continuously varying the exposure delay (See synchronization part of Methods 6.2) in a sequence of 8 measurements (similar to the measurement discussed in **Fig. 6-14**). **Fig. 6-20**a-h show this 8 measurements, starting from exposure time point of 0.31 μs before MIR pulse arrive (**Fig. 6-20**a, n=1) to exposure time point of 0.96 μs after MIR pulse arrive (**Fig. 6-20**h, n=8). In this measurement, the actual arrive time of VIS pulse is recorded by photodetector as plotted in **Fig. 6-20**i, and compared with the MIR pulse arrive time (Here takes MIR trigger as time reference). The MIR-phase of a selective lipid droplet (marked in **Fig. 6-20**e) is plotted in **Fig. 6-20**j for demonstrating the changing of contrast. It is observed that at the beginning of MIR pulse arrive, the large lipid droplets is observable with low contrast (**Fig. 6-20**c). The lipid is clearer and clearer in the following frames (**Fig. 6-20**d-h). In the **Fig. 6-20**e, the cells body starting to show up. To capture both the lipid droplets and the cells body, in our

measurements of living cells, we set the VIS pulse arrive time at 0.96 µs after the MIR-pulse arrive (which is 190.16 µs by taking MIR trigger as reference), as marked by the red arrow in (**Fig. 6-20**j).

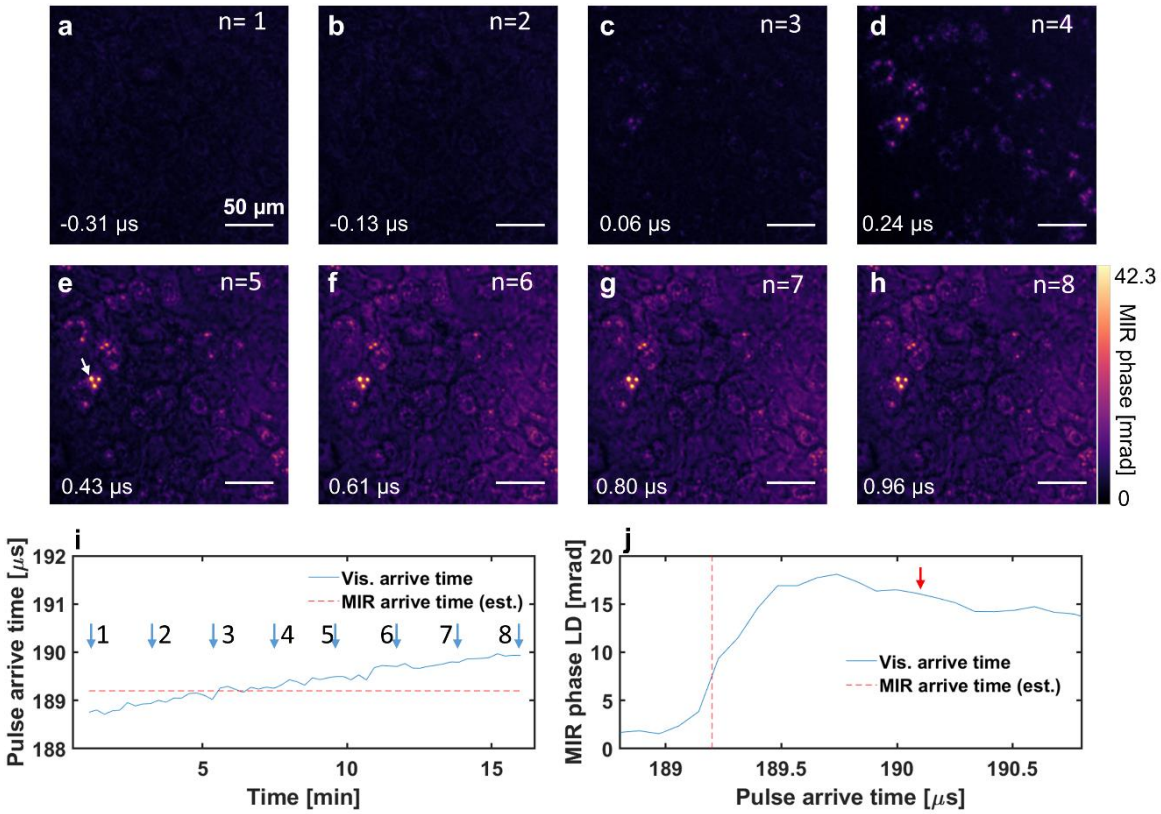

Fig. 6-20. Time dependent of LD contrast from single MIR pulse excitation. a-h, PSOM micrograph at different exposure time points near the MIR pulse arrive time (The time indicated here taking the MIR-arrive time as reference). **i,** Plot of VIS pulse arrive time and MIR pulse arrive time, where the VIS pulse arrive time is consciously changing over the measurement time course for acquiring the time dependent imaging contrast (The time here taking the MIR trigger as time reference. MIR pulse arrive at 189.20 µs as marked by the dashed line). **j,** Plot of MIR-phase of a particular LD (indicated in Fig. e) developing over the VIS arrive time. Red arrow marked the configured VIS pulse arrive time used for living cell hyperspectral imaging.

As we observed in **Fig. 6-20**, the cells' body also illustrate weak contrast from the vibration of CH_2 bonds, probably generates from the cytoplasmic membrane or intracellular membranes, which mainly consist of phospholipid. In order to investigate this weak signal, we performed a measurement on HEK-293 cells and 3T3-L1 fibroblast cells as shown in **Fig. 6-21**. **Fig. 6-21**a,b show a PSOM micrograph, as well as a ZPC image of HEK-293 cells group at the wavenumber of 2850 cm^{-1}. **Fig. 6-21**c shows a line profile crossing the cells group illustrate the MIR-phase of the cells. **Fig. 6-21**d,e depict two micrographs of 3T3-L1 fibroblast cells from PSOM and ZPC microscopy respectively, and **Fig. 6-21**f plots the corresponding line profiles from the cells in PSOM micrograph. In **Fig. 6-21**f, it is observed that the cells' signal is around 2 mrad above the background signal, corresponding to optical path length of 0.17

nm, which is 4.2 % of thickness of a single phospholipid bilayer (~ 4 nm) (*91*). PSOM is able to detect this small optical path difference benefits from the advantage of low shot noise (STD of 0.021 nm, see **Fig. 6-11**).

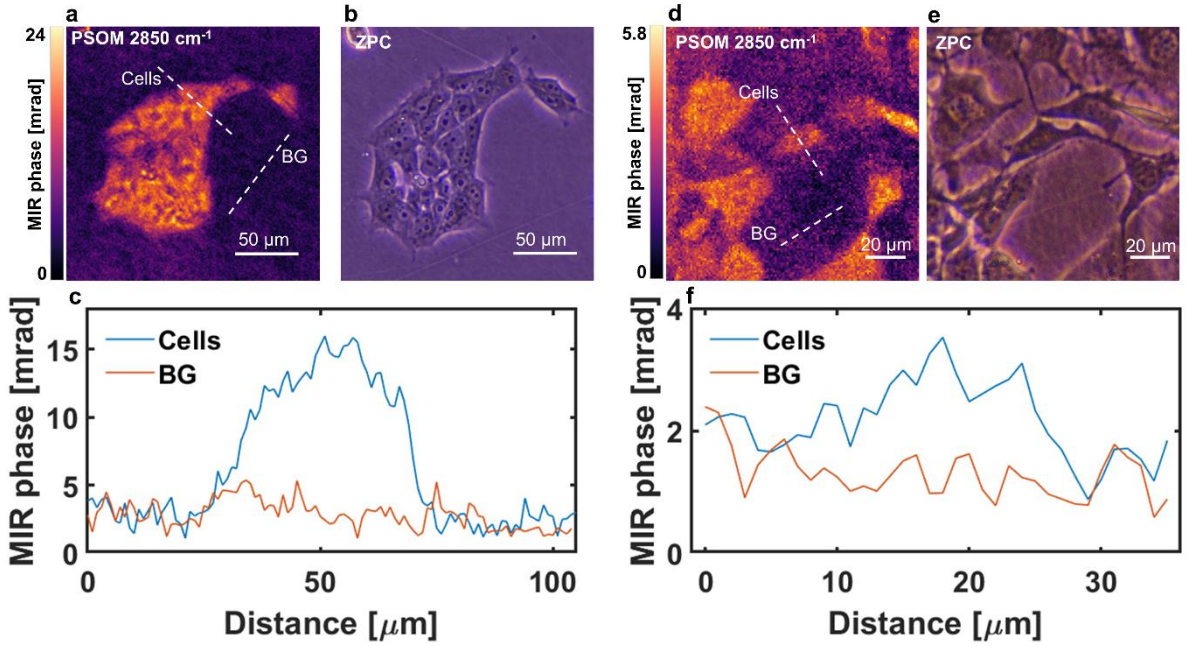

Fig. 6-21. Imaging contrast at 2850 cm^{-1} from cell body. **a,** PSOM image of HEK-293 cells group at mid-IR wavenumber of 2850 cm^{-1}. **b,** The same imaging FOV as (a) by ZPC. **c**, Line profile crossing the cells and background illustrating the MIR-phase range. **d**, PSOM image of 3T3-L1 fibroblast cells, imaging at mid-IR wavenumber of 2850 cm^{-1}. **e,** the same imaging FOV as (e) by ZPC. **f,** Line profile of the cell in the middle.

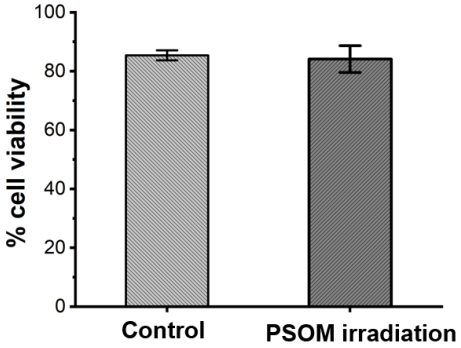

Fig. 6-22. Viability test on HeLa cells under the MIR irradiation of PSOM.

Finally, we illustrate a viability test of living cells to understand the viability of the cells under the illumination of PSOM, as shown in **Fig. 6-22**. In this test the Hela cells were imaged continuously for 2h, and repeated on three different dishes. The control was prepared and maintain in the same condition (room temperature) as the test sample only without MIR irradiation. Each bar in **Fig. 6-22** represents the mean viability value of three different experiments from control and irradiated sample respectively.

The error bars represent the standard deviation of the cell viability of the three measurements. For the irradiated sample, the cells viability is 85.4%, while for the control, it is 83.8%.

6.6 Summary

In this chapter, we moved on to a wide-field optothermal microscopy based on Phase-shifting microscopy. Here, a phase-shifting mechanism under MIR-phase perturbation is presented in section 6.1. In the mathematical deduction from eq. 6-5 to eq. 6-14, we demonstrated that the intrinsic-phase can be canceled out using the phase-shifting mechanism. Later in section 6.2, we introduced the setup of PSOM, and the synchronization of the probe laser, pump laser, and camera. A closed petri-dish was designed for the purpose of holding the sample as shown in **Fig. 6-6**. To proof the imaging concept of PSOM, an ITO measurement and a TAG drop measurement were performed as illustrated in **Fig. 6-7** and **Fig. 6-8**. The hyperspectral imaging capability was validated in **Fig. 6-9** by changing the wavenumber of MIR laser, and the spectrum of TAG from PSOM was verified by the spectrum obtained by FTIR. After carried out the characterization measurements from **Fig. 6-10** to **Fig. 6-14**, we applied PSOM for imaging the living cells. PSOM is not only capable of imaging cells in single cells level as shown in **Fig. 6-15**, it can also be applied to imaging the cells with high confluency (in our case 100 %), where the thick cells and existence of large organelles give a challenge for the other imaging modalities. It is worth noting that our imaging FOV (5.18×10^5 μm^2) can be expanded to 50 times of the state-of-art, and the weak CH_2 vibrational contrast from the cells body (mainly from phospholipid) can be observed. This is benefited from the extremely low shutdown noise (spatial noise: 0.33 mrad, temporal noise: 0.23 to 0.27 mrad) of the PSOM as characterized in **Fig. 6-10** and **Fig. 6-11**.

Chapter 7 Conclusion and outlook

7.1 Conclusion

In this thesis, an wide-field imaging modality was introduced to achieve high-speed, snapshot imaging of the molecular vibrational contrast, based on mid-infrared optothermal effect (mid-infrared absorption induces temperature increase) and thermo-optics effect (temperature change induces refractive index change). Compared with the Raman scattering, mid-infrared absorption cross-sections is 10 orders of magnitude larger (scattering cross-section around 10^{-19} cm^2) (*42*). Taking the advantage of high absorption cross-section, wide-field excitation (excitation area up to 5.18×10^5 μm^2) is implemented instead of focused excitation (excitation area c.a. 1 μm^2), and snapshot (acquisition time 10 ms without considering data transferring time) of the vibrational contrast on a large FOV can be achieved.

To assist the reader in developing a fundamental comprehension of mid-infrared vibrational absorption and the underlying principles of optothermal effect, Chapter 2 briefly reviewed the theory behind the molecular vibration. After the introduction of the fundamental knowledge, in Chapter 3, the pump-probe imaging concept of wide-field mid-infrared optothermal microscopy was introduced. In this pump-probe imaging concept, a MIR pulse laser was used as pump for exciting the vibrational absorption at specific wavenumber, and a phase imaging system was used as probe for detecting the phase change caused by MIR absorption in the sample.

Chapter 4 addressed the need for precise phase change detection by focusing on two custom-made methods - a CF-ZPC microscope and a phase-shifting microscope. In the discussion of CF-ZPC microscope, the underlying principle of ZPC microscope was reviewed, and analytical relations between phase of object and intensity of CF-ZPC image was provided. To introduce phase-shifting microscope (PSM), we began by presenting the polarization phase-shifting interferometer (PSI) and reviewing the Jones calculus. Using the Jones calculus, the mathematical relation between the phase and intensity of PSI was provided. This relation was later validated by imaging ITO phase target and HeLa cells.

Chapter 5 and 6 demonstrated two wide-field optothermal mid-infrared microscopies based on two phase imaging modalities discussed previously in Chapter 4. As a pilot study, Chapter 5 firstly proofed the imaging concept of wide-field microscopy by a MIR-ON and MIR-OFF measurement, and explored the optothermal process. Despite the low sensitivity of CF-ZPC microscope, which precludes imaging of living cells, the investigation of thermal processes in water lays a crucial experimental foundation for comprehending the imaging speed potential of wide-field imaging. In Chapter 6, the wide-field microscopy was implemented by the second phase imaging system – Phase-shifting microscope (PSM). Benefit from its intrinsic-phase cancelation, carried out by eq. 6-5 to eq. 6-11, the MIR-phase shot noise was suppressed to sub mrad (c.a. 0.2-0.3 mrad, see **Fig. 6-10** and **Fig. 6-11**). The low MIR-phase shot

noise allowed the detection of weak signal from organelles of living cells (see **Fig. 6-21**). Moreover, we demonstrated a large FOV up to 5.18×10^5 μm^2 (see **Fig. 6-18**), and imaging of high confluency cells with large organelles.

Comparing with the state-of-art wield-field optothermal/photothermal microscopy, where typical FOVs of 3.1×10^2 to 2.0×10^3 μm^2 (20 to 50 μm in diameter) were achieved, PSOM demonstrated a FOV around 260 times larger. These microscopes typically showed only 1-3 cells or few beads in the FOVs (*50-52*), lacking the ability of statistical analysis. Furthermore, the demonstrated FOVs were characterized by a Gaussian shape artifact, where middle of FOV shows high chemical-contrast and surrounding FOV shows low chemical-contrast. This Gaussian shape artifact was mainly caused by the uneven intensity distribution (2D Gaussian distribution) of excitation beam, and the artifact can be reduced by expanding the excitation area. Although a FOV of 1.0×10^4 μm^2 (100×100 μm^2) has been achieved by computationally stitching 10 frames of 4.0×10^3 μm^2 FOVs (63×63 μm^2) (*89*), the method has the trade-off between larger FOV and fast imaging speed.

In the context of MIR-phase detection, for the first time, we introduced the phase-shifting mechanism for intrinsic-phase cancelation. For comparison, the state-of-art methods extracted the MIR-phase by subtracting a MIR-OFF quantitative phase image (QPI) from MIR-ON QPI image, where the QPI image usually reconstructed from interferograms using postprocessing methods, such as Hilbert transform (*92*), derivative method (*93*), and non-linear phase unwrapping method (*94*). Since the MIR induced phase difference is 2-3 orders of magnitude smaller than the intrinsic-phase, these postprocessing methods on the intrinsic-phase might generate noise that larger or comparable with the MIR-phase, lacking the ability of detecting weak signal. Although the adaptive dynamic range QPI has been developed to bridge the large phase gap between intrinsic-phase and MIR-phase (*53*), the intrinsic-phase dependency haven't been addressed, and probe light is needed for detecting weak signal. PSOM takes the advantage of phase-shifting mechanism to obtain MIR-phase image, and it is capable of measuring MIR-phase independent to the intrinsic-phase. Benefiting from intrinsic-phase indenpendency, PSOM is able to circumvent the need for postprocessing, and measure MIR-phase low noise.

7.2 Outlook

PSOM can assistant the analysis of cells by chemical-contrast imaging, hyperspectral imaging, and long term dynamic motoring. Comparing with Zernike phase contrast microscopy, a ubiquitous label-free imaging technique, PSOM is able to further identify the target structure based on absorption peaks. For instance, as shown in **Fig. 6-16**, the lipid droplets can only be identified according to experience as spherical shape organelles. On PSOM, these spherical shape organelles are further confirmed as lipid droplets since they demonstrate strong absorption in wavenumber of 2850 cm^{-1}, which is the vibration bond of CH_2. Moreover, further chemical-contrast image can be easily obtain by tuning the MIR

wavenumber to the other wavenumbers. For example, protein absorption wavenumber 1550 cm^{-1}, glucose absorption wavenumber 1034 cm^{-1}.

The microscopy examination of the cells can be benefited from hyperspectral imaging (as shown in **Fig. 6-19**), which is imaging stack from a MIR wavenumber range from 2950 cm^{-1} to 2700 cm^{-1}, to further investigate the interesting target from multiple absorption bands. For example, the lipid droplet shown in **Fig. 6-19**a (marked by "LD") was further verified by its second absorption peak from 2925 cm^{-1} (**Fig. 6-19**d), which is another absorption peak from CH_2 vibration. This verification is based on the knowledge that lipid droplets mainly contains triglycerides, which have abundant of CH_2 bonds. Once the hyperspectral imaging stack is acquired, spectrum of every pixel can be extracted from the whole FOV, therefore, spectral analysis can be extended to the whole FOV.

PSOM is a label-free technique that can be used for long term dynamic motoring of organelles. Long term lipid droplets dynamic monitoring has been demanded for understanding the lipid metabolism (*95, 96*). Although fluorescence label has been applied for this study, photobleaching limits the number of images that can acquired in this process (*97*), and using fluorophores run the risk of generating blue-shifted intermediate molecule (*2*). In **Fig. 6-18**, we demonstrate lipid droplets continuous monitoring of 4.5 h without losing the imaging contrast. Using fluorescence labels, this long term, continuous and frequent imaging on the lipid droplets is challenging due to photobleaching.

However, the current setup haven't reach PSOM's maximum imaging speed due to the technical implementations. Firstly, to construct a PSOM image, we averaged 1600 images for a single PSOM image, corresponding to data volume of around 1.2 G. Due to his huge data volume, ~ 1 minute is required for transferring the data from camera to computer, although only 0.8 s is actually needed for capturing the image. To overcome this limitation, one can simply use a camera capable of onboard averaging. By this improvement, images can be averaged on the camera before transferring, thus eliminate the data transferring time. Secondly, the current implementation mechanically rotates the analyzer to acquire PSM intensity images from 4 different analyzer angles. The mechanical rotation slow down the image speed from the other aspect. To address this limitation, a polarization camera can be implemented to avoid the mechanical rotation to instantaneously obtained images from these 4 different angles. Thirdly, to approach the physical speed limit of optothermal microscopy, one can shorten the time interval between MIR-ON and MIR-OFF images. As we demonstrated in **Fig. 6-14**, a optothermal cycle was observed as around 80 μs, while the MIR-ON and MIR-OFF interval in our system is 500 μs (calculated from repetition rate of visible laser and mid-infrared laser, see **Fig. 6-5**). Therefore, one can increase the repetition rate of mid-infrared laser and the visible laser to approach the speed limit.

Moreover, the imaging resolution of the current set up can still be improved. As shown in **Fig. 6-10**, we demonstrated resolution of 2.0 μm, this imaging resolution is limited by the Numerical Aperture (NA = 0.28) of the current objective. Although we achieve a subwavelength resolution in the scope of mid-infrared microscope (2.5 – 12 μm), this imaging resolution is inadequate for imaging smaller cellular organelles. Taking advantage of pump-probe design, where the imaging resolution is determined by the visible optics, one can use a higher NA objective to improve the imaging resolution.

Appendix A

A.1 List of symbols

V	Potential energy
ω	Angular frequency
m	Mass
η	Reduced mass
$\hbar$	Reduced Planck's constant
q_i	Mass weight coordination $q_i = \sqrt{m_i}x_i$.
HO	Higher order terms of expansion
Q_k	Normal coordination k
λ_k	Vibration frequency of the normal mode k
$\Psi_{nk}(Q_k)$	Wave function of a normal mode k at quantum state n
CH_2	Methylene group
CH_3	Methyl group
U	Internal energy
C, c	Thermal capacity, specific capacity
T	Temperature
$\dot{\boldsymbol{q}}$	Heat flux (the rate at which heat is transferred per unit area, per unit time)
ρ	Density
κ	Thermal conductivity constant
α	Thermal diffusivity
$d\tau$	Infinitesimal volume element
σ	Planar density
ZnS	Zinc sulfide
μ	Absorption coefficient
$D(r, \phi, z)$	Energy volume density at cylindrical coordination (r, ϕ, z)
n	Refractive index
δ	Termo-optic coefficient $\delta = \frac{dn}{dT}$
μ_k	Vibrational absorption coefficient at wavenumber k
λ	Wavelength
β	Thermal expansion coefficient
E	Energy
$\Delta\varphi_{(\vec{r},k)}$	MIR-phase image, defined as the phase change caused by MIR absorption

$\overrightarrow{\boldsymbol{E_x}}(z,t)$	Propagating electrical field, at propagation distance *z*, at time *t*
$I_{(x,y)}$	PSM intensity image
$I_{f(x,y)}$	PSM intensity image acquired without MIR illuminating the sample
$I_{n(x,y)}$	PSM intensity image acquired with MIR illuminating the sample
$\phi_{0(x,y)}$	Intrinsic-phase image

A.2 List of abbreviations

MIR-OM	Mid-infrared optothermal microscopy
PSOM	Phase-Shifting Optothermal Microscopy
PSM	Phase-Shifting Microscopy
FOV	Field-Of-View
OPD	Optical Path Difference
mid-IR/MIR	mid-InfraRed
PFD	Power Flux Density
CARS	Coherent Anti-Stokes Raman Scattering
SRS	Stimulated Raman Scattering
SERS	Surface-Enhanced Raman Scattering
MiROM	Mid-infraRed Optoacoustic Microscopy
SNR	signal-to-noise ratio
QPI	Quantitative Phase Imaging
RB	Reference Beam
SB	Sample Beam
TAG	Triglyceride
CNR	Contrast-to-Noise Ratio
FWHM	Full-Width-at-Half-Maximum
BSTP	Bond-Selective Transient Phase
FTIR	Fourier-Transform Infrared spectroscopy
BG	Background
ZPC	Zernike's Phase Contrast
NA	Numerical Aperture
OPO	Optical Parametric Oscillator
LDs	Lipid Droplets
STD	Standard Deviation
ITO	Indium-Tin-Oxide
BFP	Back Focal Plane
CF-ZPC	Condenser-Free Zernike Phase Contrast microscopy
WOMiM	Wide-field Optothermal Mid-infrared Microscopy
PSI	Polarization phase-Shifting Interferometer

A.3 List of figures

A.4 List of tables

Appendix B

B.1 MIR shutdown noise and contrast to noise ratio

The spatial MIR shutdown noise σ_s is defined as the standard deviation of pixels from a PSOM image acquired without MIR laser, calculated by:

$$\sigma_s = \sqrt{\frac{1}{N}\sum_{i}^{N}(\varphi_{s,i} - \mu)} \qquad eq.\,\mathrm{B1}$$

Where, $\varphi_{s,i}$ is the MIR-phase at pixel index i from the PSOM image, and μ is the average of MIR-phase among N pixels of this PSOM image. Eq. B1 can also be used to calculate the temporal MIR shutdown noise, when $\varphi_{s,i}$ is temporal MIR-phase value of a pixel, from a PSOM video with totally N images.

The contrast to noise ratio (CNR) is defined as the MIR-phase difference between the signal and background ($\varphi_{signal} - \varphi_{BG}$) divided by standard deviation of the spatial mid-IR shutdown noise σ_s, which takes the value of 0.33 mrad according to **Fig. 6-10**. CNR is calculated according to:

$$CNR = \frac{\varphi_{signal} - \varphi_{BG}}{\sigma_s} \qquad eq.\,\mathrm{B2}$$

Acknowledgment

Thanks God for giving me the opportunity to meet such a great team here in Munich, and to have support from my family, during my whole journey of studying and the journey of approaching the boundary of the unknown. Without all of the support from people around me, and from family far away in China, I wouldn't be able to start the PhD, let alone finish the PhD. I would like to thank all the people who played an important role for me to reach this point.

I would specially thank Prof. Dr. Miguel A. Pleitez, who hired me, provided me with this exciting project, and trained me the state-of-art knowledge. Not only am I grateful to him for giving me an inspiring project, but I also appreciate the great degree of freedom he granted me during PhD, allowing me to explore and discover the fact of nature, while patiently and tolerantly accepting my mistakes in the learning curve. I would like to thank Prof. Dr. Vasilis Ntziachristos, who provided me with extraordinary resources and a platform for my project, and established such a collaborative and interdisciplinary environment. And also thank Prof. Dr. Ghulam Destgeer for providing all his insightful input in the thesis committee meetings.

I would like to give many thanks to my colleagues in our group. Thanks Francesca Gasparin and Dr. Nasire Uluç, who have been with me for more than four years and who have provided generous assistance on my experiments and on my life in Munich. Thanks to Dr. Yuanhui Huang and Dr. Hailong He, as senior doctoral students from the same graduate school, who provided a lot of advice on my doctoral studies and career planning based on their own experience and knowledge. Thanks to Dr. Lucas Riobo for transferring me his expertise on polarization interferometer, which laid a good foundation for my later work. Thanks to Lidia Seidl, Susanne Stern, and all the administration members of IBMI&CBI, who assisted me with all aspects of administration and organization stuffs related to my CSC scholarship, procurements of experimental equipment, arrangements of thesis committee meeting, and conference attendance, etc.

Finally, I would not be able to reach the starting point of PhD without my lovely families. I want to thank my father Weihua Yuan, who as the core of the poor family, suffered a lot from rising up three children, and thank my mother Zongrong Pang, who offered endless love in my life. Thanks my sister Shihong Yuan and my brother Shiqiang Yuan, for taking care of parents during the last few years and supporting me the PhD study. Thanks all of my uncles and aunts, who finically supported me from my elementary school. Last but not least, I would like to give special thanks to my wife Jinhua Zhang, who came together with me here in Munich, and thank her for the care and patience she gave in my life, and thanks for the encouragement she gave me at my low points of PhD.

Publications

Publications presented in this thesis:

Yuan, T.[#], Pleitez, M. A.[#], Gasparin, F., & Ntziachristos, V. (2021). Wide-Field Mid-Infrared Hyperspectral Imaging by Snapshot Phase Contrast Measurement of Optothermal Excitation. *Analytical Chemistry*, *93*(46), 15323-15330. ([#]Equal contribution)

Yuan, T., Riobo, L., Gasparin, F., Ntziachristos, V., & Pleitez, M. A. (2024). Phase-shifting optothermal microscopy enables live-cell mid-infrared hyperspectral imaging of large cell populations at high confluency. *Science Advances*, 10(8), eadj7944.

Ko, V., Goess, M. C., Scheel-Platz, L., **Yuan, T.,** Chmyrov, A., Jüstel, D., Ruland, J., Ntziachristos, V., Keppler, S.J. and Pleitez, M.A. (2023). Fast histological assessment of adipose tissue inflammation by label-free mid-infrared optoacoustic microscopy. *npj Imaging*, 1(1), 3.

Uluç, N., Glasl, S., Gasparin, F., **Yuan, T.,** He, H., Jüstel, D., Pleitez, M.A., & Ntziachristos, V. (2024). Non-invasive measurements of blood glucose levels by time-gating mid-infrared optoacoustic signals. *Nature Metabolism*, 1-9.

Gasparin, F., Tietje M. R., Katab E., Nurdinova A., **Yuan T.,** Chmyrov A., Ulųc N., Jüstel, D., Bassermann F., Ntziachristos V., and Pleitez, M. A. Protein-structure-sensitive mid-infrared optoacoustic microscopy enables label-free assessment of drug therapy in myeloma cells. *BioRxiv* doi: https://doi.org/10.1101/2024.02.21.581391

Yuan, T., Pleitez, M. A., Ntziachristos, V. Quantitative phase imaging by condenser-free Zernike phase contrast microscope. (Manuscript preparing)

International conference contributions and proceedings:

Yuan, T., Pleitez, M. A., Gasparin, F., & Ntziachristos, V. (2022, March). Wide-Field Mid-Infrared Hyperspectral Imaging by Snapshot Phase Contrast Measurement of Optothermal Excitation. *17th European Molecular Imaging Meeting, Thessaloniki*. (Poster)

Yuan, T., Gasparin, F., Uluc, N., Ntziachristos, V., & Pleitez, M. A. (2023, March). Functional live-cell mid-infrared microscopy and spectroscopy by optoacoustic and optothermal detection. In *Advanced Chemical Microscopy for Life Science and Translational Medicine 2023* (Vol. 12392, p. 1239202). SPIE.

Yuan, T., Gasparin, F., Ntziachristos, V., & Pleitez, M. A. (2023, June). Fast hyperspectral mid-infrared microscopy by phase-contrast optothermal detection. *European Conference on Biomedical Optics, Munich*. (Poster, SPIE)

Pleitez, M. A., **Yuan, T.**, Gasparin, F., Ntziachristos, V. (2022, March). Looking and listening at biomolecular vibrations: mid-infrared optoacoustic and optothermal sensing for bioanalysis and imaging. *17th European Molecular Imaging Meeting, Thessaloniki*. (Talk)

Yuan, T., Riobo, L., Gasparin, F., Ntziachristos, V, Pleitez, M. A., (2024, March) Wide field mid-infrared optothermal microscopy by phase-shifting background suppression. *First European meeting on InfraRed Nanospectro-Imaging 2024, Paris.* (Talk)

Bibliography

1. S. M. Burrows, R. D. Reif, D. Pappas, Investigation of photobleaching and saturation of single molecules by fluorophore recrossing events. *Anal. Chim. Acta* **598**, 135-142 (2007).
2. D. A. Helmerich, G. Beliu, S. S. Matikonda, M. J. Schnermann, M. Sauer, Photoblueing of organic dyes can cause artifacts in super-resolution microscopy. *Nat. Methods* **18**, 253-257 (2021).
3. N. Fili, C. P. Toseland, Fluorescence and labelling: how to choose and what to do. *Fluorescent Methods for Molecular Motors*, 1-24 (2014).
4. K. F. Freed, Radiationless transitions in molecules. *Accounts of Chemical Research* **11**, 74-80 (1978).
5. X. Wang, X. Xu, Thermoelastic wave induced by pulsed laser heating. *Applied Physics A* **73**, 107-114 (2001).
6. C. K. N. Patel, A. C. Tam, Pulsed optoacoustic spectroscopy of condensed matter. *Reviews of Modern Physics* **53**, 517 (1981).
7. J. B. Callis, The calorimetric detection of excited states. *Journal of Research of the National Bureau of Standards. Section A, Physics and Chemistry* **80**, 413 (1976).
8. J. B. Callis, M. Gouterman, J. D. S. Danielson, Flash calorimeter for measuring triplet yields. *Review of Scientific Instruments* **40**, 1599-1605 (1969).
9. M. Terazima, N. Hirota, Measurement of the quantum yield of triplet formation and short triplet lifetimes by the transient grating technique. *The Journal of chemical physics* **95**, 6490-6495 (1991).
10. L.-G. Rosengren, An opto-thermal gas concentration detector. *Infrared Physics* **13**, 173-182 (1973).
11. G. H. Brilmyer, A. Fujishima, K. S. V. Santhanam, A. J. Bard, Photothermal spectroscopy. *Analytical Chemistry* **49**, 2057-2062 (1977).
12. C. Hartung, R. Jurgeit, Optimization of the optothermal detector for absorption spectroscopy in the low pressure range. *Applied Physics B* **27**, 39-42 (1982).
13. A. C. Boccara, D. Fournier, W. Jackson, N. M. Amer, Sensitive photothermal deflection technique for measuring absorption in optically thin media. *Opt. Lett.* **5**, 377-379 (1980).
14. W. B. Jackson, N. M. Amer, A. C. Boccara, D. Fournier, Photothermal deflection spectroscopy and detection. *Applied optics* **20**, 1333-1344 (1981).
15. E. R. T. Kerstel, M. Becucci, G. Pietraperzia, E. Castellucci, Optothermal spectroscopy of the dissociating lowest electronic singlet states of s-tetrazine and dimethyl-s-tetrazine in a molecular beam. *The Journal of chemical physics* **106**, 1318-1325 (1997).

16. M. Becucci, N. M. Lakin, G. Pietraperzia, P. R. Salvi, E. Castellucci, E. R. T. Kerstel, High resolution optothermal spectroscopy of pyridine in the S 1 state. *The Journal of chemical physics* **107**, 10399-10405 (1997).
17. J. Gordon, R. Leite, R. S. Moore, S. Porto, J. Whinnery, Long-transient effects in lasers with inserted liquid samples. *Journal of Applied Physics* **36**, 3-8 (1965).
18. J. Shen, R. D. Lowe, R. D. Snook, A model for cw laser induced mode-mismatched dual-beam thermal lens spectrometry. *Chemical physics* **165**, 385-396 (1992).
19. J. Shen, M. L. Baesso, R. D. Snook, Three-dimensional model for cw laser-induced mode-mismatched dual-beam thermal lens spectrometry and time-resolved measurements of thin-film samples. *Journal of applied physics* **75**, 3738-3748 (1994).
20. J. Coates, Interpretation of infrared spectra, a practical approach. *Encyclopedia of analytical chemistry: applications, theory and instrumentation*, (2006).
21. Z. Movasaghi, S. Rehman, D. I. ur Rehman, Fourier Transform Infrared (FTIR) Spectroscopy of Biological Tissues. *Applied Spectroscopy Reviews* **43**, 134-179 (2008).
22. P. Lasch, M. Boese, A. Pacifico, M. Diem, FT-IR spectroscopic investigations of single cells on the subcellular level. *Vibrational spectroscopy* **28**, 147-157 (2002).
23. P. R. Griffiths, Fourier transform infrared spectrometry. *Science* **222**, 297-302 (1983).
24. R. A. Dluhy, R. Mendelsohn, Emerging techniques in biophysical FT-IR. *Analytical chemistry* **60**, 269A-278A (1988).
25. S. G. Kazarian, K. L. A. Chan, Applications of ATR-FTIR spectroscopic imaging to biomedical samples. *Biochimica et Biophysica Acta (BBA)-Biomembranes* **1758**, 858-867 (2006).
26. T. E. Gough, G. Scoles, "Optothermal infrared spectroscopy" in *Laser Spectroscopy V* (Springer, 1981), pp. 337-340.
27. E. R. T. Kerstel, K. K. Lehmann, B. H. Pate, G. Scoles, Reinvestigation of the acetylenic C–H stretching fundamental of propyne via high resolution, optothermal infrared spectroscopy: Nonresonant perturbations to ν1. *The Journal of chemical physics* **100**, 2588-2595 (1994).
28. M. E. Long, R. L. Swofford, A. C. Albrecht, Thermal lens technique: a new method of absorption spectroscopy. *Science* **191**, 183-185 (1976).
29. R. Gupta. (Academic Press: NY, 1989).
30. M. Harada, K. Iwamoto, T. Kitamori, T. Sawada, Photothermal microscopy with excitation and probe beams coaxial under the microscope and its application to microparticle analysis. *Analytical Chemistry* **65**, 2938-2940 (1993).
31. D. Boyer, P. Tamarat, A. Maali, B. Lounis, M. Orrit, Photothermal imaging of nanometer-sized metal particles among scatterers. *Science* **297**, 1160-1163 (2002).
32. A. Gaiduk, M. Yorulmaz, P. V. Ruijgrok, M. Orrit, Room-temperature detection of a single molecule's absorption by photothermal contrast. *Science* **330**, 353-356 (2010).

33. D. Zhang, C. Li, C. Zhang, M. N. Slipchenko, G. Eakins, J.-X. Cheng, Depth-resolved mid-infrared photothermal imaging of living cells and organisms with submicrometer spatial resolution. *Sci. Adv.* **2**, e1600521 (2016).
34. K. Hamada, K. Fujita, N. I. Smith, M. Kobayashi, Y. Inouye, S. Kawata, Raman microscopy for dynamic molecular imaging of living cells. *Journal of biomedical optics* **13**, 044027 (2008).
35. M. D. Duncan, J. Reintjes, T. J. Manuccia, Scanning coherent anti-Stokes Raman microscope. *Opt. Lett.* **7**, 350-352 (1982).
36. A. Zumbusch, G. R. Holtom, X. S. Xie, Three-dimensional vibrational imaging by coherent anti-Stokes Raman scattering. *Phys. Rev. Lett.* **82**, 4142 (1999).
37. C. W. Freudiger, W. Min, B. G. Saar, S. Lu, G. R. Holtom, C. He, J. C. Tsai, J. X. Kang, X. S. Xie, Label-free biomedical imaging with high sensitivity by stimulated Raman scattering microscopy. *Science* **322**, 1857-1861 (2008).
38. K. Kneipp, A. S. Haka, H. Kneipp, K. Badizadegan, N. Yoshizawa, C. Boone, K. E. Shafer-Peltier, J. T. Motz, R. R. Dasari, M. S. Feld, Surface-enhanced Raman spectroscopy in single living cells using gold nanoparticles. *Applied spectroscopy* **56**, 150-154 (2002).
39. S. E. J. Bell, N. M. S. Sirimuthu, Surface-enhanced Raman spectroscopy (SERS) for sub-micromolar detection of DNA/RNA mononucleotides. *Journal of the American Chemical Society* **128**, 15580-15581 (2006).
40. Y. Fu, H. Wang, R. Shi, J.-X. Cheng, Characterization of photodamage in coherent anti-Stokes Raman scattering microscopy. *Opt. Express* **14**, 3942-3951 (2006).
41. C. A. Casacio, L. S. Madsen, A. Terrasson, M. Waleed, K. Barnscheidt, B. Hage, M. A. Taylor, W. P. Bowen, Quantum-enhanced nonlinear microscopy. *Nature* **594**, 201-206 (2021).
42. W. S. Barney, L. M. Wingen, M. J. Lakin, T. Brauers, J. Stutz, B. J. Finlayson-Pitts, Infrared absorption cross-section measurements for nitrous acid (HONO) at room temperature. *The Journal of Physical Chemistry A* **104**, 1692-1699 (2000).
43. D. Lasne, G. A. Blab, F. De Giorgi, F. Ichas, B. Lounis, L. Cognet, Label-free optical imaging of mitochondria in live cells. *Opt. Express* **15**, 14184-14193 (2007).
44. E. S. Lee, J. Y. Lee, Nonlinear optical infrared microscopy with chemical specificity. *Appl. Phys. Lett.* **94**, 261101 (2009).
45. E. S. Lee, J. Y. Lee, High resolution cellular imaging with nonlinear optical infrared microscopy. *Opt. Express* **19**, 1378-1384 (2011).
46. A. Mërtiri, A. Totachawattana, H. Liu, M. K. Hong, T. Gardner, M. Y. Sander, S. Erramilli. (Optical Society of America), pp. AF1B-4.
47. Y. Bai, D. Zhang, C. Li, C. Liu, J.-X. Cheng, Bond-selective imaging of cells by mid-infrared photothermal microscopy in high wavenumber region. *The Journal of Physical Chemistry B* **121**, 10249-10255 (2017).

48. M. A. Welte, Bidirectional transport along microtubules. *Curr. Biol.* **14**, R525-R537 (2004).
49. G. T. Shubeita, S. L. Tran, J. Xu, M. Vershinin, S. Cermelli, S. L. Cotton, M. A. Welte, S. P. Gross, Consequences of motor copy number on the intracellular transport of kinesin-1-driven lipid droplets. *Cell* **135**, 1098-1107 (2008).
50. K. Toda, M. Tamamitsu, Y. Nagashima, R. Horisaki, T. Ideguchi, Molecular contrast on phase-contrast microscope. *Sci. Rep.* **9**, 9957 (2019).
51. M. Tamamitsu, K. Toda, H. Shimada, T. Honda, M. Takarada, K. Okabe, Y. Nagashima, R. Horisaki, T. Ideguchi, Label-free biochemical quantitative phase imaging with mid-infrared photothermal effect. *Optica* **7**, 359-366 (2020).
52. D. Zhang, L. Lan, Y. Bai, H. Majeed, M. E. Kandel, G. Popescu, J.-X. Cheng, Bond-selective transient phase imaging via sensing of the infrared photothermal effect. *Light Sci. Appl.* **8**, 116 (2019).
53. K. Toda, M. Tamamitsu, T. Ideguchi, Adaptive dynamic range shift (ADRIFT) quantitative phase imaging. *Light Sci. Appl.* **10**, 1-10 (2021).
54. C. Wang, Q. Fu, X. Dun, W. Heidrich, Quantitative phase and intensity microscopy using snapshot white light wavefront sensing. *Scientific reports* **9**, 1-12 (2019).
55. Y. Park, C. Depeursinge, G. Popescu, Quantitative phase imaging in biomedicine. *Nat. Photonics* **12**, 578-589 (2018).
56. D. Griffith, Introduction to Quantum Mechanics 2014. *Essex: Pearson*.
57. E. B. Wilson, J. C. Decius, P. C. Cross, *Molecular vibrations: the theory of infrared and Raman vibrational spectra* (Courier Corporation, 1980).
58. J. Tennyson, N. F. Zobov, R. Williamson, O. L. Polyansky, P. F. Bernath, Experimental energy levels of the water molecule. *Journal of Physical and Chemical Reference Data* **30**, 735-831 (2001).
59. M. Stomp, J. Huisman, L. J. Stal, H. C. P. Matthijs, Colorful niches of phototrophic microorganisms shaped by vibrations of the water molecule. *The ISME journal* **1**, 271-282 (2007).
60. S. Türker-Kaya, C. W. Huck, A review of mid-infrared and near-infrared imaging: principles, concepts and applications in plant tissue analysis. *Molecules* **22**, 168 (2017).
61. B. C. Smith, *Infrared spectral interpretation: a systematic approach* (CRC press, 2018).
62. M. A. Pleitez, A. A. Khan, A. Soldà, A. Chmyrov, J. Reber, F. Gasparin, M. R. Seeger, B. Schätz, S. Herzig, M. Scheideler, Label-free metabolic imaging by mid-infrared optoacoustic microscopy in living cells. *Nat. Biotechnol.*, 1-4 (2019).
63. M. J. Baker, J. Trevisan, P. Bassan, R. Bhargava, H. J. Butler, K. M. Dorling, P. R. Fielden, S. W. Fogarty, N. J. Fullwood, K. A. Heys, Using Fourier transform IR spectroscopy to analyze biological materials. *Nature protocols* **9**, 1771 (2014).

64. A. Jabs, Determination of secondary structure in proteins by fourier transform infrared spectroscopy (FTIR). *Jena Library of Biologica Macromolecules*, (2005).
65. M. N. Ã–zisik, M. N. Özışık, M. N. Özısık, *Heat conduction* (John Wiley & Sons, 1993).
66. N. Morad, M. Idrees, A. Hasan, Specific heat capacities of pure triglycerides by heat-flux differential scanning calorimetry. *Journal of thermal analysis* **45**, 1449-1461 (1995).
67. T. Gouw, J. Vlugter, Physical properties of triglycerides. I. Density and refractive index. *Fette, Seifen, Anstrichmittel* **68**, 544-549 (1966).
68. N. S. Bogatishcheva, M. Z. Faizullin, A. P. Popov, E. D. Nikitin, Critical properties, heat capacities, and thermal diffusivities of four saturated triglycerides. *The Journal of Chemical Thermodynamics* **113**, 308-314 (2017).
69. F. Zernike, Phase contrast, a new method for the microscopic observation of transparent objects. *Physica* **9**, 686-698 (1942).
70. F. Zernike, How I discovered phase contrast. *Science* **121**, 345 (1955).
71. E. Bergstrand, A. Maréchal, M. Françon, H. Wolter, H. Wolter, Schlieren-, Phasenkontrast- und Lichtschnittverfahren. *Grundlagen der Optik/Fundamentals of Optics*, 555-645 (1956).
72. H. Kadono, M. Ogusu, S. Toyooka, Phase shifting common path interferometer using a liquid-crystal phase modulator. *Optics communications* **110**, 391-400 (1994).
73. M. Totzeck, N. Kerwien, A. V. Tavrov, E. Rosenthal, H. J. Tiziani. (SPIE), vol. 4777, pp. 1-11.
74. K. F. Webb, G. de Fillipi, N. Johnston, Condenser-free zernike phase contrast imaging for scanning probe microscopy. *Microsc. Anal* **27**, 27-32 (2013).
75. K. F. Webb, Condenser‐free contrast methods for transmitted‐light microscopy. *J. Microsc.* **257**, 8-22 (2015).
76. J. E. Krist, in *Optical Modeling and Performance Predictions III. URL: http://proper-library.sourceforge.net/*. (International Society for Optics and Photonics, 2007), vol. 6675, pp. 66750P.
77. T. Yuan, M. A. Pleitez, F. Gasparin, V. Ntziachristos, Wide-field mid-infrared hyperspectral imaging by snapshot phase contrast measurement of optothermal excitation. *Anal. Chem.* **93**, 15323-15330 (2021).
78. A. H. Bennett, H. Jupnik, H. Osterberg, W. Oscar, *Phase microscopy: principles and applications* (Wiley, 1951).
79. D. G. Stavenga, H. L. Leertouwer, B. D. J. L. S. Wilts, Applications, Quantifying the refractive index dispersion of a pigmented biological tissue using Jamin–Lebedeff interference microscopy. *Light: Science & Applications* **2**, e100-e100 (2013).
80. B. J. Thompson, D. Goldstein, D. H. Goldstein, Polarized Light. (2003).

81. A. Ahmad, V. Dubey, A. Butola, J.-C. Tinguely, B. S. Ahluwalia, D. S. Mehta, Sub-nanometer height sensitivity by phase shifting interference microscopy under environmental fluctuations. *Opt. Express* **28**, 9340-9358 (2020).
82. L. M. Riobó, F. E. Veiras, P. A. Sorichetti, M. T. Garea, Wideband quad optical sensor for high-speed sub-nanometer interferometry. *Appl. Opt.* **56**, 397-403 (2017).
83. M. Zhao, L. Huang, Q. Zhang, X. Su, A. Asundi, Q. Kemao, Quality-guided phase unwrapping technique: comparison of quality maps and guiding strategies. *Appl. Opt.* **50**, 6214-6224 (2011).
84. M. Zhao, H. Wang, Q. Kemao, Snake-assisted quality-guided phase unwrapping for discontinuous phase fields. *Appl. Opt.* **54**, 7462-7470 (2015).
85. S. Murugkar, C. Brideau, A. Ridsdale, M. Naji, P. K. Stys, H. Anis, Coherent anti-Stokes Raman scattering microscopy using photonic crystal fiber with two closely lying zero dispersion wavelengths. *Opt. Express* **15**, 14028-14037 (2007).
86. T. Yuan, L. Riobo, F. Gasparin, V. Ntziachristos, M. A. Pleitez, Phase-shifting optothermal microscopy enables live-cell mid-infrared hyperspectral imaging of large cell populations at high confluency. *Sci. Adv.* **10**, eadj7944 (2024).
87. S. Bégin, B. Burgoyne, V. Mercier, A. Villeneuve, R. Vallée, D. Côté, Coherent anti-Stokes Raman scattering hyperspectral tissue imaging with a wavelength-swept system. *Biomed. Opt. Express* **2**, 1296-1306 (2011).
88. G. Topman, O. Sharabani-Yosef, A. Gefen, A method for quick, low-cost automated confluency measurements. *Microsc. Microanal.* **17**, 915-922 (2011).
89. J. Zhao, A. Matlock, H. Zhu, Z. Song, J. Zhu, B. Wang, F. Chen, Y. Zhan, Z. Chen, Y. Xu, X. Lin, L. Tian, J.-X. Cheng, Bond-selective intensity diffraction tomography. *Nat. Commun.* **13**, 7767 (2022).
90. H. Salehi, L. Derely, A.-G. Vegh, J.-C. Durand, C. Gergely, C. Larroque, M.-A. Fauroux, F. J. Cuisinier, Label-free detection of anticancer drug paclitaxel in living cells by confocal Raman microscopy. *Appl. Phys. Lett.* **102**, 113701 (2013).
91. P. Khakbaz, J. B. Klauda, Investigation of phase transitions of saturated phosphocholine lipid bilayers via molecular dynamics simulations. *Biochimica et Biophysica Acta (BBA)-Biomembranes* **1860**, 1489-1501 (2018).
92. T. Ikeda, G. Popescu, R. R. Dasari, M. S. Feld, Hilbert phase microscopy for investigating fast dynamics in transparent systems. *Opt. Lett.* **30**, 1165-1167 (2005).
93. B. Bhaduri, G. Popescu, Derivative method for phase retrieval in off-axis quantitative phase imaging. *Opt. Lett.* **37**, 1868-1870 (2012).
94. X. Xie, Iterated unscented Kalman filter for phase unwrapping of interferometric fringes. *Opt. Express* **24**, 18872-18897 (2016).

95. C. Jüngst, M. Klein, A. Zumbusch, Long-term live cell microscopy studies of lipid droplet fusion dynamics in adipocytes [S]. *Journal of lipid research* **54**, 3419-3429 (2013).
96. M. Paar, C. Jüngst, N. A. Steiner, C. Magnes, F. Sinner, D. Kolb, A. Lass, R. Zimmermann, A. Zumbusch, S. D. Kohlwein, Remodeling of lipid droplets during lipolysis and growth in adipocytes. *Journal of Biological Chemistry* **287**, 11164-11173 (2012).
97. J. Gong, Z. Sun, L. Wu, W. Xu, N. Schieber, D. Xu, G. Shui, H. Yang, R. G. Parton, P. Li, Fsp27 promotes lipid droplet growth by lipid exchange and transfer at lipid droplet contact sites. *Journal of Cell Biology* **195**, 953-963 (2011).